Identification of tool-toolholder-spindle dynamics for high speed milling

Geurtsen, E.A.J.

Award date:
2007

Identification of Tool-Toolholder-Spindle Dynamics for High Speed Milling

ing. E.A.J. Geurtsen

Reportnr. DCT 2007.046

Coach: Ir. R. Faassen
Coach: Dr.Ir. N. van de Wouw
Supervisor: Prof.Dr. H. Nijmeijer

Eindhoven University of Technology
Department of Mechanical Engineering
Dynamics and Control Group

Eindhoven, April 18, 2007

Keywords: High Speed Milling, Chatter, (Inverse)Receptance Coupling, Modelling, Experiments.

Contents

Abstract

High speed milling (HSM) has been known and used in industry for many years. Throughout these years, in the HSM process, a problem known as chatter is encountered. Chatter is often the most important factor limiting the spindle speed and depth of cut which together determine the material removal rate (MRR) (i.e. the milling efficiency). Namely, chatter causes large vibrations of the tool resulting in a damaged workpiece noise and tool wear. In order to prevent chatter and optimize the MRR while maintaining the product quality, TNO Science and Industry and the TU/e have jointly started the Chattercontrol project in co-operation with Jabro Tools, VDL ETG and Somatech. In this project, an "in process chatter controller" is developed to ensure chatter-free milling.

In order to predict chatter in the milling process as accurately as possible, the dynamics of the tool-toolholder-spindle-system of the HSM machine need to be known since they are an important part of a model for the HSM process. These dynamic properties are different for every single tool-toolholder-spindle-system combination on the HSM machine. Therefore, new measurements have to be performed for every new tool-toolholder-spindle-system combination to identify the corresponding dynamics.

Commonly, the dynamics of each combination are determined experimentally by performing impulse hammer experiments. Performing new experiments every time the combination changes is a time-consuming process, which causes loss of operating time on the HSM machine.

In this work, we aim at increasing the efficiency of this identification process without costly adaptations to the milling machine. This is done by dividing the dynamics of the tool-toolholder-spindle-system into: on the one hand the tool dynamics and, on the other hand, the toolholder-spindle dynamics. The dynamics of both subsystems are stored in a data-base incorporating the dynamics for different toolholders (in combination with specific spindle) and different tools. By making use of the receptance coupling (RC) technique to couple the dynamics of the two separate subsystems from the data-base, joint models for every tool-toolholder-spindle combination are available. Finite element methods (FEM) are used to determine the dynamics of the freely supported tool. Measurements in combination with inverse receptance coupling (IRC) are used to identify the dynamics of the toolholder-spindle combination. Using the assembled dynamics in a model for the high-speed milling process, the so called stability lobe diagram (SLD) can be constructed, which characterizes combinations of the spindle speed and depth of cut avoiding chatter. Using such SLDs, a suitable (chatter free) working point for the milling process can be calculated.

The RC and IRC procedure developed in this thesis is tested with models and validated experimentally. The models of the RC and IRC method shows that the identification procedure is exact. The validation is carried out on a Mikron HSM 700 machine available at TNO Science and Industry. This milling machine is equipped with a shrink-fit tool holder and an end-mill replacement.

The validation shows that, using the proposed identification strategy, the dynamics of the tool-toolholder-spindle combination can be predicted accurately. Therefore, it is an efficient method to identify the dynamics for a large number of machine-toolholder-tool combinations.

Samenvatting

Hoge snelheid frezen (HSF) is al vele jaren bekend en wordt al vele jaren toegepast in de industrie. Al sinds het begin kampt HSF met het zogenaamde chatter probleem. Chatter is meestal de limiterende factor in spindel-snelheid en snede-diepte die samen de verspaning-snelheid vaststellen (een maat voor de efficiëntie van het freesproces). Chatter veroorzaakt grote vibraties van de frees wat resulteert in een inferieure kwaliteit van het werkstuk, een onaangenaam geluid en slijtage van de frees. Voor het beheersen van het chatter verschijnsel en het optimaliseren van de verspaning-snelheid met behoud van de product kwaliteit hebben TNO Industrie en Techniek en de TU/e het Chattercontrol project opgestart in samenwerking met Jabro Tools, VDL ETG en Somatech. In dit project, wordt een "in process chatter controller" ontwikkeld welke chattervrij frezen verzekert.

Om chatter tijdens het freesproces zo nauwkeurig mogelijk te voorspellen, moet de dynamica van het spindel-freeshouder-frees-systeem van de HSF machine bekend zijn, aangezien dit een belangrijk onderdeel voor het model van de HSF machine is. De dynamische eigenschappen zijn voor elke combinatie van spindel-freeshouder-frees anders. Bij een andere spindel-freeshouder-frees-systeem combinatie moet daarom de daarbij behorende dynamica opnieuw gemeten worden.

Deze dynamica wordt tegenwoordig bepaald door het experimenteel meten van de betreffende spindel-freeshouder-frees-combinatie door middel van impuls hamer testen. Het uitvoeren van deze hamer test, voor elke keer dat de spindel-freeshouder-frees-combinatie verandert, is erg tijd rovend waardoor de machine onnodig vaak stil staat.

In dit verslag richten wij ons op het efficiënter maken van het identificatie proces, zonder kostbare aanpassingen uit te voeren op de machine. Dit wordt gedaan door de dynamica op te splitsen in enerzijds de dynamica van de frees en anderzijds de dynamica van het spindel-freeshouder systeem. De dynamica van beide subsystemen wordt in een data-base opgeslagen. Deze omvat de dynamica van de verschillende freeshouders (in combinatie met de specifieke spindel) en de verschillende frezen. Door gebruik te maken van de receptantie koppeling (RK) methode voor het aan elkaar koppelen van de subsystemen uit de data-base, kunnen samengevoegde modellen van de gewenste spindel-freeshouder-frees-systeem combinaties berekend worden. Eindige elementen modellen (EEM) worden gebruikt voor het berekenen van de vrij opgespannen frees. Metingen in combinatie met inverse reseptantie koppeling IRK berekeningen worden gebruikt voor het identificeren van de dynamica van de spindel-freeshouder-frees combinaties. Met deze dynamica worden zo genaamde stabiliteitslobben (SLD) geconstrueerd, deze karakteriseren de combinatie van spindel-snelheid en snede-diepte met het voorkomen van chatter. Door gebruik te maken van deze SLDs kan een geschikt (chatter vrij) werkpunt voor het freesproces berekend worden.

De IRK en RK procedure, ontwikkeld in deze scriptie, is getest middels simulatie modellen en is experimenteel gevalideerd door middel van hamer experimenten. Uit de gemaakte modellen van de RK en IRK methoden kan geconcludeerd worden dat de voorgestelde identificatie procedure exact is. De validatie is uitgevoerd op een Mikron HSM 700 machine van TNO Industrie en Techniek. Deze freesmachine is uitgevoerd met een krimphouder en als gereedschap een cilinder met twee vlakke kanten aan de punt.

De validatie laat zien dat bij het toepassen van de voorgestelde identificatie procedure,

de dynamica van de gewenste spindel-freeshouder-frees combinatie nauwkeurig voorspeld kan worden. Hierdoor is het een efficiënte methode om de dynamica te identificeren van een groot aantal combinaties van machine, gereedschapshouder en gereedschap.

Acknowledgements

During my graduation work, I have studied coupling techniques. These techniques were developed 50 years ago and nowadays, these techniques are still in development. This made it an interesting and innovative subject to work on. Also, the high speed milling process and the chatter phenomena are studied, models of the receptance coupling and inverse receptance coupling technique are build and system identifications are performed on a milling machine to verify the developed models. During my work, I have met a lot of people who made it possible for me to realize this project, and I would like to thank a few of them:

My parents, Albert and Wil Geurtsen, for their great support throughout my graduation. My girlfriend C. van Santen for all her support especially in hard times. R. Faassen for the fine team work, great coaching, close support, fun and help on the problems that I faced. N. van de Wouw for the coaching, support and help on solving problems during my graduation. H. Nijmeijer for the coaching and support on the project. R. Fey for the support, knowledge on the different coupling techniques and FEM programs. R. Kodde for his knowledge on sensors. H. Hijink for sharing his knowledge and experience on the measurements on an HSM and his expertise on JPEG files. J. Chae for his time and help on the derivation of the coupling equation, solving problems for making the coupling equation work. S. Kersjes for his knowledge on residual flexibility by making the Ansys models. M. Aarts for his time and knowledge for the development of the calculation procedure of the tool. E. Homburg for the help with the Ansys FEM program. W. Dijkhof for the time and guidance on the calculation of FRFs from FE models with the aid of Matlab. R. van den Hooff for his help and support with Ansys FEM program. Especially for the making of the Solid 72 element for this application. F. Podbevsek for his knowledge and experience on the field of IGES files. O. van Buul for his help with the conversion of the model of the mill. F. Soers for his help with importing the end-mill in STEP format. M. Anthonissen for his help and mathematical knowledge on the IRC equations. W. Verbrugge from UniGraphics for the help on repairing the STEP file type and conversion to Ansys. N. Mallon for his help on compiling the rdfull.exe.

Chapter 1

Introduction

1.1 The high-speed milling process

Even though high-speed machining has been known for a long time, the first attempts for milling at high speeds were not made until the early thirties of the past century. In 1931, Carl Salomon [54] made his first attempt of high-speed milling (HSM). He assumed that at a certain cutting speed which is 5-10 times higher than in conventional machining, the chip tool interface temperature would start to decrease while the milling process remains stable. This was the first discovery of milling with high speeds while maintaining a high product quality.

Nowadays high-speed milling is widely used in the manufacturing industry, mostly for manufacturing of aluminium components. Also other materials such as synthetic materials are processed with HSM, for example in the casting industry for the production of moulds. In the aerospace industry, HSM has changed the way aircrafts are manufactured. HSM enables the replacement of sheet-metal assemblies with machined monolithic components resulting in cost savings and improved performance. These monolithic structures can be stronger, lighter, and more precise than the sheet-metal build-ups. Machining with high speeds, up to 50000 rev/min with a high load capacity, is nowadays one of the modern manufacturing technologies that, in comparison with conventional cutting, enables to increase efficiency, accuracy and quality of the resulting workpieces and, at the same time, enables to decrease costs and machining time [66].

The ever increasing demand for products of high quality and lower manufacturing costs requires a closer look at manufacturing operations. For the efficiency of the milling process, high demands on the material removal rate (MRR) and the surface generation rate (SGR) are posed. If we look at the fabrication of moulds and the aeroplane building industry, where large amounts of material are removed from a large structure, up to 90% removal of the initial amount of material. The milling process is most efficient if the MRR is as large as possible, while maintaining a high quality level of the machined surface. This is the so-called maximum material removal rate (MMRR).

Part errors may be due to forced vibrations or due to an instability in the cutting process known as chatter. There is a well-established literature on chatter (unstable cutting) and its linkage to the dynamics of the milling machine and its tooling as described by Altintas et al. [2]. The tool-spindle dynamics of the HSM machine are highly important for the stability of the cutting process (i.e. the occurrence of chatter). Both the maximum spindle speed and maximum depth of cut are limited by these tool-spindle dynamics.

Research on the milling process and the stability of the cutting process has been done for several decades. Schmitz has investigated the prediction of chatter [20, 40, 64], the role of tool length on the stability in milling [63], the role of cutter eccentricity [62] and improving the MRR [60]. Stépán et al. [70, 71, 73, 74] has performed research on HSM models, with a focus on the nonlinearities occurring primarily in low-immersion high-speed milling. Altintas

et al. describe the role of the tool-spindle dynamics in the analytical prediction of stability lobes in milling [2, 3, 41, 43]. Herein, it is shown that these dynamics represent a very important factor in the occurrence of chatter. More specifically, the tool-toolholder-spindle dynamics forms an intricate part of state-of-the-art milling models used to predict so-called stability lobe diagrams (SLD). SLDs depict the chatter boundary in the process parameter space (i.e. spindle speed and depth of cut) and play an important role in guiding the machinist in choosing a chatter-free working point.

Identification of the tool-spindle dynamics is therefore of great importance. Many different methods to identify the tool-spindle dynamics have been proposed throughout the years. Commonly, the dynamics of a specific tool-toolholder-spindle combination as a whole is determined with conventional hammer experiments [25]. This is a time-consuming process, which has to be repeated for every tool-toolholder-spindle combination. This causes causes loss of operating time on the HSM machine. Also, different methods to calculate the tool-spindle dynamics have been proposed. On the one hand, coupling techniques to couple the spindle dynamics with the dynamics of different tool-toolholder-systems in combination with coupling parameters (for the cross-section stiffness and damping) are used to estimate the dynamics of the tool-toolholder-spindle combination [1, 44, 45]. In this way, the dynamics of the HSM machine are calculated off-line without the loss of operating time. Nevertheless, the coupling parameters must be fit accurately to obtain realistic results. This parameter fitting process is time consuming and therefore undesirable. On the other hand, coupling techniques and the placement of force sensors in the spindle of the HSM machine are used in combination in [47]. With these methods the dynamics of the HSM machine-tool combinations are also estimated off-line. However, equipping the HSM machine with force sensors integrated in the spindle is a costly and difficult adaptation on the milling machine. Therefore, our goal is to develop a method that is efficient and relatively simple to apply without making adaptations to the milling machine. In this thesis, such a method is presented that can be used to efficiently identify the dynamics of a spindle and a set of tools.

1.2 Chatter

The onset of chatter during machining is primarily caused by the variation in chip thickness that occurs due to vibration of the tool, workpiece, or both. This situation is shown schematically in Figure 1.1. In this figure, the flexible tool engages the workpiece and, due to the time-varying cutting force, begins to vibrate. This vibration is imprinted on the machined surface. In milling, the next tooth on the rotating cutter encounters this wavy surface produced by the previous tooth. This wavy surface varies the instantaneous chip thickness which,

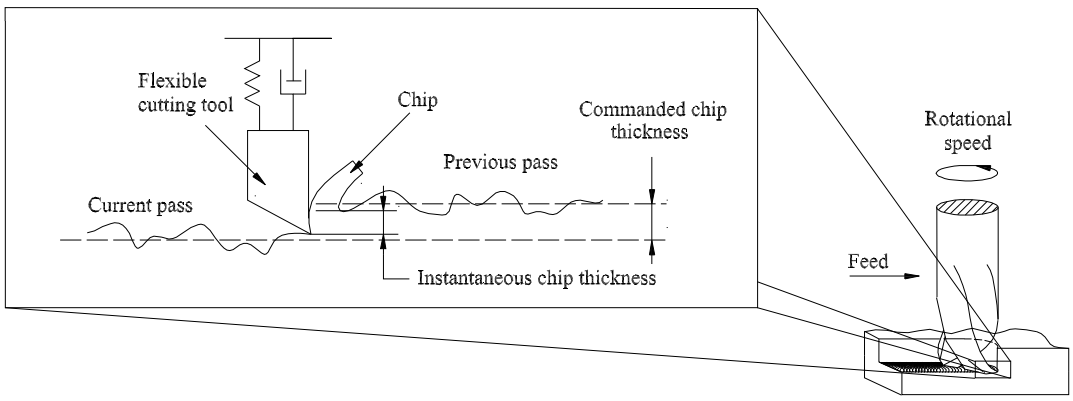

Figure 1.1: Chip thickness variation due to cutter vibrations.

in turn, modulates the cutting force and the cutter vibration (i.e., a feedback mechanism is produced that can lead to self-excited vibrations known as regenerative chatter). Depending on the relationship between the wavy surface left by the previous tooth and the current cutter vibration, the resulting deflections and forces can grow very large, which results in rapid tool wear, an inferior surface quality of the workpiece and noise [2, 19, 25, 76]. Chatter can be recognized by the noise provided by these vibrations, the chatter marks on the machined surface, see Figure 1.2, and the appearance of the chips. Correspondingly, the depth of cut

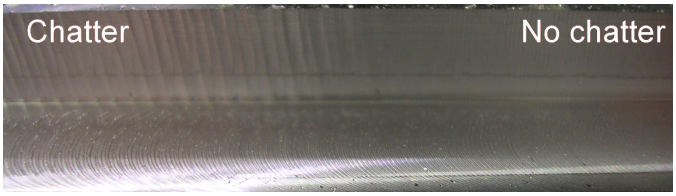

Figure 1.2: Chatter marks on the machined surface.

and the spindle speed (i.e. the MRR) must be kept below the limit at which chatter occurs. In this respect, chatter is often the most important factor limiting the MMRR. Consequently, the model-based prediction of regenerative chatter is of great interest. In the current work, we contribute to the prediction of chatter by focusing on the part of the milling model involving the identification of the dynamics of the tool-toolholder-spindle combination.

1.3 The Chattercontrol project

The MRR of the high-speed milling process is restricted by the chatter phenomenon. In order to maximize the MRR while avoiding chatter, TNO Science and Industry and the TU/e have jointly started the Chattercontrol project in co-operation with Jabro Tools, VDL ETG and Somatech. The Chattercontrol project started in June 2003 with a duration of four years. The goal of this project is to develop an "in process chatter control".

To pursue this goal an advanced controller is developed that can detect the onset of chatter and interfere in the process, such that chatter does not occur. The main goals of the Chattercontrol project are: (1) development of a new model of the milling process; (2) development of a method to predict chatter reliably and efficiently; (3) online detection of the onset of chatter and the interference in the milling process with the "in process chatter controller" to maintain stable cutting by preventing chatter; (4) development of a hardware device that can be coupled to an NC milling machine to prevent and control chatter.

This work is part of the Chattercontrol project and this thesis focusses on the reliable and efficient prediction of chatter by identifying the tool-spindle dynamics for a variety of tool-toolholder-spindle combinations. The identified tool-toolholder-spindle dynamics can be used off-line in milling models to provide a working-point for the milling process (in terms of depth of cut and spindle speed) guaranteeing both a large MRR and stable cutting conditions. This stable working-point is kept stable on-line by the developed controller to perform highly efficient milling with robustness against changing conditions (tool wear, temperature etc.).

1.4 Problem statement

In order to predict chatter in the milling process as accurately as possible, the dynamics of the tool-toolholder-spindle-system needs to be known for a collection of tool-toolholder-spindle combinations. Therefore, the dynamic properties of the different spindle, toolholder, tool combinations on the HSM machine under evaluation need to be categorized in the form

of a data-base. The data-base can be filled by performing analytic calculations, finite element (FE) calculations or by performing measurements in the form of hammer experiments (impulse response measurements), shaker experiments or non-contact measurements [21, 35]. Commonly, the dynamics of a specific tool-toolholder-spindle combination as a whole is determined experimentally. This is a time-consuming process, which has to be repeated for every tool-toolholder-spindle combination, which causes loss of operating time on the HSM machine.

In this work, we aim at increasing the efficiency of this identification process. We aim to do so by separately modelling, firstly, the tool dynamics and, secondly, the toolholder-spindle dynamics. By coupling these models, joint models for every tool-toolholder-spindle combination can than become available. A study needs to be done to determine which of the existing coupling techniques is most suited for the coupling of the models of the tool and toolholder-spindle. By integrating the dynamics of the tool-toolholder-spindle-system from the data-base in the overall milling process model, a 'chatter-free' working-point for the "in process chatter controller" can be calculated. This calculation takes place off-line such that interference with ongoing work on the milling-machine on the work-floor is avoided. In this thesis, the chosen coupling technique will be tested in practice on a specific tool-toolholder-spindle-system combination. The result will be validated with conventional hammer experiments on that specific tool-toolholder-spindle-system combination.

With this method, the dynamics of the spindle of the HSM machine can be identified for a range of combinations of tools and toolholders to provide a working-point for the "in process chatter controller" to start and maintain chatter-free milling.

1.5 Outline of the report

The history of chatter in HSM, the modelling of the HSM process and the importance of the dynamics of the machine, tool and toolholder combination herein is explained in Chapter 2. Substructuring techniques are discussed in Chapter 3 since these techniques will be used to couple the dynamics of the tool and toolholder-spindle combination. From a range of coupling methods, the one that is most suited for this application is chosen where characteristics as efficiency, reliability, accuracy and level of implementation difficulty are considered. In Section 3.2, this specific method (receptance coupling (RC) method) is explained and, in Section 3.3, an example of the chosen coupling method is presented to provide insight in the method. Not only the coupling of substructures to form a total joint structure is possible; it is also possible to use the substructuring techniques to calculate the dynamics of one of the substructures instead of the dynamics of the total joint structure. The applications and background of this decoupling of structures is treated in Section 3.4. An example of this decoupling is presented in Section 3.5. In Section 3.6, the influence of measurement errors is examined on this example since the reliability of the method in the face of measurement errors is highly important in practice. A literature investigation of coupling the spindle-toolholder-toolsystems is treated in Chapter 4 where we apply the substructuring techniques to the spindle-toolholder-toolsystems in Section 4.1. In Section 4.2, the importance of rotational degrees of freedom (RDOFs) in coupling the spindle-toolholder-toolsystems and the introduction of RDOFs in the coupling process on the HSM machine is discussed. The identification of the dynamics of the tool and toolholder-spindle combination is treated in Section 4.3 and 4.4, respectively. In Section 4.5, the developed RC and IRC procedure is discussed. The implementation of the coupling technique on the HSM machine is presented in Chapter 5. Herein, the IRC and RC technique is validated in Section 5.1 and 5.2, respectively. Finally conclusions and recommendations are presented in Chapter 6.

Chapter 2

Models of the HSM process

The pioneering models for the prediction of chatter were introduced by Tlusty and Polacek [77], and Tobias and Fiswick [78]. They independently formulated the chatter stability law. This law describes the chatter boundaries as a function of process parameters, such as spindle speed and depth-of-cut. This method has been widely used since the 1950's. Tobias and Fiswick studied chatter in a one-degree-of-freedom model. They utilized the properties of the chatter stability law and introduced spindle speed dependent chatter stability lobes. In order to consider the process damping in chatter stability, the International Academy for Production Engineering (CIRP - from the French name College International pour la Recherche en Productique, 1951), formed a task force identifying the dynamic cutting coefficients using a common test set-up proposed by Peters, Vanherck and Brussel [49]. Tlusty summarized the research findings in great detail in [75]. The dynamic cutting coefficients were calibrated experimentally by correlating the tool geometry, chatter vibration frequency and cutting speed. However, the experimental set-ups were limited to low vibration frequencies and cutting speeds. Montgomery and Altintas attempted to model the penetration of a hard tool into the softer work material with wavy surface finish using laws of contact mechanics [43]. However, the model is not accurate at high frequencies.

The chatter stability law presented by Tlustly et al. and stability lobes introduced by Tobias et al. has had a fundamental impact in designing machine tools and selection of productive cutting conditions, and has led to expanded stability formulations and interpretations [46, 50].

Therefore, these theories form a basis of the milling model developed for the chattercontrol project. This milling model is created by Faassen et al. [25–27]. In the model, the chip thickness, encountered by the tool in cut, is related to the rotation angle of the end-mill, cutting force, machine dynamics and delay caused by the tooth passing period. A block diagram of the milling process is depicted in Figure 2.1, as presented in [25]. In this diagram,

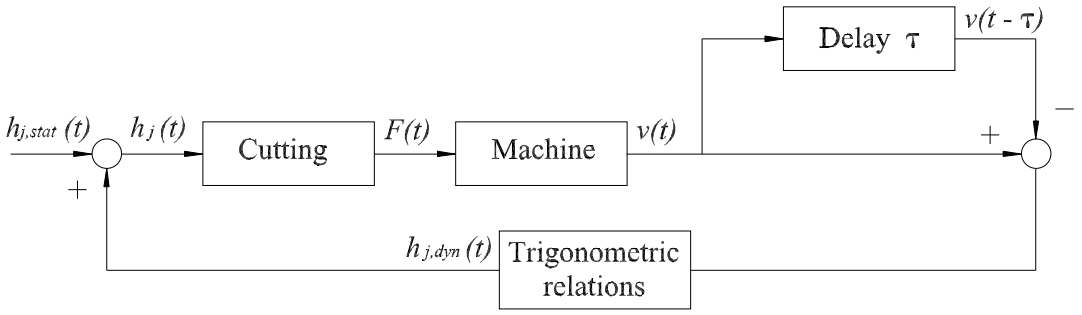

Figure 2.1: Block diagram of the model of the milling process.

the total chip thickness of tooth j, $h_j(t)$, is the sum of the static and dynamic chip thickness,

$$h_j(t) = h_{j,stat}(t) + h_{j,dyn}(t). \tag{2.1}$$

The static chip thickness $h_{j,stat}(t)$ is a result of the predefined motion of the tool with respect to the workpiece and is described by

$$h_{j,stat}(t) = f_z \sin \phi_j(t), \tag{2.2}$$

with $\phi_j(t)$ the rotation angle of tooth j and f_z the chip load. The chip thickness results, via the cutting process (block Cutting in Figure 2.1), in a force F that acts on the tool. The forces in tangential and radial direction are described by

$$\begin{aligned} F_{t_j}(t) &= \big(K_t\, a_p\, h_j(t)^{x_F} + K_{te}\, a_p\big) g_j\big(\phi_j(t)\big), \\ F_{r_j}(t) &= \big(K_r\, a_p\, h_j(t)^{x_F} + K_{re}\, a_p\big) g_j\big(\phi_j(t)\big), \end{aligned} \tag{2.3}$$

where $0 < x_F \leq 1$, $K_t, K_r > 0$ and $K_{te}, K_{re} \geq 0$ are cutting parameters, and a_p is the axial depth of cut. The function $g_j\big(\phi_j(t)\big)$ describes whether a tooth is in or out of cut:

$$g_j\big(\phi_j(t)\big) = \begin{cases} 1, & \phi_s \leq \phi_j(t) \leq \phi_e \wedge h_j(t) > 0, \\ 0, & \text{else.} \end{cases} \tag{2.4}$$

Via trigonometric functions, the force can easily be converted to x (feed) and y (normal) direction. This force interacts with the spindle and tool dynamics (block Machine) in Figure 2.1, modelled via a linear state-space model,

$$\begin{aligned} \dot{z}(t) &= \mathbf{A} z(t) + \mathbf{B} F(t), \\ v(t) &= \mathbf{C} z(t), \end{aligned} \tag{2.5}$$

where z is the state (the order of this model primarily depends on the order of the spindle-tool dynamics model). This results in a dynamic displacement of the tool $v(t)$ which is superimposed on the predefined tool motion. The dynamic chip thickness is the result of this displacement $v(t) = \begin{bmatrix} v_x(t) & v_y(t) \end{bmatrix}^T$ and the displacement of the cutter at the previous tooth pass at time $v(t-\tau)$. This is called the regenerative effect and results in the block Delay in Figure 2.1. Via trigonometric relations, the tool motion results in a dynamic chip thickness $h_{j,dyn}(t)$ given by,

$$h_{j,dyn}(t) = \begin{bmatrix} \sin \phi_j(t) & \cos \phi_j(t) \end{bmatrix} \big(v(t) - v(t-\tau)\big), \tag{2.6}$$

which is added to the static chip thickness. We introduce Z as the number of teeth of the end-mill. Hence, when summing for all Z teeth, the cutting forces in x- and y-direction can be described by

$$F(t) = a_p \sum_{j=0}^{Z-1} g_j\big(\phi_j(t)\big) \left(\Big(h_{j,stat}(t) + \begin{bmatrix} \sin \phi_j(t) & \cos \phi_j(t) \end{bmatrix} \big(v(t) - v(t-\tau)\big)\Big)^{x_F} \mathbf{S}(t) \begin{bmatrix} K_t \\ K_r \end{bmatrix} + \mathbf{S}(t) \begin{bmatrix} K_{te} \\ K_{re} \end{bmatrix} \right), \tag{2.7}$$

with $F(t) = \begin{bmatrix} F_x(t) & F_y(t) \end{bmatrix}^T$ and $F_x(t)$ and $F_y(t)$ the cutting forces in x- and y-direction, respectively, and

$$\mathbf{S}(t) = \begin{bmatrix} -\cos \phi_j(t) & -\sin \phi_j(t) \\ \sin \phi_j(t) & -\cos \phi_j(t) \end{bmatrix}.$$

Substitution of (2.7) in (2.5) yields the delay differential equations describing the milling process,

$$\begin{aligned}\dot{z}(t) =&\mathbf{A}z(t) + \mathbf{B}a_p \sum_{j=0}^{Z-1} g_j\big(\phi_j(t)\big)\Bigg(\Big(h_{j,stat}(t) + \begin{bmatrix}\sin\phi_j(t) & \cos\phi_j(t)\end{bmatrix}\\ &\mathbf{C}\big(z(t) - z(t-\tau)\big)\Big)^{x_F}\mathbf{S}(t)\begin{bmatrix}K_t\\K_r\end{bmatrix} + \mathbf{S}(t)\begin{bmatrix}K_{te}\\K_{re}\end{bmatrix}\Bigg),\\ v(t) =&\mathbf{C}z(t).\end{aligned} \tag{2.8}$$

Model (2.8) is used to describe the milling process for different tool-toolholder-spindle combinations (each of which leads to different "Machine" dynamics (2.5)). The goal in this thesis is to find a method to determine the dynamics of the tool-toolholder-spindle combinations. Therefore, the focus is on the dynamics of the tool-toolholder-spindle-system combination (2.5) of the milling machine; i.e. the second block in Figure 2.1 named Machine: This part represents the modelling of the tool-spindle dynamics, i.e. the tool, toolholder and spindle. The variety of tools, toolholders and spindles used in combination with each other has a great influence on the machine dynamics, see [8]. Nowadays, these dynamics are commonly measured with hammer-tests: Herein, the system is manually excited with a calibrated force hammer inducing a time-varying displacement, see [23]. The combination of the time history of impact force and displacement can be used to determine the dynamics of that particular system (i.e. the specific tool-toolholder-spindle-system combination). This identification process has to be repeated for every single tool-toolholder-spindle system combination which is time consuming and, therefore, undesirable. Therefore, it is necessary to use an accurate method that can identify the dynamics for all possible tool, toolholder and spindle combinations in an efficient way. These dynamics can then be incorporated in the HSM model (2.8) for effective prediction of chatter vibrations.

Many possible combinations exist for the tool-toolholder-spindle system. Therefore, the total combination is divided into two substructures. All the different tools are considered as a substructure and all the toolholder-spindle combinations are considered as a substructure. These substructures can be combined to form the desired tool-toolholder-spindle-system combination. The advantage of this method compared to impulse hammer-tests is that the identification of the substructures can take place off-line. The modelling and identification of substructures and coupling of substructures will be discussed in the next chapter.

Chapter 3

Coupling of substructures

Since the 1960s, substructuring has been used to model complex mechanical structures. Substructuring involves dividing the structure to be evaluated into a number of substructures, or components. For each component, a model is obtained and then these models are assembled into a model of the entire joint structure. These models are mostly obtained by the application of first principles (such as Newton's second law) or experiments. The primary uses of dynamic substructuring are: the coupling of reduced-order models of moderately complex structures (e.g. airplane components or systems of automotive components) and the coupling of substructures that are exchangeable or modifiable.

3.1 Substructuring

A substructure can be described by a defined part of the total system. The total structure must fulfil the following properties:

- the total system should consist of more than one component,
- the components are attached to each other through a discrete number of locations and
- the components show linear and time-invariant behavior.

The coupling methods of substructures can be classified into two groups:

- coupling in the time domain; component mode synthesis (CMS), see [28, 31, 82],
- coupling in the frequency domain using (measured) frequency response functions (FRFs); frequency domain structural synthesis (FSS), see [33, 80, 82].

Model reduction is one of the major objectives in CMS. The mode set describing the dynamics of a substructure is usually reduced to a smaller set of modes. To apply CMS, it is necessary to describe the substructures with a model, for example modelling with Lagrange-Euler equations. By applying a Lagrange multiplier-based generalized substructure coupling procedure, these equations can be coupled [14]. The result is one total Lagrange-Euler equation which can be used for further analysis of the overall dynamics.

In the mid-1960s, Hurty published several reports and papers on substructure coupling in the time domain [30, 31]. In collaboration with Hurty, Bamford created a CMS computer program that employed several kinds of modes [5]. A simplification of Hurtys method was presented by Craig and Bampton in 1968 [15], and in the early 1970s, MacNeal and Rubin introduced important alternatives to Hurtys CMS method [39, 53]. A number of CMS methods are described and compared in [6]. Nowadays most finite element (FE) programmes, such as Ansys [34] or MSC/NASTRAN [12], use the CMS coupling method in the time domain.

Frequency-domain techniques for linear structural synthesis (FSS) are not new in themselves; the basic equation for synthesis can be found in many references. An application of frequency-domain techniques to structural analysis appeared in 1946, see Sofrin [69]. Sykes [72] derived the same equation for structural synthesis as Sofrin. The derivations are based on an implicit statement of force and displacement continuity between the substructures known as the compatibility and equilibrium conditions:

$$\begin{aligned} x_S = &\quad x_1 = x_2 = ... = x_n, \\ F_S = &\quad \sum_{i=1}^{n} F_i, \end{aligned} \tag{3.1}$$

where x_S represents the displacement of, and F_S represents the resulting force acting on the connection coordinate on the assembly S, x_1 and x_2 until x_n represent the displacements of, and F_1 until F_n represent the forces acting on the connection coordinates (1 until n) on the substructures where n is the chosen number of connection coordinates. The coupling of FRFs can be done with two different methods: the impedance coupling (IC) technique and the receptance coupling (RC) technique. Research on these techniques can be found in [51] and an implementation of the IC and RC technique can be found in [33] and [80], respectively. The IC technique translates the compatibility and equilibrium conditions into a matrix representation concerning all the degrees of freedom (DOFs) of the substructures. In this way, the technique satisfies the criterium of physical generality, meaning that the calculation satisfies the laws of physics. It is also very simple to implement. However, this technique is computationally inefficient, since two inversions of the full size substructure matrices are required. Because the full size matrix inversion is required, the numerical error can be significant. When the full size receptance matrix is singular, the IC technique collapses and no results can be obtained at all. In this prospect the IC method is not reliable. The requirement of the inversions of the full size substructure matrices and the computationally inefficiency makes the IC technique unpractical for our tool-toolholder-spindle-system application.

The principle of RC or receptance coupling substructure analysis (RCSA) is described in [7]. The term "receptance" as used by Bishop and Johnson is, for this purpose, equivalent to FRF. Bishop and Johnson provide analytic expressions for the receptances of simple beams. Later on, the receptance technique is used in all kind of fields, e.g. automotive engineering [17], evaluating dynamic characteristics of design alternatives for a reconfigurable machine tool (RMT) in an automated design environment [83], micro cutting [10] and aerospace engineering [4]. This wide variety of applications shows that RC has a lot of potential. The main reason for this wide use of the RC technique is the advantage that the RC technique requires only one matrix inversion. The size of the matrix to be inverted is determined by the number of joint coordinates on the assembly, which can be chosen by the user and is usually much smaller than the size of the whole receptance matrix. It is also more likely to be a well-conditioned matrix because of the much smaller size compared to the matrices used in the IC technique. In other words, the RC technique is mathematically more robust and computationally more efficient than the IC technique. However, the RC technique is not applicable to cases in which two coordinates to be coupled are located on the same structure. This means that the substructures must be independent of each other. The RC technique has advantages especially in an experimental environment. Firstly, often FRFs are the quantities which are measured directly. Secondly, in general, the final number of coupling degrees of freedom plus interesting internal degrees of freedom will be relatively small. Also characteristic features, e.g. irregularities and the type and level of damping of the structure, are inherently present in the measurements of the FRFs.

The possibility to choose the coupling degrees of freedom and internal degrees of freedom ourselves, the mathematical robustness in combination with the computational efficiency and the advantages in an experimental environment make this technique most appropriate for the

tool-toolholder-spindle-system application. In the next section, we will discuss the receptance coupling technique in more detail.

3.2 The receptance coupling technique

To minimize the size of the matrix to be inverted in the RC technique, a minimum number of coordinates should be picked on the assembly, which is, however, still enough to satisfy the compatibility and equilibrium conditions (3.1). The minimum number of coordinates to fulfil these conditions is two, one on each substructure and to evaluate the assembly on any spatial location, an additional coordinate on that spatial location is necessary. This makes the minimum number of coordinates three. A simple example of a structure fulfilling these conditions is illustrated in Figure 3.1. It is unnecessary to use more than three coordinates in the RC technique unless an additional coordinate on the structure is chosen to be evaluated. In Figure 3.1, the points i and c indicates the chosen internal and coupling coordinates,

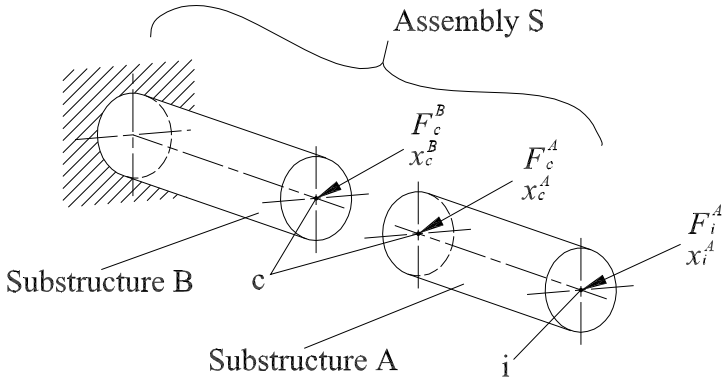

Figure 3.1: Minimum number of coordinates required for the RC technique.

respectively. In the remainder of this section, we will explain these coordinates in more detail. The translational DOFs $x_{i,c}^{A,B}$ are the DOFs of the internal (i) or coupling (c) coordinates of component A or B. The external forces $F_{i,c}^{A,B}$ are acting on the internal (i) or coupling (c) coordinates of component A or B. This notation of substructures, internal and coupling coordinates is used throughout this thesis. The assembly S is chosen to be evaluated on the free-end at point i. Therefore, coordinate x_i^A is picked on the tip, at point i, of the free-free substructure A. The other two coordinates x_c^A and x_c^B, at point c, are located on the cross-section, where the assembly is split into two substructures. These coordinates must be placed on the cross-section to make it possible to fulfill the compatibility and equilibrium conditions ($n = 2$ in (3.1)).

In this example, it may be possible that experiments can be performed directly on location i of the joint structure. In this case the RC technique is unnecessary. The RC technique is used in cases where this possibility to accurately measure assembly dynamics is not present. Either one of the substructures is exchangeable for a range of different substructures or one of the substructures is a model (e.g. based on finite-elements) resulting in hybrid methods. In hybrid methods, measured and modeled components are coupled using rigid, flexible, or flexible/damped compatibility conditions to predict the assembly response at any spatial location. In all of these cases, the RC technique is particularly helpful. Practical examples exist where the RC technique is used for different applications. For example, the RC technique is used to compensate for scaling and frequency distortion errors arising from non-ideal

sensor placement on mechanical structures [56]. Additionally, knowledge of the response at any location on the structure enables mode shape prediction and, therefore, selection of high signal-to-noise ratio sensor locations. Also complex models, with or without the application of reduction techniques, are coupled with the RC technique, for example in the automotive industry where the development of car-engines is performed separately from that of the carriage work of the car. These two components are then coupled with the RC technique for further analysis or optimization in the racing industry [16]. Analysis and optimization can be done without the physical coupling of the two components which reduces costs.

The RC technique is an FRF-based substructuring technique that predicts the dynamic behavior of the coupled system on the basis of free-interface FRFs of the uncoupled components. The basic strategy of an FRF-based receptance coupling technique is as follows. We define the substructure systems

$$\begin{aligned} x^A(j\omega) = &\quad H^A_{xF}(j\omega)F^A(j\omega), \\ x^B(j\omega) = &\quad H^B_{xF}(j\omega)F^B(j\omega), \end{aligned} \tag{3.2}$$

where superscript A and B represents the substructures A and B respectively, $F^{A,B}(j\omega)$ is the Fourier transform of the excitation (force) on a chosen DOF on the substructures A and B. $x^{A,B}(j\omega)$ is the Fourier transform of the response (displacement) vector of the chosen DOF of substructures A and B and $H^{A,B}_{xF}(j\omega)$ is the free-interface FRF matrix of the substructures A and B. ω represents the angular frequency and j equals $\sqrt{-1}$. For the sake of brevity, we will omit the notation $(j\omega)$ in the remainder of this thesis.

For every component, the available DOFs are classified into two sets, namely:

1. the coupling DOFs,
2. the internal DOFs.

Therefore, the indices c and i are used to represent the coupling and internal DOFs respectively, see Figure 3.1. The DOFs correspond with the excitation and response location of the uncoupled components. In this way, the substructures can be written in the partitioned form as

$$\begin{bmatrix} x_i^{A,B} \\ x_c^{A,B} \end{bmatrix} = \begin{bmatrix} H^{A,B}_{x_iF_i} & H^{A,B}_{x_iF_c} \\ H^{A,B}_{x_cF_i} & H^{A,B}_{x_cF_c} \end{bmatrix} \begin{bmatrix} F_i^{A,B} \\ F_c^{A,B} \end{bmatrix}, \tag{3.3}$$

with

- $H^{A,B}_{x_{(i,c)}F_{(i,c)}}$ the FRF matrix of component A or B between every combination of DOF i and c,
- $x^{A,B}_{(i,c)}$ the response on the internal (i) or coupling (c) DOFs of component A or B,
- $F^{A,B}_{(i,c)}$ the force on the internal (i) or coupling (c) DOFs of component A or B,
- i the subscript for the internal DOFs of component A and B,
- c the subscript for the coupling DOFs of component A and B.

In order to present the RC technique, we take the example of Figure 3.1, where the objective is to identify the FRF $H^S_{x_iF_i}$ at the free end of the total joint structure S (point i in Figure 3.1). There is no interest in evaluating the internal coordinates of substructure B. Then, only the DOF on the connection point of substructure B, x_c^B, is sufficient to identify the dynamics of substructure B to calculate the dynamics of the total joint structure S. Therefore, the substructure can be expressed in the coupling DOF, which yields:

$$x_c^B = H^B_{x_cF_c}F_c^B. \tag{3.4}$$

Substructure A is expressed in the minimum number of two DOFs namely the coupling DOF x_c^A and the internal DOF x_i^A. Substructure A is written in the partitioned form as follows:

$$\begin{bmatrix} x_i^A \\ x_c^A \end{bmatrix} = \begin{bmatrix} H_{x_iF_i}^A & H_{x_iF_c}^A \\ H_{x_cF_i}^A & H_{x_cF_c}^A \end{bmatrix} \begin{bmatrix} F_i^A \\ F_c^A \end{bmatrix}. \tag{3.5}$$

At the cross-section, the equilibrium and compatibility conditions (3.1) provide the following boundary conditions

$$\begin{aligned} F_c = &\quad F_c^A + F_c^B, \\ x_c = &\quad x_c^A = x_c^B. \end{aligned} \tag{3.6}$$

The force F_c is an external force which equals the sum of the two internal forces acting on the cross-section of the two substructures. Under equilibrium conditions, the sum of the two internal forces is equal to zero and no external force F_c will be present. The compatibility equation for x_c describes a kinematic coupling of the two substructure coordinates x_c^A and x_c^B. It is also possible to use flexible, or flexible/damped compatibility conditions to predict the assembly response [44].

Substitution of (3.4) and (3.5) into (3.6) yields:

$$\begin{aligned} x_c^B &= x_c^A \\ H_{x_cF_c}^B F_c^B &= H_{x_cF_i}^A F_i^A + H_{x_cF_c}^A F_c^A \\ &= H_{x_cF_i}^A F_i^A + H_{x_cF_c}^A \left(F_c - F_c^B\right) \\ F_c^B &= \left(H_{x_cF_c}^A + H_{x_cF_c}^B\right)^{-1} \left(H_{x_cF_i}^A F_i^A + H_{x_cF_c}^A F_c\right). \end{aligned} \tag{3.7}$$

From now on, the internal DOF x_i^A is called x_1 and the applied forces F_i^A and F_c are called F_1 and F_2, respectively. The internal DOF x_1 can be expressed as a function of the applied forces from the partitioned form presented in (3.5). If we include the boundary condition $F_c^A = F_2 - F_c^B$, we obtain the following equation of x_1:

$$x_1 = H_{x_iF_i}^A F_1 + H_{x_iF_c}^A \left(F_2 - F_c^B\right). \tag{3.8}$$

By substituting (3.7) into (3.8)

$$\begin{aligned} x_1 &= H_{x_iF_i}^A F_1 + H_{x_iF_c}^A F_2 - H_{x_iF_c}^A \left(\left(H_{x_cF_c}^A + H_{x_cF_c}^B\right)^{-1} \left(H_{x_cF_i}^A F_1 + H_{x_cF_c}^A F_2\right)\right) \\ &= \left(H_{x_iF_i}^A - H_{x_iF_c}^A \left(H_{x_cF_c}^A + H_{x_cF_c}^B\right)^{-1} H_{x_cF_i}^A\right) F_1 + \\ &\quad \left(H_{x_iF_c}^A - H_{x_iF_c}^A \left(H_{x_cF_c}^A + H_{x_cF_c}^B\right)^{-1} H_{x_cF_c}^A\right) F_2, \end{aligned} \tag{3.9}$$

we obtain an expression for x_1 as a function of the two applied forces F_1 and F_2. Since, the external force F_2 is zero, we obtain the following assembled FRF ($x_1 = H_{x_iF_i}^S F_1$) at the tip of the joint structure

$$H_{x_iF_i}^S = H_{x_iF_i}^A - H_{x_iF_c}^A \left(H_{x_cF_c}^A + H_{x_cF_c}^B\right)^{-1} H_{x_cF_i}^A. \tag{3.10}$$

With this equation, two substructures are coupled to form a assembled structure. This joint structure can be used for further analysis. Therefore, the RC technique is suitable for our tool-toolholder-spindle-system application. For obvious reasons this equation is called the coupling equation. This coupling equation is tested for its accuracy in an example of a four DOF mass-spring-damper model in the next section.

3.3 Receptance coupling applied to a 4DOF mass-spring-damper model

The example presented in Figure 3.1 is modeled in a 4DOF mass-spring-damper model. Substructures A and B are both modeled as 2DOF mass-spring-damper systems. Jointly these systems form the 4DOF mass-spring-damper assembly S as depicted in Figure 3.2.

Let us consider the 4DOF mass-spring-damper system to test the coupling equation (3.10). The goal is to obtain $H^S_{q_4F}$ by coupling substructures A and B. $H^S_{q_4F}$ represents the frequency response function from the input force (F) to translational displacement (q_4) on assembly S.

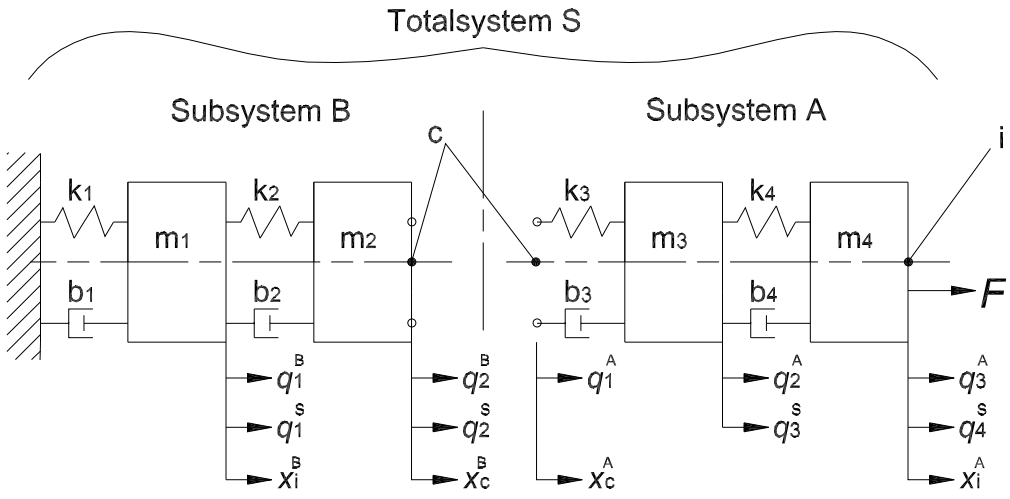

Figure 3.2: A 4DOF mass-spring-damper system consisting of two substructures.

The 2DOF subsystem A is a free-free system which is characterized by three generalized coordinates $q^A = \begin{bmatrix} q_1^A & q_2^A & q_3^A \end{bmatrix}^T$. The 2DOF subsystem B is supported at one end and is characterized by two generalized coordinates $q^B = \begin{bmatrix} q_1^B & q_2^B \end{bmatrix}^T$. The total system S is a 4DOF mass-spring-damper system that is clamped on one end. The total system S is characterized by four generalized coordinates $q^S = \begin{bmatrix} q_1^S & q_2^S & q_3^S & q_4^S \end{bmatrix}^T$. The number of generalized coordinates of the substructures and the total system are chosen differently. This shows that the individual number of generalized coordinates of the subsystems and total joint system are independent of each other. The parameters used for the masses, spring constants and damping-ratios are collected from a parameter-fit performed on a tool-spindle combination in [26]. The two most dominant modes of the tool and the two most important modes of the spindle of an HSM machine are used to parameterize subsystem A and B, respectively. The parameters characterizing these dynamics are shown in Table 3.1.

The three mass-spring-damper systems (subsystem A, subsystem B and the total system S) are each described by a mass matrix ($\mathbf{M}$), stiffness matrix ($\mathbf{K}$) and damping matrix ($\mathbf{D}$). This yields for subsystem A:

$$\mathbf{M}^A = \begin{bmatrix} 0 & 0 & 0 \\ 0 & m_3 & 0 \\ 0 & 0 & m_4 \end{bmatrix}, \quad \mathbf{K}^A = \begin{bmatrix} k_3 & -k_3 & 0 \\ -k_3 & k_3 + k_4 & -k_4 \\ 0 & -k_4 & k_4 \end{bmatrix}, \quad \mathbf{D}^A = \begin{bmatrix} b_3 & -b_3 & 0 \\ -b_3 & b_3 + b_4 & -b_4 \\ 0 & -b_4 & b_4 \end{bmatrix},$$

	i=1	i=2	i=3	i=4
$m_i[kg]$	0.8705	0.3301	0.03228	0.01574
$k_i[N/m]$	$4.271 \cdot 10^7$	$3.075 \cdot 10^7$	$2.481 \cdot 10^7$	$2.229 \cdot 10^7$
$b_i[Ns/m]$	0.04348	0.03551	0.04754	0.03364

Table 3.1: Parameters used in the 4DOF mass-spring-damper model.

for subsystem B

$$\mathbf{M}^B = \begin{bmatrix} m_1 & 0 \\ 0 & m_2 \end{bmatrix}, \quad \mathbf{K}^B = \begin{bmatrix} k_1 + k_2 & -k_2 \\ -k_2 & k_2 \end{bmatrix}, \quad \mathbf{D}^B = \begin{bmatrix} b_1 + b_2 & -b_2 \\ -b_2 & b_2 \end{bmatrix},$$

and for the total system S

$$\mathbf{M}^S = \begin{bmatrix} m_1 & 0 & 0 & 0 \\ 0 & m_2 & 0 & 0 \\ 0 & 0 & m_3 & 0 \\ 0 & 0 & 0 & m_4 \end{bmatrix}, \quad \mathbf{K}^S = \begin{bmatrix} k_1 + k_2 & -k_2 & 0 & 0 \\ -k_2 & k_2 + k_3 & -k_3 & 0 \\ 0 & -k_3 & k_3 + k_4 & -k_4 \\ 0 & 0 & -k_4 & k_4 \end{bmatrix},$$

$$\mathbf{D}^S = \begin{bmatrix} b_1 + b_2 & -b_2 & 0 & 0 \\ -b_2 & b_2 + b_3 & -b_3 & 0 \\ 0 & -b_3 & b_3 + b_4 & -b_4 \\ 0 & 0 & -b_4 & b_4 \end{bmatrix}.$$

The FRFs of the individual systems are calculated from the $\mathbf{M}$, $\mathbf{K}$ and $\mathbf{D}$ matrices with a damped MIMO frequency response function for linear systems

$$H_{x_{i,c}F_{i,c}} = \left(-\omega^2\mathbf{M} + j\omega\mathbf{D} + \mathbf{K}\right)^{-1}, \tag{3.11}$$

in which $H_{x_{i,c}F_{i,c}}$ represents the frequency response function from the input force ($F_{i,c}$) to translational displacement ($x_{i,c}$) on the locations i and c, respectively. The derived FRFs of subsystem A are written in the partitioned form. Again, substructure B is not presented in the partitioned form because there is no internal coordinate of interest on substructure B to be evaluated:

$$\begin{aligned} \begin{bmatrix} x_i^A \\ x_c^A \end{bmatrix} &= \begin{bmatrix} H^A_{x_iF_i} & H^A_{x_iF_c} \\ H^A_{x_cF_i} & H^A_{x_cF_c} \end{bmatrix} \begin{bmatrix} F_i^A \\ F_c^A \end{bmatrix}, \\ x_c^B &= H^B_{x_cF_c} F_c^B. \end{aligned} \tag{3.12}$$

The result of the application of the coupling equation (3.10) with the calculated FRFs (as in 3.11) is displayed in Figure 3.3. The left two figures are (from top to bottom) the magnitude and phase of $H^S_{x_iF_i}$. In these left figures, two FRFs are presented; the first FRF shown is $H^S_{x_iF_i}$ derived from the equations of motion which is derived with Newton's second law by using the $\mathbf{M}^S$, $\mathbf{K}^S$ and $\mathbf{D}^S$ matrices of the total joint structure S. The second FRF $H^S_{x_iF_i}RC_{method}$ is calculated with the coupling equation (3.10) of the RC technique. The right figures represent the absolute error between these FRFs in magnitude and phase, respectively. The two FRFs match perfectly. The error is very small and only due to numerical round off errors, concluding that the RC technique is exact.

With the RC technique, it is not only possible to couple substructures to form an assembly, but also the decoupling of the assembly into substructures is possible (as explained in the next section).

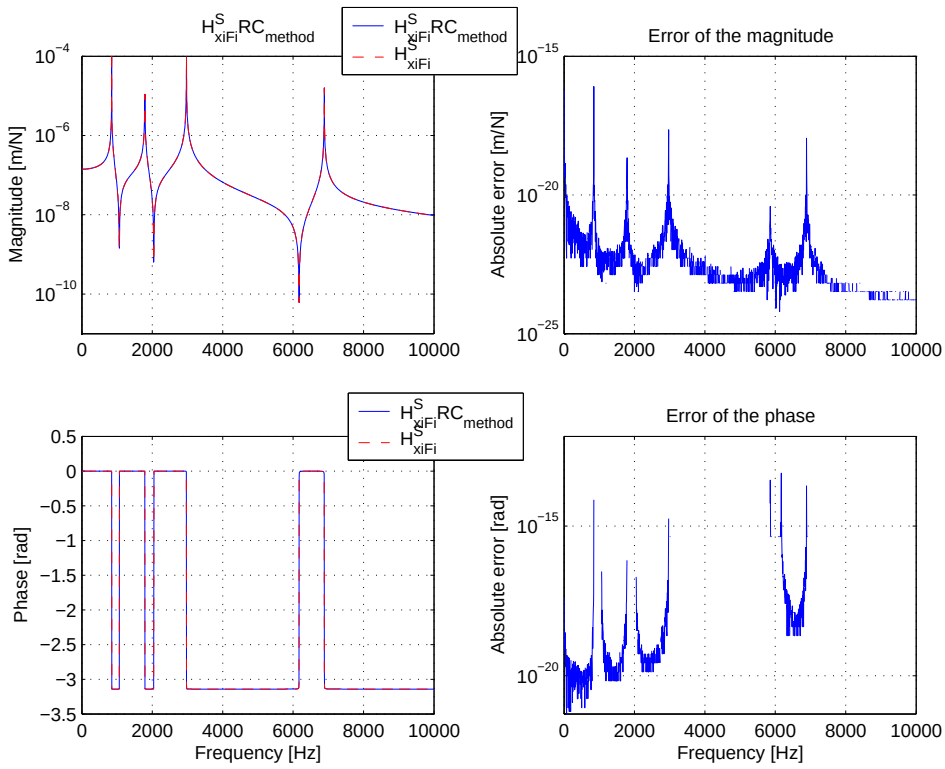

Figure 3.3: RC calculation of $H^S_{x_iF_i}$ for the 4DOF mass-spring-damper system.

3.4 Decoupling of substructures

The system of interest that needs to be evaluated can be one of the substructures instead of a total joint structure. The ability to accurately measure assembly dynamics allows data recorded at one location on the structure to be compensated by the structural dynamics between the measurement point and actual location of interest. For example, consider a system as depicted in Figure 3.1, where the system under evaluation is substructure B while the assembled system S consists of the joint substructures A and B. Suppose that we aim to obtain the dynamics of substructure B of the joint structure S from which substructure A and B can not be physically detached to perform individual measurements. Then, only measurements on the assembled structure S can be performed. Suppose that the dynamics of substructure A can be modeled (in this case e.g. beam-theories [32, 84] can be applied). Then, the inverse receptance coupling (IRC) technique can be applied to decouple the dynamics of substructure B from assembly S. In other words, the dynamics of substructure B can be derived by using the dynamics of assembly S and substructure A [56]. The background on this IRC technique is the following.

The derived coupling equation (3.10) for the RC technique is an equation with complex scalar numbers. Therefore, this equation can be considered in the same way as any other normal scalar equation; only the coupling equation needs to be evaluated for every single frequency in the frequency domain of interest. This quality makes it possible to rewrite the coupling equation such that an explicit expression for every FRF, used in the coupling equation, can be obtained. This is the basic idea behind the IRC technique also known as the inverse receptance coupling substructure analysis (IRCSA).

In the next section, the IRC technique is illustrated by applying it on the 4DOF mass-spring-damper system presented in Figure 3.2.

3.5 Inverse receptance coupling with a mass-spring-damper model

We assume that the dynamics of subsystem B of the system presented in Figure 3.2 needs to be evaluated. With the IRC technique the dynamics of subsystem B can be derived from the measurements performed on the assembly S and subsystem A. The ability to measure assembly dynamics allows data recorded at one location on the structure to be compensated by the structural dynamics between the measurement point and actual location of interest.

To test the IRC technique on its accuracy, the FRF $H^B_{x_cF_c}$ in the 4 DOF mass-spring-damper model (see Section 3.3) is written explicitly from the coupling equation (3.10):

$$H^B_{x_cF_c} = \left(H^S_{x_iF_i} - H^A_{x_iF_i}\right)^{-1} H^A_{x_cF_c} \left(H^S_{x_iF_i} - H^A_{x_iF_i}\right) + H^A_{x_iF_c} H^A_{x_cF_i} \tag{3.13}$$

The result of the application of the IRC equation to the 4DOF model is displayed in Figure 3.4.

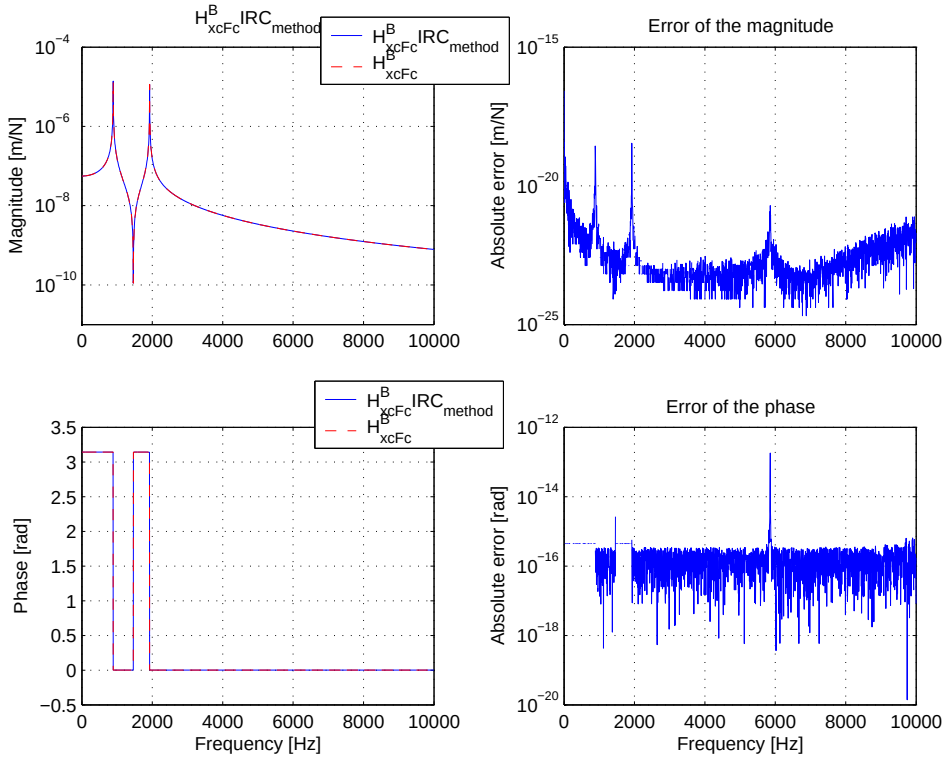

Figure 3.4: IRC calculation of H^B_{xcFc}.

The result is presented in the same way as in Figure 3.3. Two figures are presented on the left; the top figure is the magnitude of $H^B_{x_cF_c}$ and the bottom figure is the phase of $H^B_{x_cF_c}$. In these left figures, two FRFs are presented; the first FRF shown is $H^B_{x_cF_c}$ derived from the equation of motion obtained by applying Newton's second law on substructure B. The second FRF $H^B_{x_cF_c}IRC_{method}$ is calculated with the inverse receptance coupling equation (3.13) of the IRC technique. The right figures represent the absolute error between these FRFs in magnitude and phase, respectively. These two FRFs match perfectly. The error is very small concluding that in theory the IRC technique is exact.

Hence, it is shown that both the methods RC and IRC are exact.
In practice, the data used in the RC and IRC technique will not be as ideal as in the used 4DOF model. Therefore, the coupling (RC) and decoupling (IRC) of the 4DOF model are tested under the influence of measurement uncertainties in the next section.

3.6 Influence of measurement uncertainties on the coupling equation

The prediction of the dynamic behavior of a coupled structure can be obtained by (a) analytical modeling and (b) experimental modal analysis. Specifically, when the first approach is employed, first principles are used in order to formulate the equations of motion. The advantage is that it causes no problems due to measurement uncertainties such as measurement noise. By application of the second approach, namely the experimental analysis, measurements of FRFs are performed on the structures. A benefit of this approach is that characteristic features, i.e. irregularities and damping of the structure, are inherently present in the measurement. A drawback is the influence of measurement noise. This can cause poor results of the prediction of the coupled structure [29].

In this work, the influence of the measurement noise is tested in a model based environment. In the 4DOF mass-spring-damper system used for the testing of the RC and IRC technique, depicted in Figure 3.2, noise is added to the FRFs of the substructures. Then, the RC and IRC technique are tested with these FRFs added with noise. The results of these tests can be found in Appendix A. In these results of the RC and IRC calculations the important resonance frequencies of the structure are clearly visible but unfortunately, resonant frequencies also appear on unexpected frequencies. These unexpected frequencies are the natural frequencies of the substructures. Overall it can be concluded that the measurement noise makes the RC and IRC technique less accurate. It can be concluded that it is of great importance for the accuracy of the result of the coupling equation (3.10) that the response data of the substructures is as accurate as possible.

The influence of measurement noise can be reduced. This can be done by averaging all the measurement results for each individual structure to one averaged FRF for all the FRFs used in the RC and IRC technique. An average of a total of ten equivalent measurements proved to be sufficient for a reliable averaged FRF in this case. Then, this averaged FRF is without the turbid of the noise, which is causing the undesired resonance peaks of the natural frequencies of the substructure in the RC and IRC result. The measurements performed on the HSM machine are therefore averaged to perform a proper RC and IRC calculation using measured FRFs of the HSM machine.

The error that still can occur by averaging FRFs is the performance of biased measurements. By performing biased measurements, the response data of the substructures are not accurate. To investigate the influence of biased response data of the substructures on the coupling result, tests are performed with shifted resonance peaks of substructure A, as in Figure 3.5 where $H^A_{x_cF_c biased}$ has shifted resonance peaks and $H^A_{x_cF_c}$ is derived with the use of Newton's second law. In the upper and lower left plots both $H^A_{x_cF_c biased}$ and $H^A_{x_cF_c}$ are plotted in magnitude and phase, respectively. In the right figures, the absolute errors of the magnitude and the phase are presented. An error is inserted to the location of the resonance and anti-resonance peaks of substructure A. Substructure B is assumed to be measured accurately. The result of the RC calculation with the shifted resonances of substructure A is presented in Figure 3.6. The left figures represent the magnitude and phase of the calculated FRF $H^S_{x_iF_i} RC_{technique}$. The result is compered with $H^S_{x_iF_i}$ of the total coupled structure derived with the use of Newton's second law. In the right figures, the absolute errors of the magnitude and phase are presented. In these right figures, the coupling result is clearly affected by the influenced substructure A. The resonance and anti-resonance peaks of the joint structure S are shifted. It can be concluded that the RC technique handled the influenced substructure A as an other structure with other resonance and anti-resonance peaks. In practice, the detection of such an error is difficult; this states the importance of the accuracy of the response data of the substructures. The response data of the substructures must be as accurate as possible. This conclusion is also supported by the performed IRC calculation with

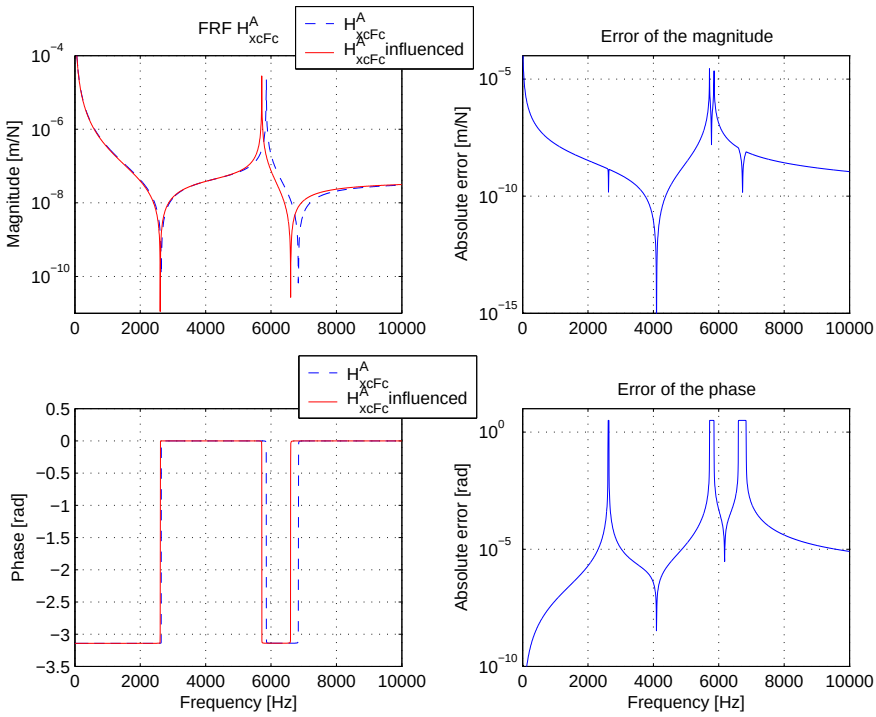

Figure 3.5: $H^A_{x_cF_c}$, biased measurements.

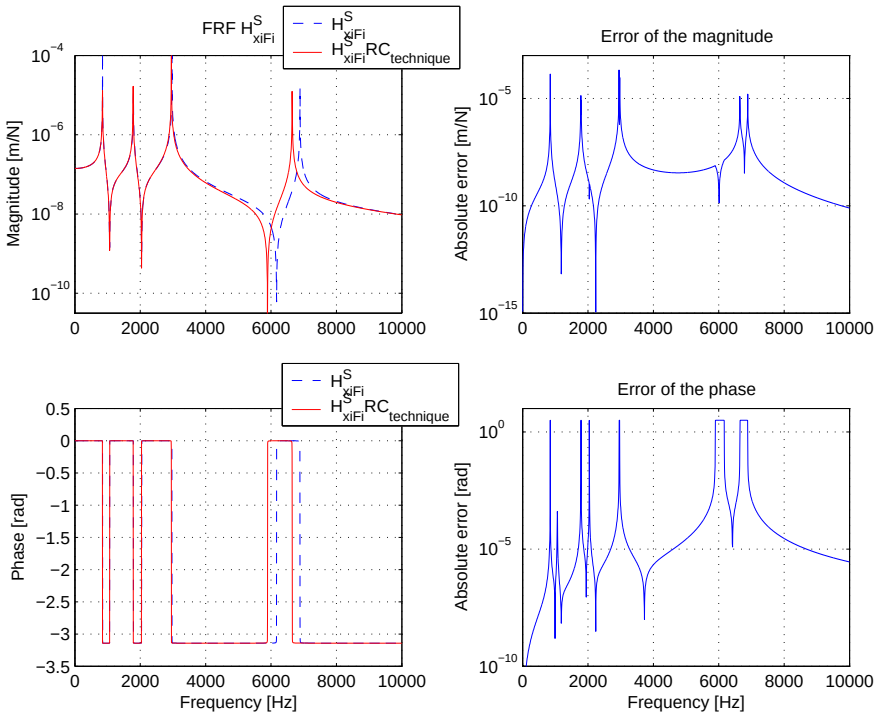

Figure 3.6: $H^S_{x_iF_i}$ calculated with the RC technique.

the inaccurately measured substructure A and accurately measured assembly S. This result can be found in Appendix B.

Chapter 4

Modelling of the tool-spindle dynamics

The RC and IRC technique will be used to couple the tool dynamics with the toolholder-spindle dynamics. By coupling the models for the tool dynamics and the toolholder-spindle combination, joint models for every tool-toolholder-spindle combination can be calculated efficiently based on these submodels.

A major difficulty for the choice of the location of the cross-section between these submodels is the determination of the dynamics at the intersection of the two substructures, i.e. the stiffness and damping in the cross-section. The location of the cross-section and the dynamics at the cross-section are linked with each other, and create different possibilities for the coupling of the modeled components using rigid, flexible, or flexible/damped compatibility conditions. This results in a great variety of strategies of the RC technique for modelling the dynamics of the HSM machine. These variations are presented throughout the years in the references [1, 8, 11, 21, 36, 44, 45, 47, 48, 57–61, 65, 85]. For example, more than two substructures can be used [47, 65] and the modelling of cross-section stiffness and/or damping can be considered [1, 44, 45]. When considering dynamics in the intersection of two substructures, often an optimization method based on a genetic algorithm is employed to find parameters of the joint model in [44, 45]. Herein, for every tool-spindle combination the parameters of the joint model need to be adjusted to model the reality accurately. For a large number of tool-spindle combinations this constitutes a rather unpractical approach. In [57, 61], the RC technique (equivalent to forward RC used in these papers) and coupling parameters (for the cross-section stiffness and damping) are used to estimate the dynamics of the machine-tool combination. A disadvantage is that the coupling parameters must be fit accurately to have realistic results. This parameter fitting process is time consuming and therefore undesirable in our tool-toolholder-spindle application. It is preferred to use kinematic coupling because the determination of the dynamics at the cross-section is unnecessary. Another approach is proposed by Esterling et al. [21] and Kiefer [35]. They developed a non-contact electromagnetic measurement device to capture the machine and tool dynamics. A disadvantage of this approach is that this measurement has to be carried out for every individual machine-tool combination.

Therefore, other methods have been developed. Park et al. [47] use inverse RC. They use a force sensor in the spindle of the HSM machine in combination with inverse RC techniques to calculate the FRFs that are difficult to measure. The difficulty of the measurement of some FRFs will be discussed in the following chapters. With the FRFs calculated with inverse RC techniques, Park estimates the dynamics of the tool- HSM machine combination off-line. Hereby, Park uses finite element analysis (FEA) to model the end-mill. A drawback of this approach is that every HSM machine under evaluation needs to be equipped with a force sensor integrated in the spindle, which is a costly and large-scaled undertaking. Another,

similar approach is presented by Schmitz et al. [58, 59, 61, 65]. He presents a finite element modeling approach to determine the stiffness and damping behavior between the tool and toolholder in thermal shrink fit conditions. Moreover, the spindle of the HSM machine is decoupled from the toolholder, creating three substructures. Then, RC techniques are used to couple the three substructures off-line. Here, a drawback is that the determination of the dynamics in the cross-sections takes a lot of effort and the coupling result is very sensitive for errors. Esterling [22] also calculates the toolholder-spindle combinations off-line. Hereby, Esterling uses analytic equations to describe the free-free supported tool. The disadvantage is that the tool is approximated by applying beam theories [32, 84] instead of using, generally more accurate, FE modelling. The variation in geometry of the range of tools used in an average HSM machine can not be presented by the simple geometry of a beam. This implies an error in the accuracy of the receptance data of the end-mill.

Therefore, in this work FE calculation, kinematic coupling in the RC and IRC techniques are used off-line to calculate the joint models of the tool-toolholder-spindle combinations.

4.1 Substructuring on the HSM machine

Commonly, the dynamics of a specific tool-toolholder-spindle combination as a whole is determined by performing hammer experiments. A typical HSM machine has as many as 50 to 100 tools in its tool carrousel, leading to a large number of measurements, that is for every tool, toolholder, spindle, HSM machine combination. This is a time-consuming process, which has to be repeated for every tool-toolholder-spindle combination.

In this work, we aim at increasing the efficiency of this identification process. We aim to do so by separately modelling, firstly, the tool dynamics and, secondly, the toolholder-spindle dynamics. By coupling these models, joint models for every tool-toolholder-spindle combination are available. This method does not require on-line measurements on the required tool-toolholder-spindle combinations on the HSM machine. The aim is to identify the dynamics of the joint HSM machine coupling combinations, in terms of FRFs from a force at the tip of the tool where the tool comes in contact with the milling-material to a displacement of the tool-tip. The location at the tip of the tool is the point of the tool that is excited during the milling process.

By choosing the cross-section as indicated in Figure 4.1, at the free-free end of the end-mill the dynamics of the cross-section are considered stiff. Now, a kinematic coupling assumption is valid because displacements and accelerations acting on the cross-section dynamics are negligibly small. The cross-section divides the total structure S into two substructures: substructure A and substructure B. Substructure A represents the free-free part of the end-mill and substructure B represents the HSM machine, spindle, toolholder and fixed part of the end-mill, respectively.

These substructures are used in the derived coupling equation (3.10). The coupling equation (3.10) only includes translational DOFs (TDOFs). However, rotational degrees of freedom (RDOFs) have to be taken into account as independent coordinates because the location of interest is on the tip of the tool where the tool is excited during the milling process [38].

4.2 Rotational FRFs

Various authors have discussed the inclusion of RDOFs in dynamic models. In coupling techniques, the consideration of rotations in the coupling coordinates may be decisive, as they can be responsible for force or moment transmissions between the various substructures [24, 52]. Furthermore, the combined use of translations and rotations may reduce the number of measurements that are necessary to represent the vibration with an accuracy identical to

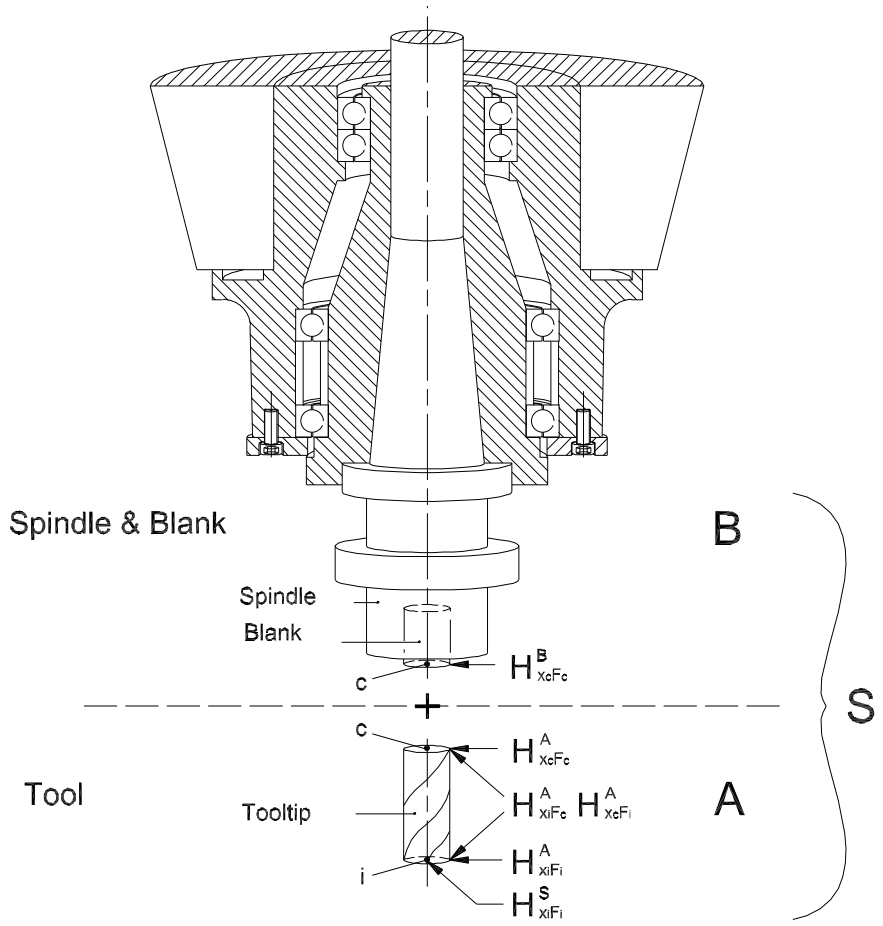

Figure 4.1: Substructures of the HSM machine.

the one which would be obtained by measuring only translations [9]. Therefore, the coupling equation derived with TDOFs (3.10) is extended with RDOFs.

Now, the FRFs in the coupling equation (3.10) contains both TDOFs and RDOFs defined by

$$\begin{bmatrix} x_\alpha \\ \theta_\alpha \end{bmatrix} = \begin{bmatrix} H^I_{x_\alpha F_\beta} & H^I_{x_\alpha M_\beta} \\ H^I_{\theta_\alpha F_\beta} & H^I_{\theta_\alpha M_\beta} \end{bmatrix} \begin{bmatrix} F_\beta \\ M_\beta \end{bmatrix} =: \mathbf{H}^I_{\alpha\beta} \begin{bmatrix} F_\beta \\ M_\beta \end{bmatrix},$$

where subscripts $\alpha, \beta \in \{i, c\}$ represents the relation to the internal or coupling DOF, superscript $I \in \{A, B, S\}$ represents substructure A or B or the assembly S, $H_{\alpha\beta}$ represent the specific FRF matrix where the input and output are determined by α and β, respectively and θ_α and M_β represent the rotational response and input momentum on the chosen internal or coupling RDOF, respectively. This can be done for all the components in equation (3.10), yielding:

$$\mathbf{H}^S_{ii} = \begin{bmatrix} H^A_{x_iF_i} & H^A_{x_iM_i} \\ H^A_{\theta_iF_i} & H^A_{\theta_iM_i} \end{bmatrix} - \begin{bmatrix} H^A_{x_iF_c} & H^A_{x_iM_c} \\ H^A_{\theta_iF_c} & H^A_{\theta_iM_c} \end{bmatrix} \tag{4.1}$$

$$\left(\begin{bmatrix} H^A_{x_cF_c} & H^A_{x_cM_c} \\ H^A_{\theta_cF_c} & H^A_{\theta_cM_c} \end{bmatrix} + \begin{bmatrix} H^B_{x_cF_c} & H^B_{x_cM_c} \\ H^B_{\theta_cF_c} & H^B_{\theta_cM_c} \end{bmatrix} \right)^{-1} \begin{bmatrix} H^A_{x_cF_i} & H^A_{x_cM_i} \\ H^A_{\theta_cF_i} & H^A_{\theta_cM_i} \end{bmatrix}.$$

Because we are only interested in the relation between the force and the displacement on the tip of the tool on the HSM machine ($H^S_{x_iF_i}$) the number of required FRFs can be reduced. We introduce the term kernel matrix for the matrix inversion in (4.1). This kernel matrix can

be notated more briefly

$$\left(\begin{bmatrix} H^A_{x_cF_c} & H^A_{x_cM_c} \\ H^A_{\theta_cF_c} & H^A_{\theta_cM_c} \end{bmatrix} + \begin{bmatrix} H^B_{x_cF_c} & H^B_{x_cM_c} \\ H^B_{\theta_cF_c} & H^B_{\theta_cM_c} \end{bmatrix} \right)^{-1} =: \begin{bmatrix} H_{2,x_cF_c} & H_{2,x_cM_c} \\ H_{2,\theta_cF_c} & H_{2,\theta_cM_c} \end{bmatrix}^{-1},$$

where $H_{2,q_cR_c} := (H^A_{q_cR_c} + H^B_{q_cR_c})$ for each element $(q \in \{x, \theta\})$ and $(R \in \{F, M\})$. The inversion of the kernel matrix can be expressed in a simpler notation by making use of the Kramer notation [37]:

$$\begin{bmatrix} H_{2,x_cF_c} & H_{2,x_cM_c} \\ H_{2,\theta_cF_c} & H_{2,\theta_cM_c} \end{bmatrix}^{-1} = \frac{1}{H_{2,\theta_cF_c}H_{2,x_cM_c} - H_{2,\theta_cM_c}H_{2,x_cF_c}} \begin{bmatrix} -H_{2,\theta_cM_c} & H_{2,x_cM_c} \\ H_{2,\theta_cF_c} & -H_{2,x_cF_c} \end{bmatrix}. \tag{4.2}$$

By using this representation of the kernel matrix (4.2) while evaluating the (1,1) element of $\mathbf{H}^S_{ii}$, representing $H^S_{x_iF_i}$, $H^S_{x_iF_i}$ can be expressed as

$$H^S_{x_iF_i} = \frac{x_1}{F_1} = H^A_{x_iF_i} + \frac{1}{H_{2,\theta_cF_c}H_{2,x_cM_c} - H_{2,\theta_cM_c}H_{2,x_cF_c}}$$

$$(H^A_{x_iF_c}H_{2,\theta_cM_c} - H^A_{x_iM_c}H_{2,\theta_cF_c})H^A_{x_cF_i} + (H^A_{x_iM_c}H_{2,x_cF_c} - H^A_{x_iF_c}H_{2,x_cM_c})H^A_{\theta_cF_i}. \tag{4.3}$$

This coupling equation consists of both TDOFs and RDOFs at the substructure interface. In an ideal situation, one would assume that all the TDOFs and RDOFs on the HSM machine can be measured accurately. Under such ideal circumstances, the coupling equation consisting of both TDOFs and RDOFs is tested in a 6DOF mass-spring-damper model. This model can be found in Appendix C. The results show that this coupling equation consisting of both TDOFs and RDOFs is exact.

Obviously, in practice, the ideal circumstances as in the 6DOF model in Appendix C can not be achieved. An additional problem is that, in particular, the possibilities for measuring responses at RDOFs are limited [55]. The measurement equipment used nowadays allows for obtaining the relationships between TDOFs and applied forces with high accuracy. However, the other RDOF relations are often not considered because of the difficulties in applying a pure moment excitation or in measuring rotational responses [42, 81]. In general, this implies a reduction of the complete dynamic model, in which relations to RDOFs will not be modeled. On the other hand, if an RC or IRC calculation includes rotational inertia, the rotational receptances of the unmodified system are needed. Nowadays, it is recognized that RDOFs (and hence rotational FRFs) may represent an important role in the characterization of the dynamic behavior of structures [18]. In our tool-toolholder-spindle coupling application we deal with rotational inertias, so the rotational FRFs must be calculated or determined experimentally.

In one experimental method, a so-called T-block is attached to the structure [81]. Then, a force, applied to an arm of the T-block, generates a moment together with a force at the connection point. The T-block also allows for angular displacement measurements. Nevertheless, the results are often not quite satisfactory. Therefore, the identification of the dynamics of the substructures A and B needs additional study.

4.3 Identification of substructure A

Similar to the receptance coupling technique proposed by Schmitz et al. [58, 61], the structural dynamics model of the end-mill at its two free ends can be modeled analytically using continuous beam formulations [57], finite element techniques [16] or it can be measured in practice.

In this application, the RDOFs of the end-mills (substructure A) can not be measured in practice without cutting through one of all the end-mills that need to be evaluated. Cutting

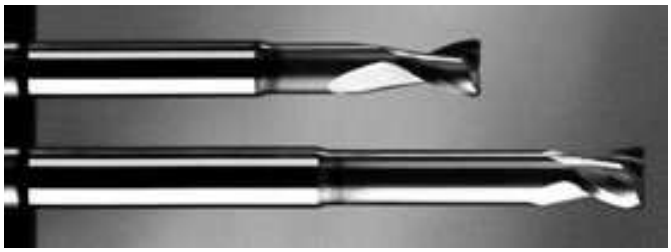

Figure 4.2: Substructure A, end-mill JH421100R080Z2-Mega-T.

through one of all the different end-mills constituting in the collection of tool-toolholder-spindle-system combinations is not an option from the cost-effectiveness point of view. Moreover, this will be rather time consuming. Moreover, considering the range of tools on the HSM machine, the smaller end-mills do not provide enough attachment area to apply a T-block. Therefore, the rotational FRFs of substructure A (the end-mill) must be computed.

Calculation of the rotational FRFs can be performed with the aid of FE programmes or by using analytic equations. Expressing the range of tools by using approximations such as cylindrical shapes in analytic equations takes a lot of categorization of the different tools and calculations are less accurate compared to a finite element analysis (FEA). Therefore, in this thesis we use FE calculations. An advantage of using FE calculations is that rotational FRFs are calculated in a straightforward fashion. A disadvantage is that the stiffness and damping characteristics are modeled (as opposed to measured); therefore, the material properties of the end-mill must be known. These material properties and tool geometry are provided by the manufacturer of the end-mills, Jabro-Tools, who is a partner in the Chattercontrol project. An end-mill that can be used as a specimen for the RC calculation is displayed in Figure 4.2.

4.3.1 Finite-element model of the end-mill

The substructure A depicted in Figure 4.1 represents the end-mill. The rotational FRFs and translational FRFs that need to be evaluated on the tip of the end-mill are depicted in more detail in Figure 4.3 where the inputs and outputs of the individual rotational and translational FRFs are presented by arrows and the rotational and translational FRF matrix is on the right. The FE calculations are performed with the FEM program Ansys [34]. Six (rotational) FRFs do not need to be calculated by using symmetry properties of the FRF. The free-free condition of the end-mill dynamics is needed because rigid body modes are important in the coupling of the substructures.

The 3-D tool geometry of the end-mills, necessary for the FE calculation, are obtained from the mill designer. The 3-D tool geometry of the end-mills is imported into the computer aided design (CAD) program UniGraphics. A manual for the exact implementation of the geometry of the end-mill into UniGraphics can be found in Appendix D.

Next, this geometric file (in UniGraphics) is imported in Ansys through the Ansys connection for UniGraphics. In Ansys, nodes are positioned on the desired locations where the FRFs need to be evaluated. Subsequently, the model is meshed using the SOLID 72 element type to evaluate both translational and rotational DOFs. Further calculations of the necessary FRFs for the coupling equation are performed in Matlab after exporting the mass and stiffness matrices to Matlab. The diagram in Figure 4.4 illustrates this procedure.

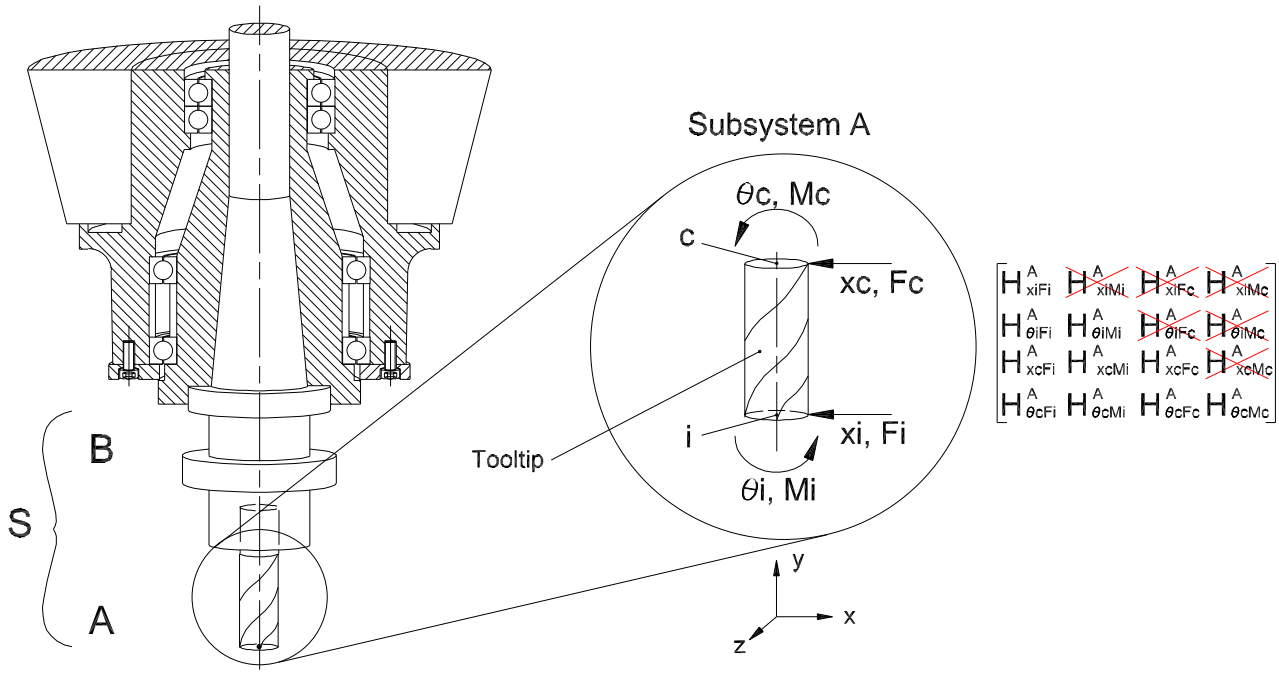

Figure 4.3: The required FRFs of substructure A, the end-mill.

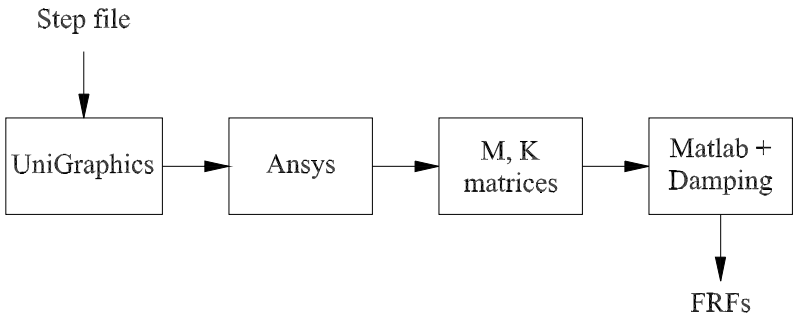

Figure 4.4: Diagram of the calculation procedure for the FRFs of subsystem A.

4.3.2 FRF calculation with Ansys and Matlab

Ansys does not support the calculation of the rotational FRFs in its dynamic design analysis toolbox. Therefore, the Modal Analysis solver in Ansys is only used to calculate the **M** and **K** matrices for the FE model of the end-mill. The matrices are computed without the influence of specific solvers in Ansys, thus without mode extraction or frequency range evaluation.

These matrices are exported to Matlab where the equations of motion (in first order form) are formed from the calculated **M**, **K** matrices. The assumed proportional damping is added to the equation of motion with the proportional damping matrix (**D**). A proportional damping model can easily be employed since the damping level (only due to material damping) is expected to be rather low. Let ω be the frequency of interest, $U(j\omega)$ the Fourier transform of the column of actual displacements, $j = \sqrt{-1}$ and $F(j\omega)$ represent the Fourier transform of the column of actual forces. Then,

$$\left(-\omega^2\mathbf{M} + j\omega\mathbf{D} + \mathbf{K}\right) U(j\omega) = F(j\omega), \tag{4.4}$$

where we will omit the $(j\omega)$ argument from now on. The imported **M** and **K** matrices have

a size equal to the total number of DOFs (m) used in the FE-model of the end-mill in Ansys. This size needs to be reduced. This is done by multiplying with the transpose of the matrix containing the eigenmodes introduced as the reduction matrix $\mathbf{T}$. Herein, $\mathbf{T}$ is a $m \times n$ matrix where n is equal to the number of reduced eigenmodes in $\mathbf{T}$. These eigenmodes are sorted with respect to the smallest eigenfrequency. The higher order modeshapes of the end-mill occur in very high frequencies where we have no interest in. Therefore, the first fourteen modeshapes, including the six rigid-modes, are used in the calculation and the rest is omitted, which gives

$$\mathbf{T}^T \left(-\omega^2 \mathbf{M} + j\omega \mathbf{D} + \mathbf{K}\right) U = \mathbf{T}^T F = F_T. \tag{4.5}$$

The reduced column of generalized forces is called F_T and is defined by $F_T = \mathbf{T}^T F$. Let Q be the Fourier transform of the reduced generalized coordinates such that

$$U = \mathbf{T} Q \tag{4.6}$$

and thus

$$\mathbf{T}^T \left(-\omega^2 \mathbf{M} + j\omega \mathbf{D} + \mathbf{K}\right) \mathbf{T} Q = F_T. \tag{4.7}$$

The equation of motion is now uncoupled due to the proportionality of the damping. So

$$\left(-\omega^2 \ \mathbf{M}_T \ + j\omega \ \mathbf{D}_T \ + \ \mathbf{K}_T \ \right) Q = F_T, \tag{4.8}$$

where $\mathbf{M}_T$, $\mathbf{K}_T$ and $\mathbf{D}_T$ are diagonal matrices defined by $\mathbf{T}^T\mathbf{M}\mathbf{T}$, $\mathbf{T}^T\mathbf{K}\mathbf{T}$ and $\mathbf{T}^T\mathbf{D}\mathbf{T}$, respectively. We introduce m_i, k_i and d_i representing the mass parameters $m_1, ..., m_n$ as diagonal elements of $\mathbf{M}_T$, stiffness parameters $k_1, ..., k_n$ as diagonal elements of $\mathbf{K}_T$ and damping parameters $d_1, ..., d_n$ as diagonal elements of $\mathbf{D}_T$, respectively.

We define

$$a_i = -\omega^2 m_i + j\omega d_i + k_i, \qquad i = 1, ..., n, \tag{4.9}$$

By applying proportional damping $d_i = 2\xi_i \omega_{0i} m_i$, where ξ_i is the dimensionless damping factors $\xi_1, ..., \xi_n$ and $\omega_{0i}^2 = k_i/m_i$, (4.9) yields

$$a_i = \left(-\omega^2 + j\omega \left(2\xi_i \omega_{0i}\right) + \omega_{0i}^2\right) m_i, \qquad i = 1, ..., n. \tag{4.10}$$

Then, (4.11) can be written as

$$\mathbf{A} Q = F_T, \tag{4.11}$$

where $\mathbf{A}$ is the diagonal matrix with $\{a_i\}$ on the diagonal. Now,

$$Q = \mathbf{A}^{-1} F_T \tag{4.12}$$

and finally the actual displacement response $U = \mathbf{T}Q$ is calculated with

$$U = \mathbf{T}\mathbf{A}^{-1}\mathbf{T}^T F. \tag{4.13}$$

With $H^A = \mathbf{T}\mathbf{A}^{-1}\mathbf{T}^T$, the substructure A representing the end-mill is now fully identified for the use in the coupling equation (4.3). Now, substructure A can be used to represent various end-mills participating in the large numbers of tool-toolholder-spindle combinations.

However, we still need to identify the dynamics of substructure B, i.e. the HSM machine, before we can use the coupling equation (4.3).

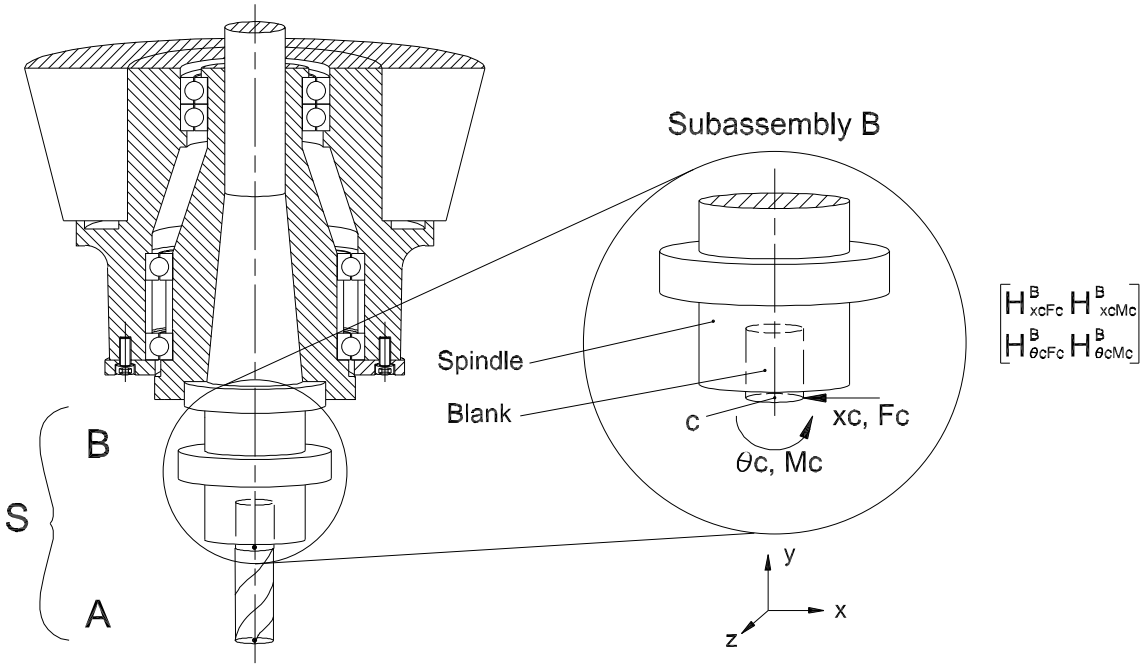

Figure 4.5: The required rotational and translational FRFs of substructure B (the HSM machine).

4.4 Identification of substructure B

The input and output locations of the translational and rotational FRFs that are necessary for the RC technique are displayed in Figure 4.5, where the input and output of the individual rotational and translational FRFs are presented with arrows and the corresponding symmetric FRF-matrix is depicted on the right side of the figure. The identification of the individual FRFs in the FRF-matrix will now be presented.

The FRF $H^B_{x_cF_c}$ of substructure B can be measured with hammer experiments. This is done by inserting the toolholder with a short blank representing the upper part of the end-mill from the cross-section to the end of the shaft of the end-mill. The exact dimensions of this blank can be found in Appendix E. For the acceleration measurement needed to identify $H^B_{x_cF_c}$, a Kistler accelerometer (Model 8696) is used. This sensor can measure both translational and rotational accelerations, however, the angular acceleration can be too small to measure accurately. In contrast to the small angular accelerations, the translational accelerations are of such size that they can be measured accurately, resulting in an accurate measurement of the corresponding translational FRF, provided that the input force can be accurately measured as well. The measurement of this translational FRF $H^B_{x_cF_c}$ is performed as displayed in Figure 4.6. In this figure, the location of the input F_c as well as the location of the outputs θ_c and x_c are indicated with an arrow.

The possibilities for measuring the rotational FRFs $H^B_{\theta_cM_c}$ and $H^B_{\theta_cF_c}$ or $H^B_{x_cM_c}$ are limited but we can not confine ourselves to the measured translational FRF for reasons explained in Section 4.2. The measurements involved in the identification of $H^B_{x_cF_c}$ with the Kistler accelerometer (Model 8696) showed that rotational accelerations on the cross-section of the HSM machine are too small to be measured accurately. The direct experimental measurement of the rotational FRFs $H^B_{\theta_cM_c}$, $H^B_{x_cM_c}$ or $H^B_{\theta_cF_c}$ of the spindle of the HSM machine (substructure B) is therefore not an option. With other techniques, such as FE calculations or analytic

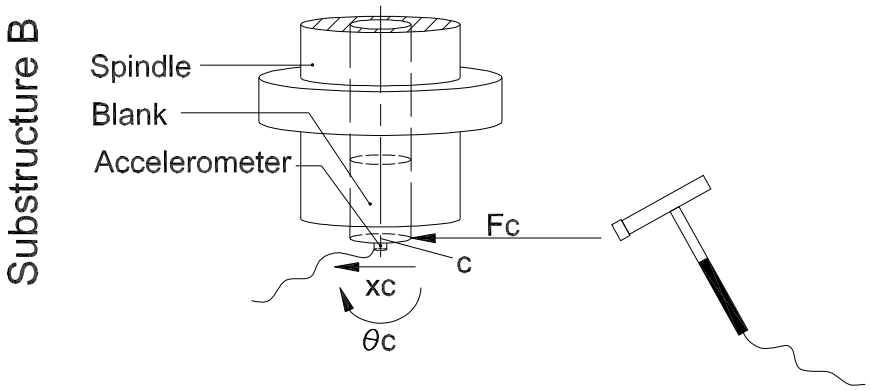

Figure 4.6: Measurement of $H^B_{x_cF_c}$.

models, it takes a lot of effort to determine these FRFs accurately. Doing so for all the tool-toolholder-spindle-system combinations is not efficient. Therefore, in this work, an alternative method based upon the RC coupling technique is developed, in which rotational receptances of substructure B are estimated without the need of applying a moment excitation.

4.4.1 IRC calculation of $H^B_{\theta_cF_c}$ and $H^B_{\theta_cM_c}$

It is preferred that the FRFs of substructure B, the HSM machine, are measured in practice. In this way, the real dynamics, including all stiffness and damping characteristics, are measured accurately.

Silva et al. [67, 68] proposed a method, the inverse RC technique, in which rotational receptances are estimated without having to measure them directly. It is also shown that neither a moment exciter nor an eccentric force applied to a rigid fixture are needed in the estimation of rotational receptances. This technique is studied and applied on the coupling equation derived for the joint HSM machine models for all possible combinations of tools, toolholders and spindles. Therefore, it is desired to use this method that can determine these FRFs based on measurements, including stiffness and damping characteristics. The stiffness and damping characteristics are calculated from measurements performed on locations where measurements can be performed reliably and accurately.

The methodology presented by Silva et al. estimates rotational receptances for one rotational FRF under evaluation. In our case, we have more than one rotational FRF to evaluate. By using symmetry, i.e. $H^B_{x_cM_c} = H^B_{\theta_cF_c}$, there is one rotational FRF less to determine. Now, we have two unknown receptances namely, $H^B_{\theta_cM_c}$ and $H^B_{x_cM_c}$ (or $H^B_{\theta_cF_c}$). Therefore, in this thesis the equation used by Silva et al. is extended to a set of two equations with two unknowns. Hereto, it is necessary to derive a second coupling equation. This is done by introducing the second force F_2 as input in the coupling equation (3.10). The derivation of the second coupling equation is the same as the derivation of the original coupling equation (3.10). Recapitulating the substitution of (3.7) into (3.8); which yields (3.9)

$$\begin{aligned} x_1 = \quad & \left(H^A_{x_iF_i} - H^A_{x_iF_c}\left(H^A_{x_cF_c} + H^B_{x_cF_c}\right)^{-1} H^A_{x_cF_i}\right) F_1 + \\ & \left(H^A_{x_iF_c} - H^A_{x_iF_c}\left(H^A_{x_cF_c} + H^B_{x_cF_c}\right)^{-1} H^A_{x_cF_c}\right) F_2, \end{aligned}$$

where we obtained an expression of x_1 as a function of the two applied forces F_1 and F_2. Now, by assuming the external force F_1 to equal zero, the derivation leads to:

$$\frac{x_1}{F_2} = H^S_{x_iF_c} = H^A_{x_iF_c} - H^A_{x_iF_c}(H^A_{x_cF_c} + H^B_{x_cF_c})^{-1}H^A_{x_cF_c}. \tag{4.14}$$

Similar to the derivation of the original coupling equation, the corresponding RDOFs need to be inserted into this second coupling equation, which leads to

$$\mathbf{H}_{ic}^{S} = \begin{bmatrix} H_{x_iF_c}^{A} & H_{x_iM_c}^{A} \\ H_{\theta_iF_c}^{A} & H_{\theta_iM_c}^{A} \end{bmatrix} - \begin{bmatrix} H_{x_iF_c}^{A} & H_{x_iM_c}^{A} \\ H_{\theta_iF_c}^{A} & H_{\theta_iM_c}^{A} \end{bmatrix} \tag{4.15}$$

$$\left(\begin{bmatrix} H_{x_cF_c}^{A} & H_{x_cM_c}^{A} \\ H_{\theta_cF_c}^{A} & H_{\theta_cM_c}^{A} \end{bmatrix} + \begin{bmatrix} H_{x_cF_c}^{B} & H_{x_cM_c}^{B} \\ H_{\theta_cF_c}^{B} & H_{\theta_cM_c}^{B} \end{bmatrix} \right)^{-1} \begin{bmatrix} H_{x_cF_c}^{A} & H_{x_cM_c}^{A} \\ H_{\theta_cF_c}^{A} & H_{\theta_cM_c}^{A} \end{bmatrix}.$$

By using the simplified representation of the kernel matrix (4.2) while writing out the (1,1) element of $\mathbf{H}_{ic}^{S}$ representing $H_{x_iF_c}^{S}$, $H_{x_iF_c}^{S}$ can be expressed as

$$H_{x_iF_c}^{S} = \frac{x_1}{F_2} = H_{x_iF_c}^{A} + \frac{1}{H_{2,\theta_cF_c}H_{2,x_cM_c} - H_{2,\theta_cM_c}H_{2,x_cF_c}}$$

$$(H_{x_iF_c}^{A}H_{2,\theta_cM_c} - H_{x_iM_c}^{A}H_{2,\theta_cF_c})H_{\theta_cF_c}^{A} + (H_{x_iM_c}^{A}H_{2,x_cF_c} - H_{x_iF_c}^{A}H_{2,x_cM_c})H_{x_cF_c}^{A}. \tag{4.16}$$

The two coupling equations (4.3) and (4.16) can be rewritten in the following form

$$z = a + \frac{g(ec - fb) + h(fd - eb)}{b^2 - cd},$$

$$y = e + \frac{i(ec - fb) + j(fd - eb)}{b^2 - cd}, \tag{4.17}$$

where the meaning of the symbols are presented in Table 4.1 for a more abbreviated notation. We consider the two sums of rotational FRFs b and c to be unknowns in (4.17). These two

$H_{x_iF_i}^{A} = a$	$H_{2,x_cM_c} = H_{2,\theta_cF_c} = b$	$H_{2,\theta_cM_c} = c$	$H_{2,x_cF_c} = d$
$H_{x_iF_c}^{A} = e$	$H_{x_iM_c}^{A} = f$	$H_{x_cF_i}^{A} = g$	$H_{\theta_cF_i}^{A} = h$
$H_{x_cF_c}^{A} = i$	$H_{\theta_cF_c}^{A} = j$	$H_{x_iF_i}^{S} = z$	$H_{x_iF_c}^{S} = y$

Table 4.1: Meaning of the symbols used in the two coupling equations.

unknowns can be written explicitly according to the IRC method presented in Section 3.4. Then, (4.17) is solved with respect to b and c with the aid of the mathematical program Maple, resulting in:

$$b = \frac{-ehd + ehi - egj + hdy + adj - zdj}{-eg + gy - zi + ai}, \tag{4.18}$$

$$c = \frac{1}{(-eg + gy - zi + ai)^2}(e^2h^2d + h^2dy^2 + j^2z^2d +$$
$$j^2a^2d + jfeg^2 - e^2h^2i + fi^2ha - 2eyh^2d - fi^2hz - j^2ega -$$
$$2j^2adz + j^2egz + 2yhadj - 2yhzdj + 2ehzdj - 2ehadj - feghi +$$
$$fyghi - jehiz - jeghy + jehia - jfiga + jfigz + eh^2iy + je^2gh - jfyg^2). \tag{4.19}$$

With the FE calculations of the rotational FRFs $H_{\theta_cM_c}^{A}$ and $H_{\theta_cF_c}^{A}$ of substructure A, the two rotational FRFs concerning substructure B, $H_{\theta_cM_c}^{B}$ and $H_{\theta_cF_c}^{B}$ can now be obtained by:

$$H_{\theta_cM_c}^{B} = c - H_{\theta_cM_c}^{A},$$

$$H_{\theta_cF_c}^{B} = b - H_{\theta_cF_c}^{A}. \tag{4.20}$$

These FRFs can be stored in a data-base as constant properties for the different toolholder-spindle combinations.

These IRC calculations are tested on the 6-DOF mass-spring-damper model in Appendix F. The resulting error in the prediction of the rotational FRFs $H^B_{\theta_c M_c}$ and $H^B_{\theta_c F_c}$ through (4.18), (4.19) and (4.20) is very small, from which we can conclude that the IRC technique to determine the two FRFs $H^B_{\theta_c M_c}$ and $H^B_{x_c M_c} = H^B_{\theta_c F_c}$ is exact.

This IRC technique can therefore be applied on the tool-toolholder-spindle-system combination.

4.4.2 IRC calculation on the HSM machine

To implement the derived IRC technique on the HSM machine to calculate $H^B_{\theta_c F_c} = H^B_{x_c M_c}$ and $H^B_{\theta_c M_c}$, the following strategy is used:

The total assembly S is replaced by an assembly S^*. S^* exist of substructures B and A^* such that $S^* = B + A^*$, see Figure 4.7. Throughout this thesis the superscript * will be used to indicate the involvement in the replacement of the substructure A with A^*. The substructure A^* is a simple cylinder made from the same material as the end-mill. All FRFs of A^* are known by FE calculations. This is a simplification (from a real end-mill to a cylinder) to perform calculations and measurements more easily and as accurately as possible. It is important to note that this does not have any consequence for the fact that exactly the same FRFs $H^B_{\theta_c F_c}$ and $H^B_{\theta_c M_c}$ can be obtained in this way (as opposed to using the end-mill). The exact dimensions of this cylinder used can be found in Appendix E. The position indicated by c is the coupling surface and i indicates the end point of the end-mill that we want to evaluate. By performing hammer experiments on the assembled structure S^* on the HSM machine at the tip (indicated with i), see Figure 4.8, the left-hand side $H^{S^*}_{x_i F_i}$ of the first coupling equation (3.10) is measured. Now with the IRC technique, presented in Subsection 4.4.1, b^*, representing $H^{S^*}_{\theta_c F_c}$, can be computed with (4.18) by substituting the FRFs of substructure A by those concerning A^*. Finally, the rotational FRF $H^B_{\theta_c F_c}$ can be calculated with

$$H^B_{\theta_c F_c} = b^* - H^{A^*}_{\theta_c F_c}. \tag{4.21}$$

However, for the calculation of b^* the measurement of $H^{S*}_{x_i F_c}$ is needed. By performing hammer experiments on the coupling section of the assembly S^* at the location indicated with c, see Figure 4.8, the FRF $H^{S^*}_{x_i F_c}$ of the second coupling equation (4.19) is measured. Since both $H^{S^*}_{x_i F_i}$ and $H^{S^*}_{x_i F_c}$ are now available, the set of two equations, (4.18) and (4.19), can be solved. The calculation of c^*, representing $H^{S^*}_{\theta_c M_c}$, can be done with (4.19), by again substituting the FRFs of substructure A by those concerning A^*. Finally the rotational FRF $H^B_{\theta_c M_c}$ can be calculated with

$$H^B_{\theta_c M_c} = c^* - H^{A^*}_{\theta_c M_c}. \tag{4.22}$$

The substructure B is now fully identified for the use of the coupling equation (4.3), in which substructure A can be used for various end-mills to predict the dynamics of the total system S consisting of all possible tool-toolholder-spindle combinations.

4.5 Discussion

The coupling equation (3.10) is extended with rotational FRFs to calculate the dynamics of the joint models for every tool-toolholder-spindle combination. It is preferred that the rotational and translational FRFs used in the extended coupling equation (4.3) are measured in practice. In this way, the real dynamics, including all stiffness and damping characteristics, are measured accurately.

The substructures A and B representing the end-mill and toolholder-spindle combination, respectively, each form a component of the total joint structure S.

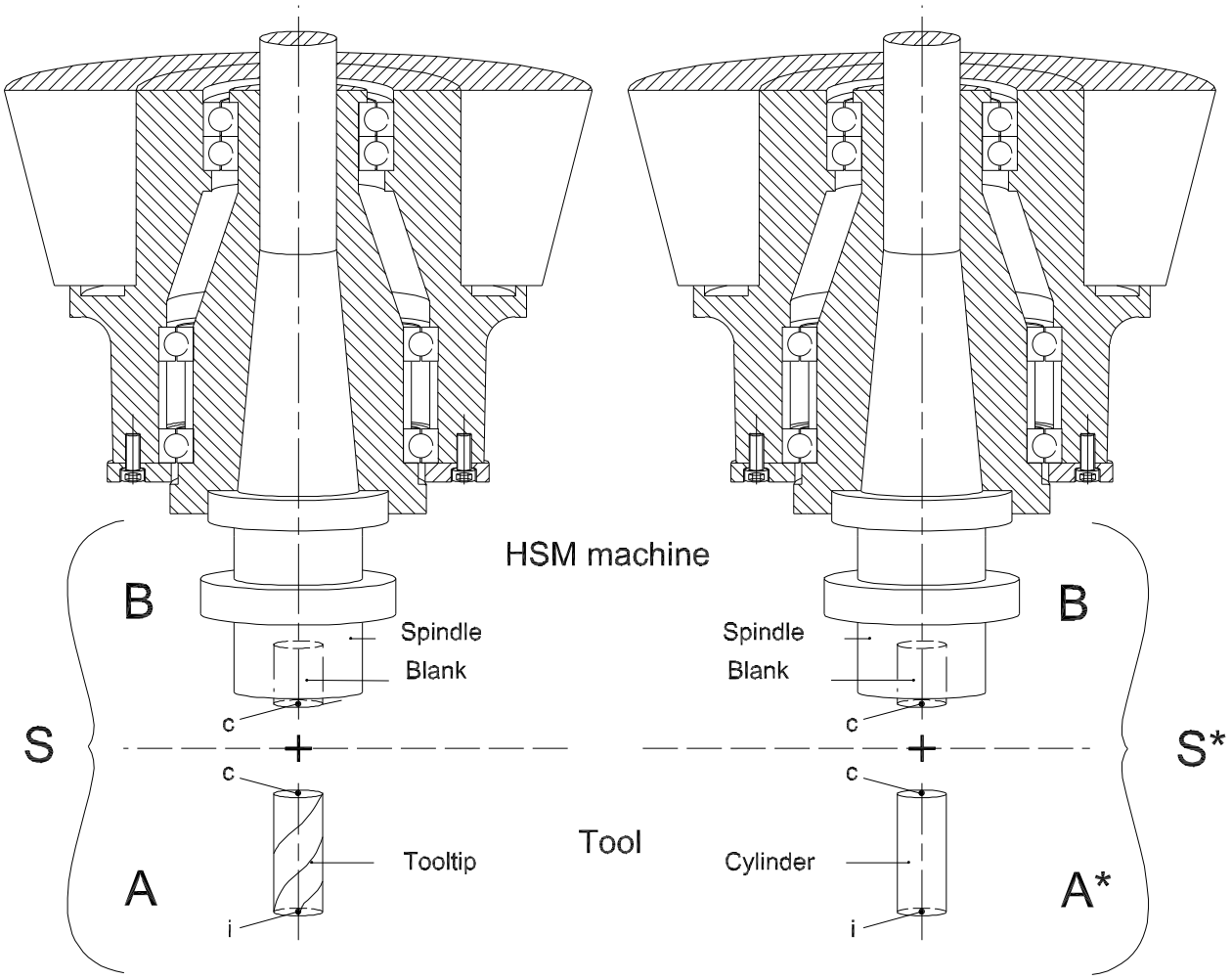

Figure 4.7: Substructures A, A^* and B and assembled systems S and S^*.

Six (rotational) FRFs of substructure A do not need to be calculated by using symmetry. The remaining rotational and translational FRFs of substructure A (the end-mill) are identified as follows. The 3-D tool geometry of the end-mill is obtained from the mill designer. After adjusting the model of the end-mill in UniGraphics, the model is opened in Ansys. Further calculations of the necessary FRFs for the coupling equation are performed in Matlab after exporting the mass and stiffness matrices based on the FE calculations to Matlab. A proportional damping model is employed since the damping level (only due to material damping) is expected to be rather low. In Matlab the equations of motion are uncoupled due to the proportionality of the damping. For the further calculation of the FRFs the number of modes are reduced to the first fourteen (sorted in ascending order of the related eigenfrequencies). This makes the calculations more easily and as accurately as possible.

The FRFs of substructure B are identified as follows: the translational FRF $H^B_{x_cF_c}$ is measured experimentally. The remaining FRFs of substructure B, $H^B_{\theta_cF_c} = H^B_{x_cM_c}$ and $H^B_{\theta_cM_c}$, are both calculated with the IRC technique based on the work of Silva et al. as follows: a second coupling equation is derived. With these two coupling equations, the two measurement locations are moved to the tip of the tool and to the cross-section where accurate measurements on translational FRFs can be performed. All FRFs used in the IRC technique are now available, therefore, $H^B_{x_cM_c}$ and $H^B_{\theta_cM_c}$ can be calculated by replacing the total assembly S by an assembly S^*. S^* exist of substructures B and A^* such that $S^* = B + A^*$,where

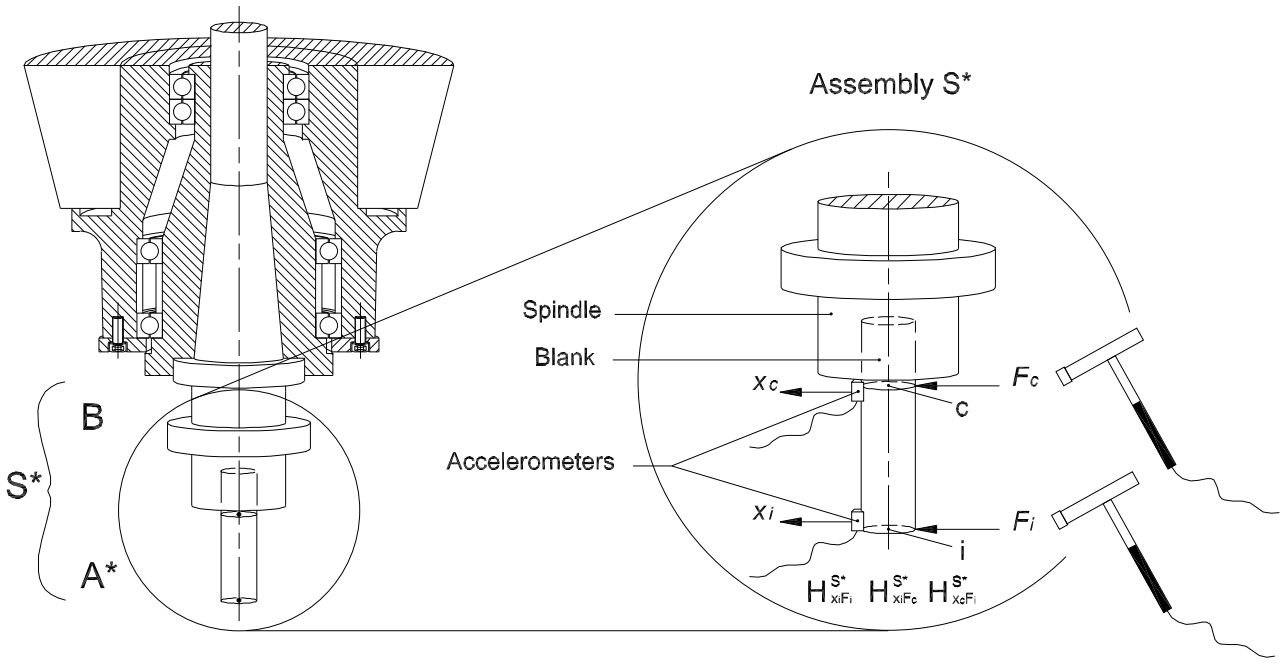

Figure 4.8: Measurement of $H^{S^*}_{x_i F_i}$ and $H^{S^*}_{x_i F_c}$.

substructure A^* is a simple cylinder made from the same material as the end-mill of which all FRFs are known by the calculation routine with UniGraphics, Ansys and Matlab. This is a simplification to perform calculations and measurements more easily and as accurately as possible.

In the next chapter, the IRC and RC strategy is tested in practice on a specific tool-toolholder-spindle combination available at TNO Science and Industry. Hereby, the implementation of the IRC and RC technique on the HSM machine used in the Chattercontrol project is obtained and validations with conventional hammer experiments are performed.

Chapter 5

Experiments

The IRC and RC procedure explained in the previous chapter will be validated experimentally. This validation is performed on a Mikron HSM 700 machine. This milling machine is equipped with a shrink fit tool holder and an end-mill replacement. The end-mill replacement is used because no software data on an existing end-mill was available at the time for the project. The replacement of the end-mill is a cylinder with two flat sides on the tip. The exact dimensions of this cylinder with two flat sides used can be found in Appendix E. The Mikron HSM 700 machine is depicted in Figure 5.1, where the tool, toolholder and spindle are indicated.

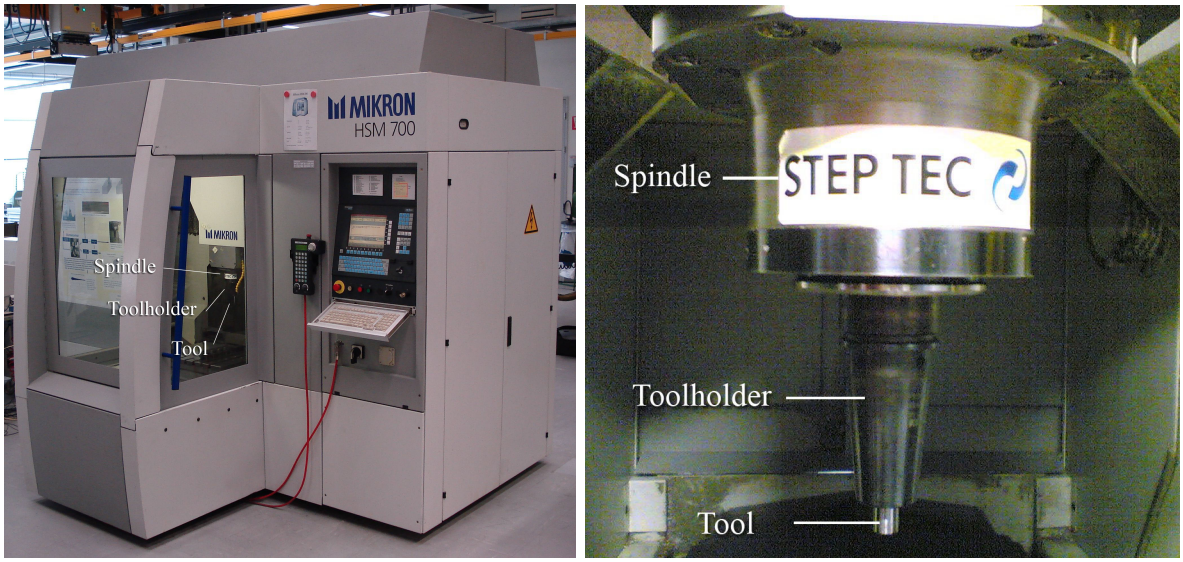

Figure 5.1: The HSM 700 machine.

The FRFs necessary for the RC and IRC calculation are determined by performing hammer experiments. The technical data of the hammer and acceleration sensors used can be found in Table 5.1. The measurements are performed with the parameters presented in Table

type	sensitivity	range	eigenfrequency
sensor SN C194546	2.51 mV/g	1000 g	125 kHz
sensor SN C142403	2.37 mV/g	1000 g	125 kHz
hammer SN 13496	1.17 mV/N	–	–

Table 5.1: Technical data of the measurement equipment.

parameter	value
sampling rate	30000 Hz
measurement time	0.25 s
trigger delay	0.125 s
low-pass filter	10000 Hz

Table 5.2: Technical data of the measurement equipment.

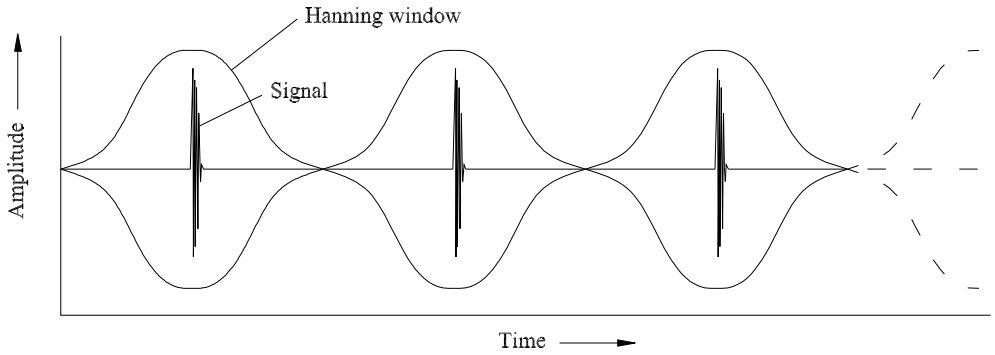

Figure 5.2: Measurement signal.

5.2. The chosen frequency range of interest is from 0 to 10000 Hz. Therefore, the sampling rate is chosen at 30000 Hz according to the Nyquist-Shannon theorem [13], i.e. the highest observable frequency is 15000 Hz. To avoid the possibility of aliasing a low-pass filter is used at 10000 Hz. The stored input and response data is analyzed using Fourier transformations. The trigger delay is set at half the measurement time to assure that the input and response are located in the middle of the time frame of the used window, see Figure 5.2. Hereby, the signal distribution in the applied Hanning window is optimal. The FRFs are averaged using a total of at least ten individual measurements.

For the measurement of the translational FRF $H^B_{x_c F_c}$ a blank with a total length of 50 mm and a diameter of 10 mm is inserted in the toolholder-spindle combination. This blank used can be found in Appendix E. The short blank extends from the toolholder with a free length of 11.75 mm, see Figure 5.3. Hereby, the location of the cross-section is defined by the

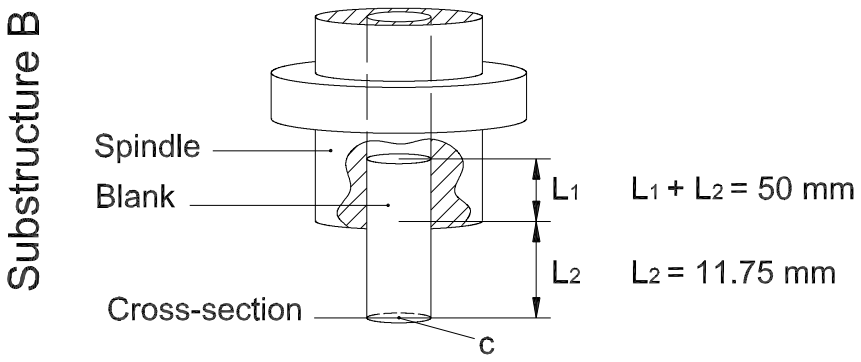

Figure 5.3: Short blank inserted in the toolholder.

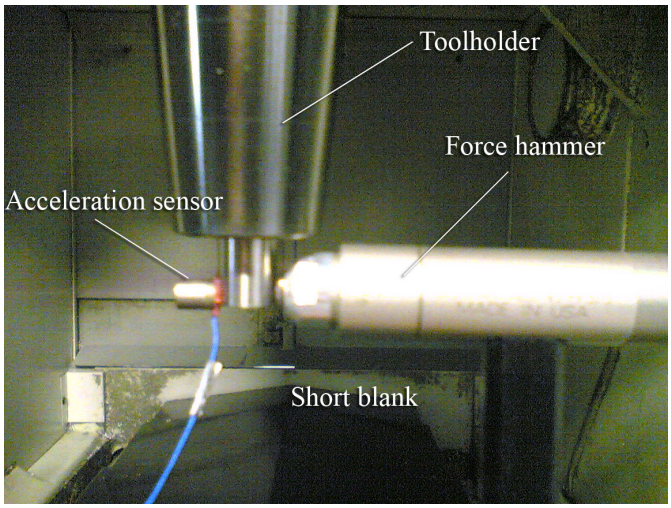

Figure 5.4: Measurement of the translational FRF $H^B_{x_cF_c}$.

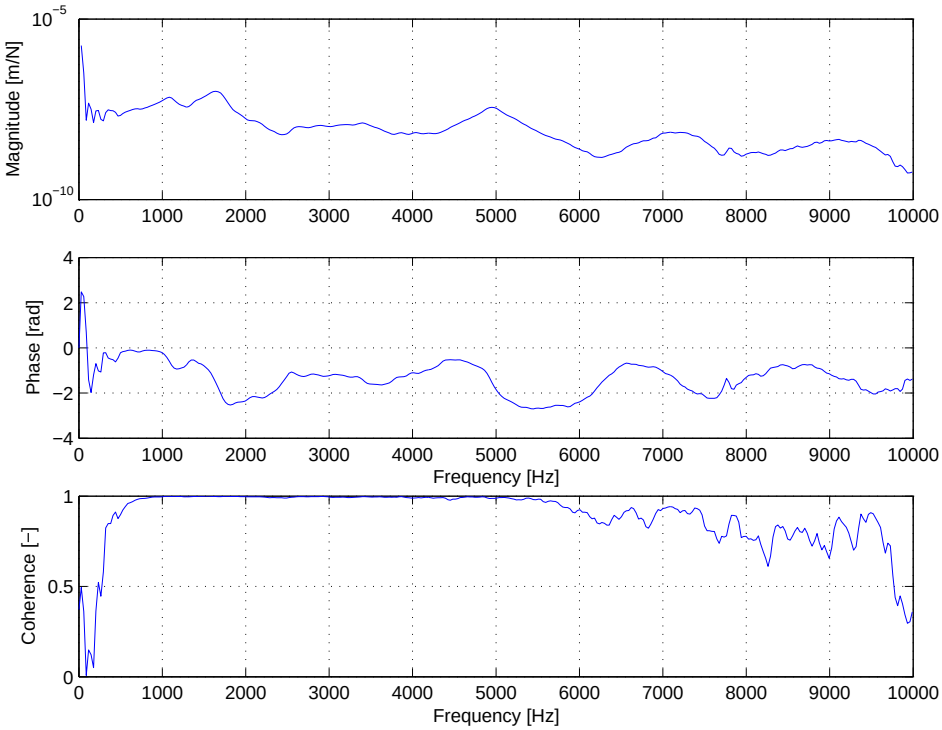

Figure 5.5: Measurement results of $H^B_{x_cF_c}$.

free length of 11.75 mm. It is important that this location of the cross-section is the same for all the measurements performed on the different blanks. A detailed picture of the experiment to determine $H^B_{x_cF_c}$ is presented in Figure 5.4 where the acceleration sensor is located at the tip of the short blank, around 11.75 mm from the tip of the toolholder. The impact location of the hammer is on the opposite side of this cylinder.

The results of the measurements of $H^B_{x_cF_c}$ are presented in Figure 5.5, where the top figure depicts the magnitude of the translational FRF $H^B_{x_cF_c}$; the phase of $H^B_{x_cF_c}$ is plotted in the figure below this. The plot at the bottom depicts the coherence function of the averaged FRFs. From the coherence function, it can be concluded that the FRF of $H^B_{x_cF_c}$ is reliable in the frequency range from 350 to 7500 Hz; above 7500 Hz the coherence drops below 0.8. The first 350 Hz are unreliable because of the use of acceleration sensors. These sensors can not

be used to measure the FRF with respect to position at low frequencies.

The measurement of $H^B_{x_cF_c}$ provides the first FRF of substructure B representing the toolholder-spindle combination. Substructure B needs to be fully identified in terms of translational and rotational FRFs for the RC and IRC technique. By making use of symmetry, yielding $H^B_{x_cM_c} = H^B_{\theta_cF_c}$, only two FRFs are still missing, namely $H^B_{\theta_cM_c}$ and $H^B_{x_cM_c}$ (or $H^B_{\theta_cF_c}$). These FRFs are determined with the IRC technique.

5.1 Implementation and validation of the IRC technique

The derived IRC technique presented in Section 4.4 to calculate $H^B_{\theta_cM_c}$ and $H^B_{x_cM_c}$ (or $H^B_{\theta_cF_c}$), is tested in practice on the Mikron HSM 700 machine. Unfortunately, the calculated FRFs $H^B_{\theta_cM_c}$ and $H^B_{x_cM_c}$ or $H^B_{\theta_cF_c}$ can not be validated directly with actual measured FRFs $H^B_{\theta_cM_c}$ and $H^B_{x_cM_c}$ or $H^B_{\theta_cF_c}$ of the HSM 700 machine because these can not be measured in practice by performing hammer experiments. The results of the IRC technique will be discussed and these results will be tested in the scope of the validation of the RC technique.

5.1.1 Implementation of the IRC technique

The IRC calculation of $H^B_{\theta_cM_c}$ and $H^B_{x_cM_c}$ (or $H^B_{\theta_cF_c}$) is performed by the set of the two coupling equations (4.3) and (4.16) that are written explicitly resulting in (4.18), (4.19) and (4.20), see Section 4.4.2. Now, two FRFs need to be measured, namely $H^{S^*}_{x_iF_i}$ and $H^{S^*}_{x_cF_i}$ (or $H^{S^*}_{x_iF_c}$). For this measurement, a long blank with a total length of 80 mm and a diameter of 10 mm is inserted in the toolholder. The total length corresponds with the $L_1 + L_2 = 80$ mm used in Figure 5.3. This cylinder used can be found in Appendix E. This cylinder is inserted in the toolholder with a depth of 38.35 mm (L_1) which is the same as the inserted depth of the short blank resulting in a cross-section location of 11.75 mm from the tip of the toolholder.

$H^{S^*}_{x_iF_i}$ is measured using a setup as depicted in Figure 5.6 where the acceleration sensor is located at the tip of the long blank, 43 mm from the tip of the toolholder. The impact location of the hammer is on the opposite side of the cylinder.

5.1.2 Measurement results of the IRC technique

The measurement results of $H^{S^*}_{x_iF_i}$ are displayed in Figure 5.7, where again the top figure depicts the magnitude of the FRF $H^{S^*}_{x_iF_i}$. The corresponding phase is plotted in the figure below this. The bottom plot depicts the coherence function. From the coherence function, it can be concluded that the coherence is closest to 1 in the frequency range from 350 to 1690 and from 1760 to 10000 Hz. The dip at 1730 Hz is related to the antiresonance in the FRF at 1730 Hz. This measurement is used in the IRC calculation. To perform the IRC calculation, (to calculate $H^B_{\theta_cM_c}$ and $H^B_{x_cM_c}$ or $H^B_{\theta_cF_c}$), the measurement of $H^{S^*}_{x_cF_i}$ or $H^{S^*}_{x_iF_c}$ is needed.

The FRFs $H^{S^*}_{x_cF_i}$ and $H^{S^*}_{x_iF_c}$ are equal according to symmetry. This provides the possibility to perform a validation if both FRFs are available. Therefore, two experiments are performed. In the first experiment, depicted in Figure 5.8, $H^{S^*}_{x_cF_i}$ is measured. The acceleration sensor is located at the proposed cross-section of the long blank, 11.75 mm from the tip of the toolholder. The impact location of the hammer is on the tip of the long blank, 43 mm from the tip of the toolholder. In the second experiment, depicted in Figure 5.9, $H^{S^*}_{x_iF_c}$ is measured. The acceleration sensor is located at the tip of the long blank, 43 mm from the tip of the toolholder. The impact location of the hammer is on the proposed cross-section of the long blank, 11.75 mm from the tip of the toolholder.

The measurement results of $H^{S^*}_{x_iF_c}$ and $H^{S^*}_{x_cF_i}$ are displayed in Figure 5.10 where they are presented in the same way as in Figures 5.5 and 5.7. Onely, two FRFs are plotted in these figures; namely, $H^{S^*}_{x_cF_i}$ and $H^{S^*}_{x_iF_c}$. From the magnitude and the phase plots, it can

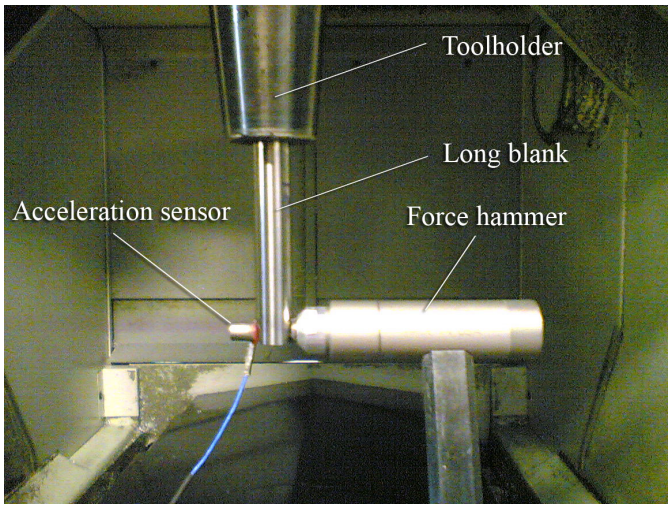

Figure 5.6: Measurement of the translational FRF $H^{S^*}_{x_iF_i}$.

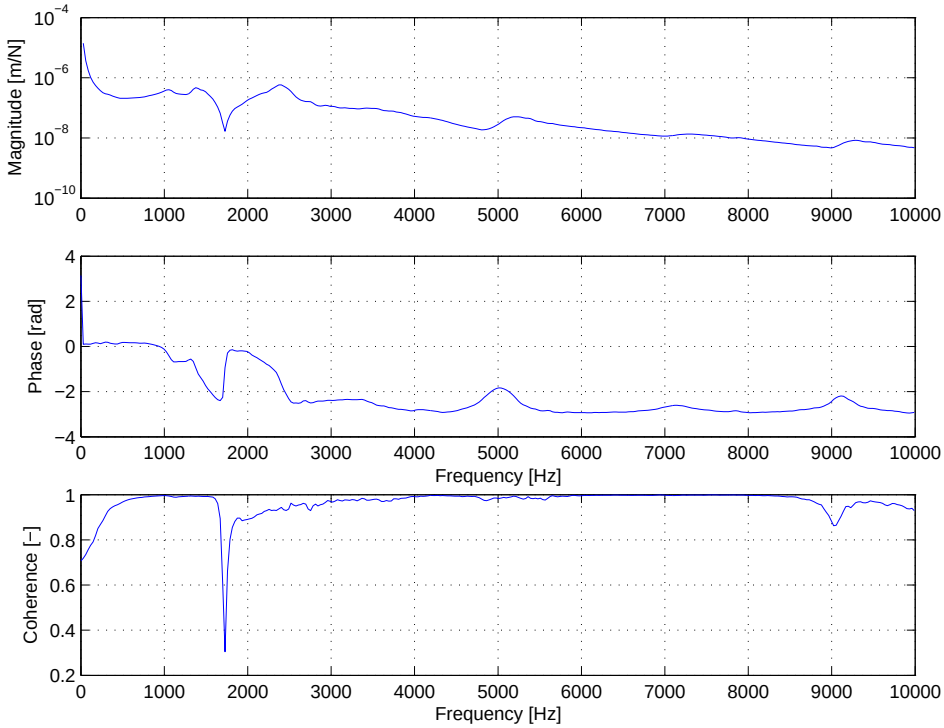

Figure 5.7: Measurement results of $H^{S^*}_{x_iF_i}$.

be concluded that the two FRFs correspond well, hereby reflecting the expected symmetry and, additionally, validating these experiments. From the coherence function at 0 Hz to 7000 Hz, it can be concluded that the coherence of $H^{S^*}_{x_cF_i}$ is higher than the coherence of $H^{S^*}_{x_iF_c}$. The reliable frequency range that is used in the IRC calculations (4.18), (4.19) and (4.20) is determined by the reliability of all the FRFs used in these IRC calculations. The coherence of the earlier performed measurement of $H^{B}_{x_cF_c}$ decreases at 7500 Hz meaning that the decrease in the coherence of $H^{S^*}_{x_cF_i}$ at 7200 Hz is not decreasing the reliable frequency range of the IRC measurement any further. Therefore, $H^{S^*}_{x_cF_i}$ is preferred over $H^{S^*}_{x_iF_c}$ and the reliable frequency range is from 350 to 1690 and from 1760 to 7200 Hz.

In order to perform the IRC calculations, the FRFs of the free-free part of the long blank, (represented by A^*), with the length of 41.70 mm and a diameter of 10 mm are calculated using

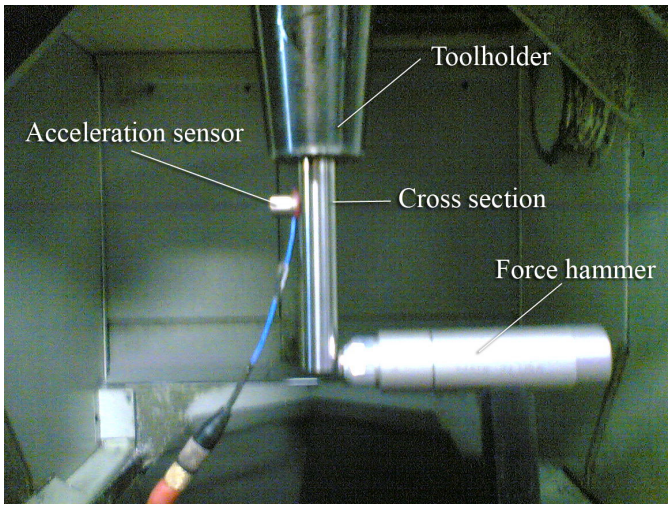

Figure 5.8: Measurement of the translational FRF $H^{S^*}_{x_cF_i}$.

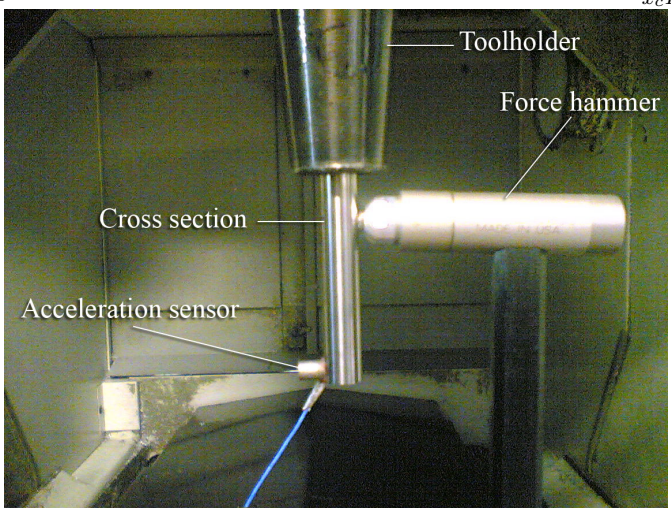

Figure 5.9: Measurement of the translational FRF $H^{S^*}_{x_iF_c}$.

the FE calculation procedure as presented in Section 4.3. The translational and rotational FRFs of A^* are now available.

With the available measurement data of $H^B_{x_cF_c}$, $H^{S^*}_{x_iF_i}$ and $H^{S^*}_{x_cF_i}$ and the FE calculations of the free-free cylinder, the IRC calculation can be performed using (4.18), (4.19) and (4.20). The calculated FRFs $H^B_{\theta_cM_c}$ and $H^B_{\theta_cF_c}$ are presented in Figures 5.11 and 5.12, respectively. By considering the coherence functions of all the measured FRFs $H^B_{x_cF_c}$, $H^{S^*}_{x_cF_i}$ and $H^{S^*}_{x_iF_i}$ necessary for the IRC calculation, the reliable frequency range is from 350 to 1690 Hz and from 1760 to 6200 Hz. This reliable frequency range is illustrated in Figures 5.11 and 5.12 by shading the less reliable frequency ranges. In the reliable frequency range of $H^B_{\theta_cF_c}$, the resonance frequency of the HSM machine is visible at 5000 Hz. This resonance frequency is also visible in the measurement of $H^B_{x_cF_c}$, see Figure 5.5. This implies that the IRC calculated FRFs $H^B_{\theta_cM_c}$ and $H^B_{\theta_cF_c}$, are reliable.

Substructure B representing the toolholder-spindle-HSM 700 machine combination is now fully identified with respect to the translational and rotational FRFs at the proposed cross-section. Now, by calculating the dynamics of any type of end-mill that can be placed in the proposed toolholder-spindle combination, the RC calculation can be used to calculate the dynamics of the joint system.

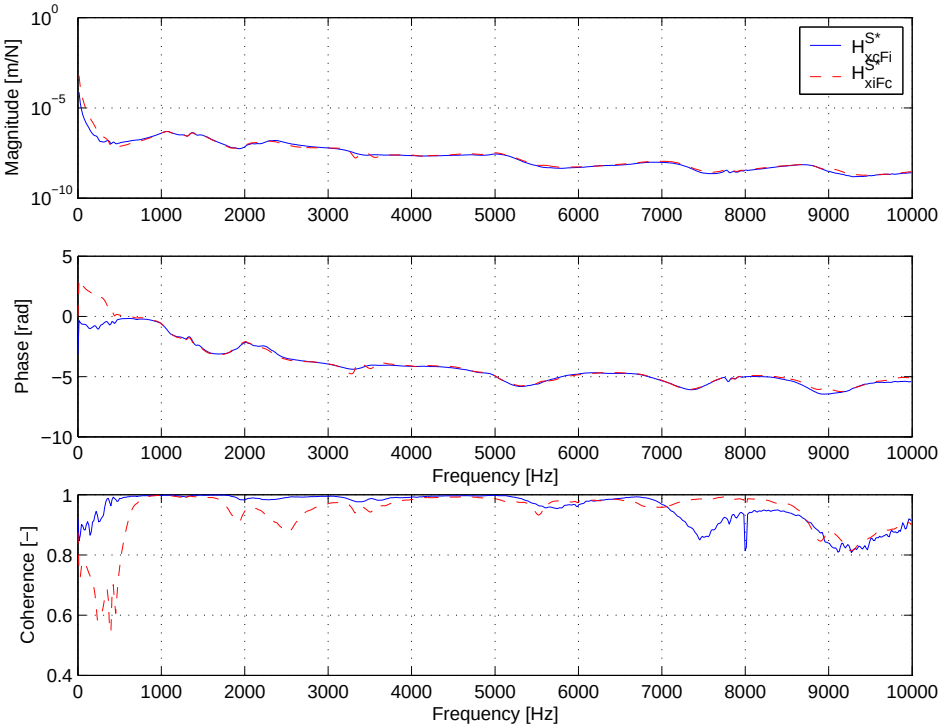

Figure 5.10: Measurement results of $H^{S*}_{x_iF_c}$ and $H^{S*}_{x_cF_i}$.

5.2 Implementation and validation of the RC technique

In order to proceed with the implementation of the RC technique in practice, the cylinder with two flat areas at the tip is used as a replacement of the tool JH421. The cylinder is made from the same carbide material as a modern end-mill. The necessary translational and rotational FRFs of this cylinder with two flat areas are calculated with the calculation routine presented in Section 4.3.

The reliable frequency range that is used in the coupling equation (4.3) is determined by the reliability of all the FRFs used in the RC calculations. The two FRFs $H^B_{\theta_cM_c}$ and $H^B_{\theta_cF_c}$ which are calculated using the IRC technique, are now used in the RC calculation. Therefore, the reliable frequency range of the IRC technique applies to the RC technique as well. The reliable frequency range of the other measured FRF $H^B_{x_cF_c}$ has already been taken into account by the IRC calculation. The reliable frequency range is thereby still stretching from 350 to 1690 Hz and from 1760 to 6200 Hz.

The validation is performed on the tool-toolholder-spindle-system combination. The validation is performed at the tip of the tool where the actual milling forces act on the tool-toolholder-spindle system. The results of both the hammer experiment identifying $H^S_{x_iF_i}$ and the RC calculation $H^S_{x_iF_i}RC_{technique}$ are plotted in Figure 5.13. The reliable frequency range is again illustrated by shading the less reliable frequencies. The upper two plots depict the magnitude and phase, respectively; the two lower plots depict the real and imaginary part of both measured and calculated FRFs. In the last figure, the absolute error between the two FRFs is plotted. If we take in mind the reliable frequency range, it can be concluded that the RC technique provides an accurate prediction of the dynamics of this tool-toolholder-spindle-system combination. The peak in the absolute error at 1700 Hz can be related to the dip in the coherence function of the measurement of $H^{S*}_{x_iF_i}$. Above 6000 Hz, the real and imaginary part of the FRF are almost zero. This is due to the use of hammer experiments. The hammer experiments provide insufficient input energy above this frequency.

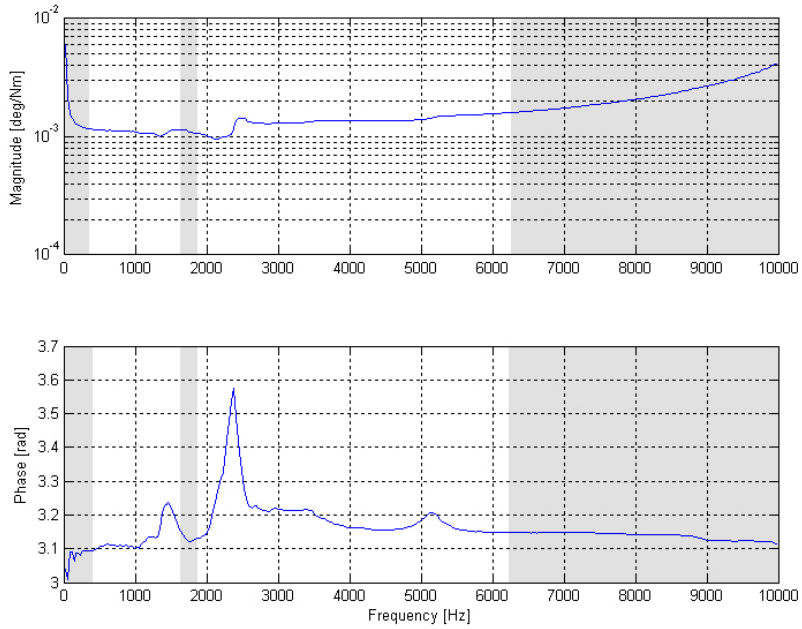

Figure 5.11: $H^B_{\theta_c M_c}$ derived with the IRC technique.

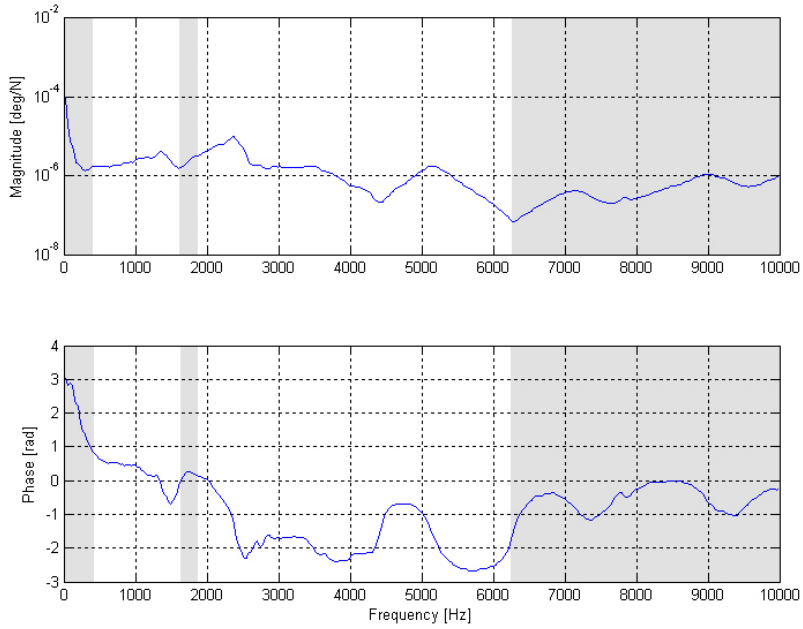

Figure 5.12: $H^B_{\theta_c F_c}$ derived with the IRC technique.

Experimental examples of the IRC and RC technique are discussed so that the working of the methodology is proven experimentally. Conclusions, advantages and limitations of the method are discussed in the next chapter.

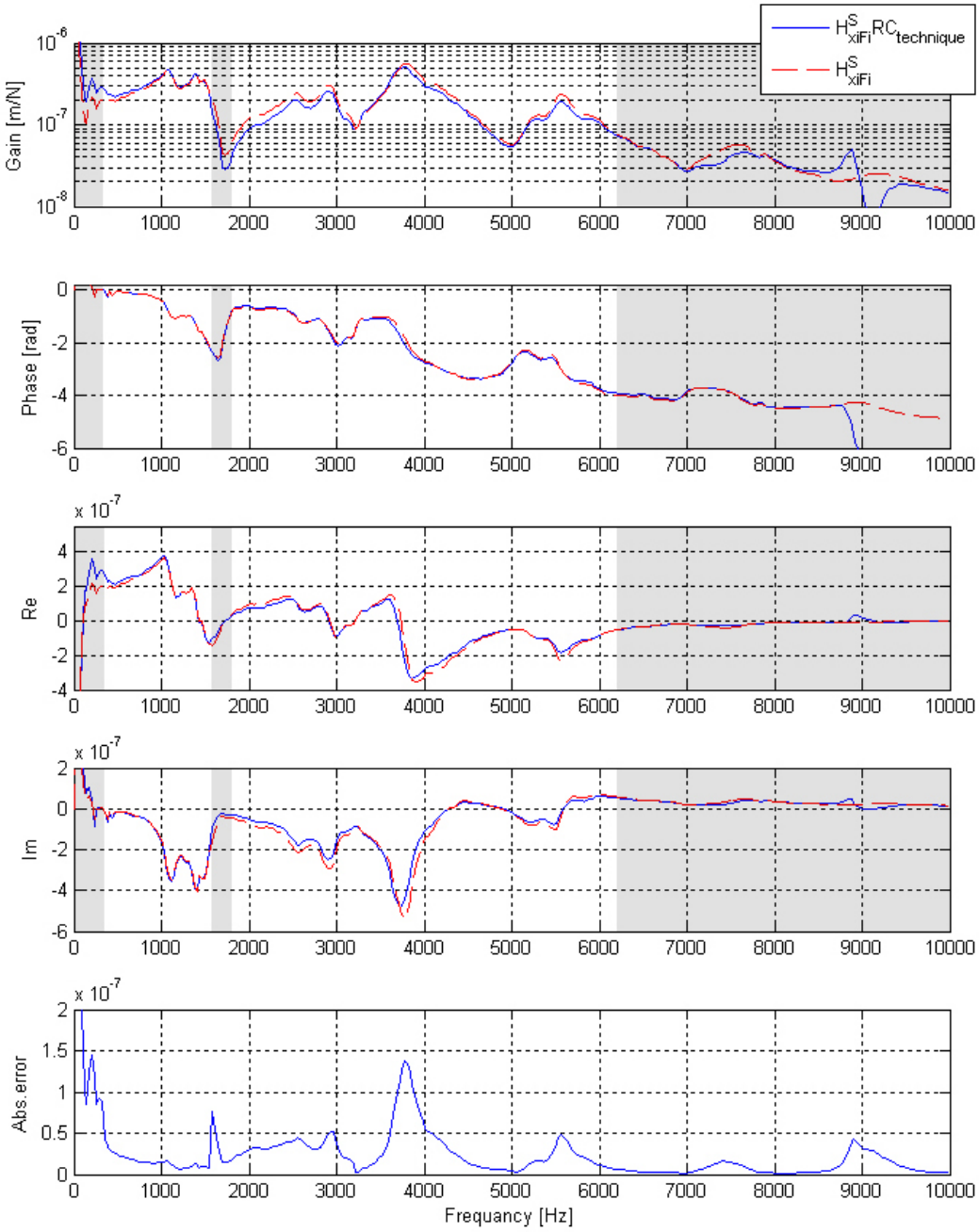

Figure 5.13: RC result $H^S_{x_iF_i}RC_{technique}$ validated experimentally with $H^S_{x_iF_i}$.

Chapter 6

Conclusions and recommendations

In order to predict the occurrence of chatter in the milling process as accurately as possible, the dynamics of the tool-toolholder-spindle-system need to be known. In practice, such knowledge has to be known for a collection of tool-toolholder-spindle combinations. Commonly, the dynamics of a specific tool-toolholder-spindle combination as a whole is determined with impulse hammer experiments. This is a time-consuming process, which has to be repeated for every tool-toolholder-spindle combination.

In this work, we propose an identification approach that potentially increases the efficiency of the identification process compared to that of impulse hammer experiments. This approach involves a separate modelling of, on the one hand the tool dynamics and, on the other hand the toolholder-spindle dynamics. By coupling these models, joint models for every tool-toolholder-spindle combination are available. By integrating the dynamics of the tool-toolholder-spindle-system in the overall milling process model, a 'chatter-free' working-point (i.e. depth of cut and spindle speed) can be calculated. The developed coupling technique is tested in a model based environment. The developed coupling technique is also validated experimentally. This validation shows that using the proposed identification strategy, the dynamics of the tool-toolholder-spindle combination can be predicted accurately.

The following conclusions are drawn and we offer the following recommendations that need attention in future work.

6.1 Conclusions

The end-mills can be modeled in the same way as the successfully modeled end-mill replacement (the cylinder with two flat sides on the tip) by using computer edit designs, FEM calculations and by applying reduction techniques. By performing impulse hammer experiments and applying the proposed IRC calculations, the toolholder-spindle dynamics are successfully identified. These models are successfully coupled with the proposed RC technique. In this way, a joint model of this tool(replacement)-toolholder-spindle combination is available.

By making models of the subsystems, the derived coupling equations is tested in a model based environment. These models shows that the identification procedure is exact. The experimental validation has shown that the accuracy of the experimental models serving as an input for the coupling equation is of great importance for the accuracy of the identification procedure.

Similar to existing coupling methods introduced by Schmitz et al. [58, 59, 61, 65], Park et al. [47] and Esterling [22], the proposed method requires no on-line measurements on the required tool-toolholder-spindle combinations on the HSM machine. This method differs from the existing coupling methods in the sense that no adaptations need to be carried out on the milling machine and no accurate fitting of coupling parameters (for the cross-section stiffness and damping) have to be performed.

The proposed RC coupling methodology can be used in other applications where one of the substructures is exchangeable and can be used as a basis in applications where the use of substructures can support an efficient identification process. The IRC methodology can be used in other applications where one is interested in the dynamic properties corresponding to a specific response location of a system where measurements can not be performed. By measuring assembly dynamics and by identifying the dynamics of the remaining substructures, the structural dynamics between a measurement point and actual location of interest can be compensated.

6.2 Recommendations

The identification method proposed in this thesis is validated with the use of an end-mill replacement. Therefore, the identification method has to be repeated with a real end-mill. From this identification a stability lobe diagram (SLD) can be constructed which can be validated with a experimentally constructed SLD. When such models indeed prove to be predictive, the identification process can be performed to fill a data-base incorporating the dynamics for different toolholders (in combination with specific spindle) and different tools. By coupling the dynamics of the two separate subsystems from the data-base, joint models for every tool-toolholder-spindle combination are available. In the future, the end-mill manufacturer could possibly deliver dynamic models of the specific end-mills as technical data to the client.

Rotational speed dependencies of the spindle dynamics can be included in the model of the HSM machine and are expected to be important for accurate chatter prediction. Esterling et al. [21] and Kiefer [35] developed a non-contact electromagnetic measurement device to capture the machine and tool dynamics with rotational speed dependency. With this device, the substructure representing the milling machine can be measured with rotational speed dependency. Also, gyroscopic effects can be included in the FE models of the end-mills, to establish the possibility to make the working-point calculations spindle speed dependent.

When the tool-toolholder-spindle combinations to be modeled involve a large number of different toolholders, it may be more efficient to use three substructures in the coupling process. The three substructures would then be: the milling machine, the toolholder and the end-mill. In this way, the dynamics of the different toolholders can be calculated using FE models instead of by performing measurements on all toolholder-machine combinations.

Bibliography

[1] J. Agapiou. A Methodology to Measure Joint Stiffness Parameters for Toolholder/Spindel Interfacees. *Transactions of NAMRI/SME*, 32:503–510, 2004.

[2] Y. Altintas. *Manufacturing Automation*. Cambridge University Press, 2000. ISBN 0521659736.

[3] Y. Altintas and E. Budak. Analytical prediction of stability lobes in milling. *Annals of the CIRP*, 44(1):357–362, 1995.

[4] R.F. Baldacci, A. Corsanego, and A. Del Grosso, editors. *Numerical Modelling of Structures to Account for Internal Damping, Damping Effects in Aerospace Structures*, number 277, London, 1979. AGARD Conference Proceedings.

[5] R.M. Bamford. A Modal Combination Program for Dynamic Analysis of Structures. *NASA center: Jet Propulsion Laboratory*, JPL-TM-33-290 Document ID 19670010842, 1967.

[6] W.A. Benfield, C.S. Bodley, and G. Morosow. Modal Synthesis Methods. In *NASA-TM-X-72318*. Marshall Space Flight Center, Space Shuttle Dynamics and Aeroelasticity Working Group Symposium on Substructure Testing and Synthesis, 1972.

[7] R.E.D. Bishop and D.C. Johnson. *The Mechanics of Vibrations*. Cambridge University press, 1960.

[8] T.J. Burns and T.L. Schmitz. A Study of Linear Joint and Tool Models in Spindle-Holder-Tool Receptance Coupling. International Design Engineering Technical Conferences and Computers and Information in Engineering Conference, September 24-28, 2005.

[9] J.A. Cafeo, M.W. Trethewey, and H.J. Sommer. Measurement and Application of Experimental Rotational Degrees of Freedom for Mode Shape Refinement. *International Journal of Analytical and Experimental Modal Analysis*, 7(4):255–269, 1992.

[10] J. Chae, S. Park, and T. Freiheit. Investigation of Micro Cutting. *International Journal of Machine Tools and Manufacture*, 46:313–332, 2006.

[11] C.H. Cheng, T.L. Schmitz, N. Arakere, and G.S. Duncan. An Approach for Micro End Mill Frequency Responce Predictions. Proceedings of American Society of Mechanical Engineers International Mechanical Engineering Congress and Exposition, 2005, Orlando, FL.

[12] The MacNeal-Schwendler Corp. *MSC/NASTRAN reference manual Introduction to Superelements in Dynamic Analysis*. MSC/NASTRAN, Los Angeles, 2004.

[13] J.P. Courriou. *Process Control Theory and Applications*. 2004. ISBN 1852337761.

[14] R.R. Craig. *An Introduction to Computer Methods*. 1981. ISBN 0471044997.

[15] R.R. Craig and M.C.C. Bampton. Coupling of Substructures for Dynamic Analysis. *American Institute of Aeronautics and Astronautics Journal*, 6:1313–1319, 1968.

[16] K. Cuppens, P. Sas, and L. Hermans. Evaluation of the FRF Based Substructuring and Modal Synthesis Technique Applied to Vehicle FE Data. *Journal of Vibration and Acoustics, Transactions of the ASME*, 119:304–310, 1997.

[17] K. Cuppers and L. Hermans. Evaluation of the FRF Based Substructuring and Modal Synthesis Technique Applied to Vehicle FE Data. *Annals of the CIRP*, 53(1):309–312, 2002.

[18] W. DAmbrogio and A. Sestieri. Substructure Coupling using FRFs: Strategies for Tackling Rotational Degrees of Freedom. *International Conference on Structural Dynamics Modelling*, pages 229–238, 2002.

[19] N. Deshpande and M.S. Fofana. Nonlinear regenerative chatter in turning. *Robotics and Computer Integrated Manufacturing*, 17:107–112, 2001.

[20] G.S. Duncan, M. Kurdi, T.L. Schmitz, and J. Snyder. Uncertainty Propagation for Selected Analytical Milling Stability Limit Analyses. *Transactions of North American Manufacturing Research Institution(NAMRI)/Society of Manufacturing Engineers(SME)*, 34: 17–24, 2006.

[21] D. Esterling, F.D. Caulfield, A. Kiefer, G. Buckner, and P. Jaju. Non-contact device for measuring frequency response functions of CNC machine tools. In *Proceedings of IMECE'03*, pages 77–83, Washington, D.C., November 2003. ASME International Mechanical Engineering Congress.

[22] D.M. Esterling. Method for Reducing the Measurement Requirements for the Dynamic Response of Tools in a CNC Machine. Patent Application Publication, January 2005.

[23] D.J. Ewins. *Modal testing: theory, practice and application.* Baldock, 2000.

[24] D.J. Ewins and P.T. Gleeson. Experimental Determination of Multi Directional Mobility Data for Beams. *Shock and Vibration Bulletin*, 45(5):153–173, 1975.

[25] R.P.H. Faassen, N. van de Wouw, J.A.J. Oosterling, and H. Nijmeijer. Prediction of regenerative chatter by modelling and analysis of high-speed milling. *International Journal of Machine Tools and Manufacture*, 43(14):1437–1446, 2003.

[26] R.P.H. Faassen, N. van de Wouw, J.A.J. Oosterling, and H. Nijmeijer. Updated tool path modelling with periodic delay for chatter prediction in milling. In *5th Euromech Nonlinear Dynamics Conference (ENOC)*, Eindhoven, the Netherlands, August 2005. Euromech.

[27] R.P.H. Faassen, N. van de Wouw, J.A.J. Oosterling, and H. Nijmeijer. An Improved Tool Path Model Including Periodic Delay for Chatter Prediction in Milling. *Journal of Computational and Nonlinear Dynamics, Transactions of the ASME*, 2007. accepted.

[28] S. Hou. Review of modal synthesis techniques and a new approach. *Shock and Vibration Bulletin*, 40(4):25–39, 1969.

[29] A.T.M.J.M. Huizinga, D.H. van Campen, and B. de Kraker. Application of Hybrid Frequency Domain Substructuring for Modelling an Automotive Engine Suspension. *Journal of Vibration and Acoustics, Transactions of the ASME*, 119:304–310, July 1997.

[30] W.C. Hurty. Dynamic Analysis of Structural Systems by Component Mode Synthesis. Technical Report 32-530, Jet Propulsion Laboratory, Pasadena, January 1964.

[31] W.C. Hurty. Dynamic Analysis of Structural Systems Using Component Modes. *American Institute of Aeronautics and Astronautics Journal*, 3:678–685, 1965.

[32] J. Hutchinson. Shear Coefficients for Timoshenko Beam Theory. *Journal of Applied Mechanics*, 68:87–92, 2001.

[33] M. Imregun, D.A. Robb, and D.J. Ewins. Structural modification and coupling dynamic analysis using measured FRF data. Proceedings of the 5th International Modal Analysis Conference, 1987.

[34] ANSYS Inc. Theory Reference. www.ansys.com/services/documentation.

[35] A.J. Kiefer. Integrating electromechanical actuator hardware with receptance coupling substructure analysis for chatter prediction on high speed machining centers. Master's thesis, North Carolina State University, Raleigh, NC, 2004.

[36] E.B. Kivanc and E. Budak. Structural Modeling of End Mills for Form Errors and Stability Analysis. *International Journal of Machine Tools and Manufacture*, 44(11): 1151–1161, 2004.

[37] B. Kolman and D.R. Hill. *Elementary Linear Algebra*. Rearson Prentice Hall, 8th edition, 2004. ISBN 0131219332.

[38] W. Liu and D. Ewins. The Importance Assessment of RDOF in FRF Coupling Analysis. Technical report, Imperial College Department of Mechanical Engineering, London, 2001.

[39] R.H. MacNeal. A Hybrid Method of Component Mode Synthesis. *Journal of Computers and Control*, 1:581–601, 1971.

[40] B. Mann, K. Young, T.L. Schmitz, M. Bartow, and P. Bayly. Machining Accuracy Due to Tool and Workpiece Vibrations. *Proceedings of ASME International Mechanical Engineering Congress and Exposition*, IMECE2003-41991, 2003.

[41] L. Marc and Y. Altintas. An Improved Time Domain Simulation for Dynamic Milling at Small Radial Immersions. *Journal of Manufacturing Science and Engineering, Transactions of the ASME*, 125(3):416–422, 2003.

[42] D. Montalvao, A.M.R. Ribeiro, N.M.M. Maia, and J.M.M. Silva. Estimation of the Rotational terms of the Dynamic Response Matrix. *Shock and Vibration Bulletin*, 11: 333350, 2004.

[43] D. Montgomery and Y. Altintas. Mechanism of Cutting Force and Surface Generation in Dynamic Milling. *Journal of Engineering for Industry, Transactions of the ASME*, 113:160–168, 1991.

[44] M.R. Movahhedy and J.M. Gerami. Prediction of dynamic response of machine tool by sub-structure analysis. In *Eighth International Conference on Vibrations in Rotating Machinery - IMechE Conference Transactions; IMechE Event Publications*, volume 2, pages 141–151, 2004.

[45] M.R. Movahhedy and J.M. Gerami. Prediction of spindle dynamics in milling by sub-structure coupling. *International Journal of Machine Tools and Manufacture*, 46:243–251, 2006.

[46] N. Olgac and M. Hosek. A New Perspective and Analysis for Regenerative Machine Tool Chatter. *International Journal of Machine Tools and Manufacture*, 38:783–798, 1998.

[47] S. Park. *Identification of spindle integrated force sensor's transfer function for modular end mills.* PhD thesis, Washington D.C., 2003.

[48] S. Park, Y. Altintas, and M. Movahhedy. Receptance Coupling for End Mills. *International Journal of Machine Tools and Manufacture*, 43(9):889–896, July 2003.

[49] J. Peters, P. Vanherck, and H. Van Brussel. *The Measurement of the Dynamic Cutting Coefficient*, volume 129-136. Annals of the CIRP, 1971.

[50] B. Rao and Y.C. Shin. A Comprehensive Dynamic Cutting Force Model for Chatter Prediction in Turning. *International Journal of Machine Tools and Manufacture*, 39 (10):1631–1654, 1999.

[51] Y. Ren and C.F. Beards. On substructure synthesesis with FRF Data. *Journal of Sound and Vibration*, 185(5):845–866, 1995.

[52] A.M.R. Ribeiro. *Development of Dynamic Analysis Technics for Structural Modification.* PhD thesis, Technical University of Lisbon, 1999.

[53] S. Rubin. Improved Component-Mode Representation for Structural Dynamic Analysis. *American Institute of Aeronautics and Astronautics Journal*, 13:995–1006, 1975.

[54] C.J. Salomon. Process for machining metals of similar acting materials when being worked by cutting tools. German Patent Number 523594, 1931.

[55] S. Sattinger. A Method for Experimentally Determining Rotational Mobilities of Structures. *Shock and Vibration Bulletin*, 50:17–27, 1980.

[56] T.L. Schmitz. Improved Sensor Data Utility Through Receptance Coupling Modeling. ASME International Mechanical Engineering Congress, November 13-19 2004.

[57] T.L. Schmitz and T.J. Burns. Receptance Coupling for High-Speed Machining Dynamics Prediction. In *International Modal Analysis Conference*, Kissimmee, FL, February 3-6 2003.

[58] T.L. Schmitz and R. Donaldson. Predicting High Speed Machining Dynamics by Substructure Analysis. *Annals of the CIRP*, 49:303–308, 2000.

[59] T.L. Schmitz and G.S. Duncan. Tree-Component Receptance Coupling Substructure Analysis for Tool Point Dynamics Prediction. *Journal of Manufacturing Science and Engineering, Transactions of the ASME*, 127(4):781–790, 2005.

[60] T.L. Schmitz, M. Davies, K. Medicus, and J. Snyder. Improving High-Speed Machining Material Removal Rates by Rapid Dinamic Analysis. *Annals of the CIRP*, 50(1):263–268, 2001.

[61] T.L. Schmitz, M.A. Davies, and M.D. Kennedy. Tool Point Frequency Response Function Prediction for High Speed Machining by RCSA. 123:700–707, 2001.

[62] T.L. Schmitz, J. Couey, E. Marsh, and M. Tummond. The Role of Cutter Eccentricity on Surface Finish and Milling Forces. *Proceedings of ASME International Mechanical Engineering Congress and Exposition*, IMECE2004-60232, 2004.

[63] T.L. Schmitz, J. Ziegert, T. Burns, B. Dutterer, and W. Winfough. Tool-Length Dependent Stability Surfaces. *Machining Science and Technology*, 8:377–397, 2004.

[64] T.L. Schmitz, J. Ziegert, and C. Stanislaus. A Method for Predicting Chatter Stability for Systems with Speed-Dependent Spindle Dynamics. *Transactions of North American Manufacturing Research Institution(NAMRI)/Society of Manufacturing Engineers(SME)*, 32:17–24, 2004.

[65] T.L. Schmitz, G.S. Duncan, C. Zahner, J. Dyer, and M. Tummond. Improved Milling Capabilities through Dynamics Prediction: Tree Component Spindle-Holder-Tool Model. In *National Science Foundation DMII Grantees Conference*, Scottsdale, AZ, 2005.

[66] H. Schulz and T. Moriwaki. Highspeed machining. *Annals of the CIRP*, 41(2):637–642, 1992.

[67] J.M.M. Silva, N.M.M. Maia, and A.M.R. Ribeiro. Some Applications of Coupling/Uncoupling Techniques in Structural Dynamics. 15th International Modal Analysis Conference, 1997.

[68] J.M.M. Silva, N.M.M. Maia, and A.M.R. Ribeiro. Estimation of Frequency Response Functions Involving RDOFs Using an Uncoupling Technique. International Conference on Applications of Modal Analysis, December 1999.

[69] T.G. Sofrin. The combination of dynamical systems. *Journal of the Aeronautical Sciences*, 13(6):281–288, 1946.

[70] G. Stépán, T. Insperger, P.V. Bayly, and B.P. Mann. Multiple chatter frequencies in milling processes. *Journal of Sound and Vibration*, 262:333–345, 2003.

[71] G. Stépán, R. Szalai, B.M. Mann, P.V. Bayly, T. Insperger, J. Gradisek, and E. Govekar. Nonlinear Dynamics of High-Speed Milling-Analysis, Numerics, and Experiments. *Journal of Vibration and Acoustics, Transactions of the ASME*, 127:197–203, 2005.

[72] A.O. Sykes. Application of admittance and impedance concepts in the synthesis of vibrating systems. *American Society of Mechanical Engineers, Special Publication of the Shock and Vibration Committee*, pages 22–37, 1971.

[73] R. Szalai. *Nonlinear dynamics of high-speed milling*. PhD thesis, University of Technology and Economics, Department of Applied Mechanics, Budapest, February 2006.

[74] R. Szalai, B. Mann, and G. Stépán. Period-two and Quasi-periodic Vibrations of High-speed Milling. In *9th CIRP International Workshop on Modeling of Machine Optimization*, Bled, Slovania, May 2006.

[75] J. Tlusty. Analysis of the State of Research in Cutting Dynamics. *Annals of the CIRP*, (2):583–589, 1978.

[76] J. Tlusty. *Manufacturing processes and equipment*. 1999. ISBN 0-201-49865-0.

[77] J. Tlusty and M. Polacek. *Besipiele der behandlung der selbsterregten Schwingung der Werkzeugmachinen*. Hanser Verlag. FoKoMa, Munchen, 1957.

[78] S.A. Tobias and W. Fiswick. *Theory of regenerative Machine Tool Chatter*. Engineering, London, 1958.

[79] ITI TranscenData Interoperability Solutions for CAD/CAM/CAE/PLM. www.transcendata.com/support/pdelib/step.htm.

[80] J.S. Tsai and Y.F. Chou. The identification of dynamic characteristics of a single bolt joint. *Journal of Sound and Vibration*, 125:487–502, 1988.

[81] University of Trieste, Chalmers University, Imperial College, Bosch, and LMS International. *Use of Rotational Degrees of Freedom in Structural Dynamics Analysis: Guidelines*, 1998 Contract number: BRPR-CT97-540, Project number: BE 97-4184.

[82] A.P.V. Urgueira. *Dynamic analysis of coupled structures using experimental data.* PhD thesis, Imperial College of Science, Technology and Medicine, University of London, 1989.

[83] A.S. Yigit and A.G. Ulsoy. Application of Nonlinear Receptance Coupling to Dynamic Stiffness Evaluation for Reconfigurable Machine Tools. *The University of Michigan*, 2002.

[84] T. Yokoyama. Vibrations of a Hanging Timoshenko Beam Under Gravity. *Journal of Sound and Vibration*, 141:245–258, 1990.

[85] G.P. Zhang, Y.M. Huang, W.H. Shi, and W.P. Fu. Predicting Dynamic Behaviours of a Whole Machine Tool Structure Based on Computer-aided Engineering. *International Journal of Machine Tools and Manufacture*, 43:699–706, 2003.

Appendix A

Influence of measurement noise

The 4DOF mass-spring-damper system used to test the accuracy of the RC and IRC technique, depicted in Figure 3.2, is used to test the influence of measurement noise on the RC and IRC results. To test the influence of measurement noise, the FRFs of both substructure A and B are deliberately contained with noise. This is done as follows,

$$\tilde{H}^{A,B}_{x_{i,c}F_{i,c}} = H^{A,B}_{x_{i,c}F_{i,c}} n\left(\omega\right) \tag{A.1}$$

where $\tilde{H}^{A,B}_{x_{i,c}F_{i,c}}$ represents the FRFs of substructure A and B contained with noise, $H^{A,B}_{x_{i,c}F_{i,c}}$ represents the FRFs of substructure A and B without the influence of measurement noise and $n\left(\omega\right)$ represents the relative disturbance with a mean of 1 and a variance of 10% of the specific FRF over the whole frequency range. The effect of the noise multiplication on the FRFs is visualized by the contained FRF $\tilde{H}^{A}_{x_cF_c}$ as depicted in Figure A.1 where the left

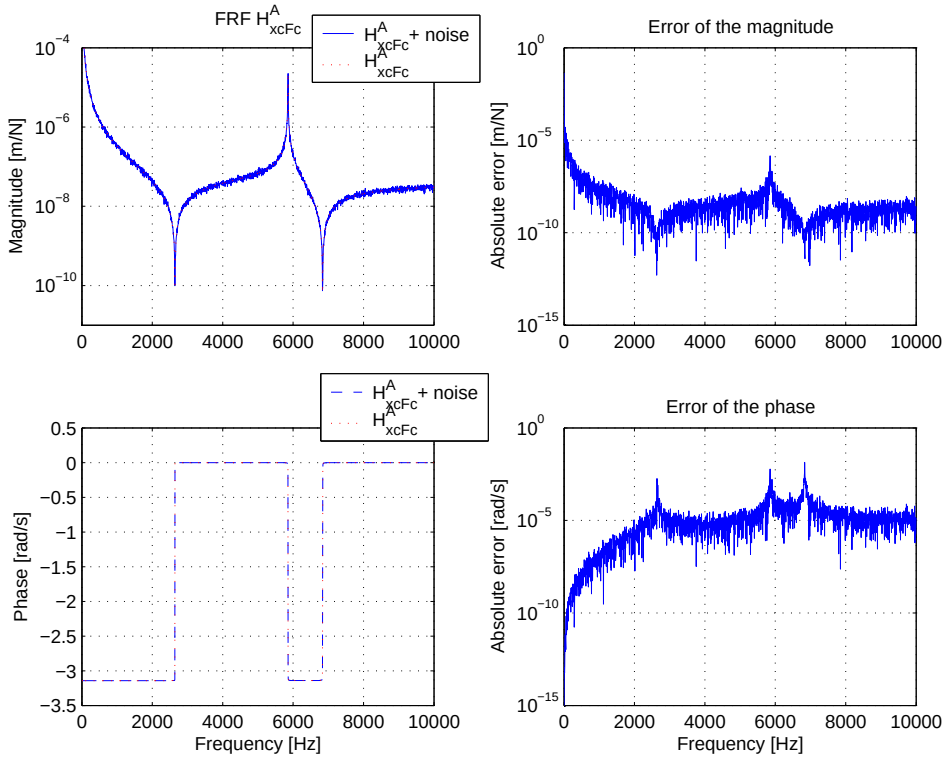

Figure A.1: $\tilde{H}^{A}_{x_cF_c}$ contained with measurement noise.

figures represent, from top to bottom, the magnitude and phase of $H^{A}_{x_cF_c}$. In these figures,

$H^A_{x_cF_c}$ is presented with and without the influence of noise. In the right figures the absolute error is presented with; from top to bottom, the magnitude and the phase error.

By adding noise to the individual FRFs of both substructures, effects of noise on the coupling equation (3.10) are tested. The coupling result of the RC technique, with the influence of measurement noise on all the FRFs of both substructures, is displayed in Figure A.2. The

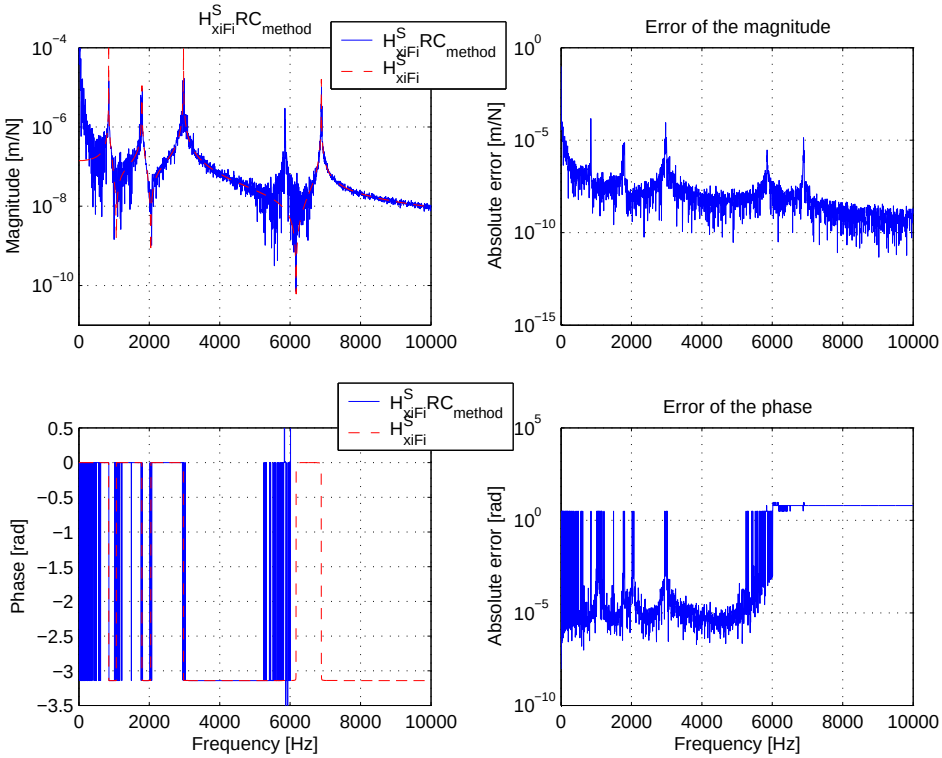

Figure A.2: $H^S_{x_iF_i}$ calculated with the RC technique.

left figures represents the magnitude end phase of the calculated FRF $H^S_{x_iF_i}RC_{method}$. The result is compared to $H^S_{x_iF_i}$ of the total coupled system derived with Newton's second law. In the right figures the absolute errors of the magnitude and the phase are presented. The coupling result is clearly influenced by the measurement noise. At 0 Hz the rigid body modes of the free-free substructure A dominates the coupling result. Also at the natural frequency of substructure A at 5900 Hz, see Figure A.1, this resonance peak is visible in the coupling result. The resonance peaks and rigid body peak in the coupling result is very sensitive for errors due to measurement noise on the substructures. Therefore, coupling results at these frequencies must be handled carefully. We notice that the noise added to the individual FRFs is relative, meaning that at the resonance peaks and for small frequencies (due to the rigid body mode) the noise added to the FRF is larger than elsewhere. This test is therefore an extreme case on the noise added to the resonance peaks. Nevertheless, it clearly shows that the resonance peaks of the substructures can turn up as false resonance peaks in the coupling result. In the left figures, the average error is acceptable. Overall, the prediction of $H^S_{x_iF_i}$ is still quite good despite the undesired resonance frequencies on the natural frequencies of the substructures.

The IRC technique is also tested on the influence of measurement noise. Hereby, the FRF of the calculated joint system S, $H^S_{x_iF_i}$, and the remaining FRFs of substructure A are contained with noise. The IRC technique is used to calculate the FRF ($H^B_{x_cF_c}$) of substructure B according to (3.13). The result of the IRC calculation is displayed in Figure A.3. In the left figures, the magnitude end phase of the calculated FRF $H^B_{x_cF_c}IRC_{method}$ are presented.

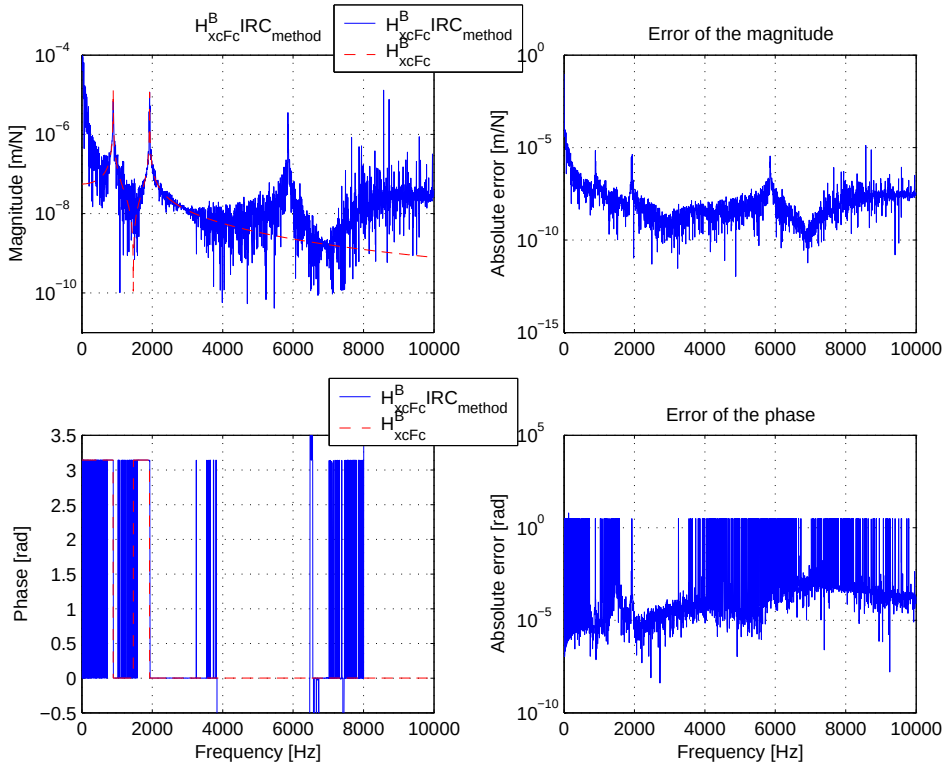

Figure A.3: $H^B_{x_cF_c}$ calculated with the IRC technique.

Two FRFs are presented, the first FRF shown is $H^B_{x_cF_c}$ derived with Newton's second law adopted on substructure B. The second FRF is calculated with the inverse coupling equation (3.13) of the IRC technique. In the right figures, the absolute errors of the magnitude and the phase are presented.

The influence of the measurement noise on the IRC technique can clearly be seen. Again the resonant peaks of the systems used in the IRC calculation appear in the IRC result. The rigid body mode at 0 Hz of substructure A is visible in the IRC result at 0 Hz. Also the mode at 5850 Hz is clearly visible. This is due to the large relative error on these resonance peaks of substructure A. This test is therefore comparable to the RC test which is an extreme case of the noise added to the resonant peaks on the used systems. Nevertheless, it clearly shows that the resonance peaks of the substructures can turn up as false resonance peaks in the decoupling result.

Appendix B

IRC calculation with biased measurements

The IRC technique is tested on the influence of biased measurements. It is assumed that substructure A is affected by the performance of biased measurements and the assembly S is measured accurately. The result of the IRC calculation is presented in Figure B.1. In the upper and lower left plots of Figure B.1 both $H^B_{x_cF_c}IRC_{technique}$ and $H^B_{x_cF_c}$ are plotted in magnitude and phase, respectively. $H^B_{x_cF_c}$ is derived with the use of Newton's second law and $H^B_{x_cF_c}IRC_{technique}$ is calculated with the IRC equation (3.13). In the right figures, the absolute errors of the magnitude and the phase are presented. There is a large error visible at the location of both resonance peaks of substructure B. The resonance peaks of substructure B are shifted. It can be concluded that the IRC technique handled the influenced substructure B as an other structure with other resonance frequencies. In practice, the detection of such an error is difficult, this states the importance of the accuracy of the response data of the substructures. The response data of the substructures must be as accurate as possible.

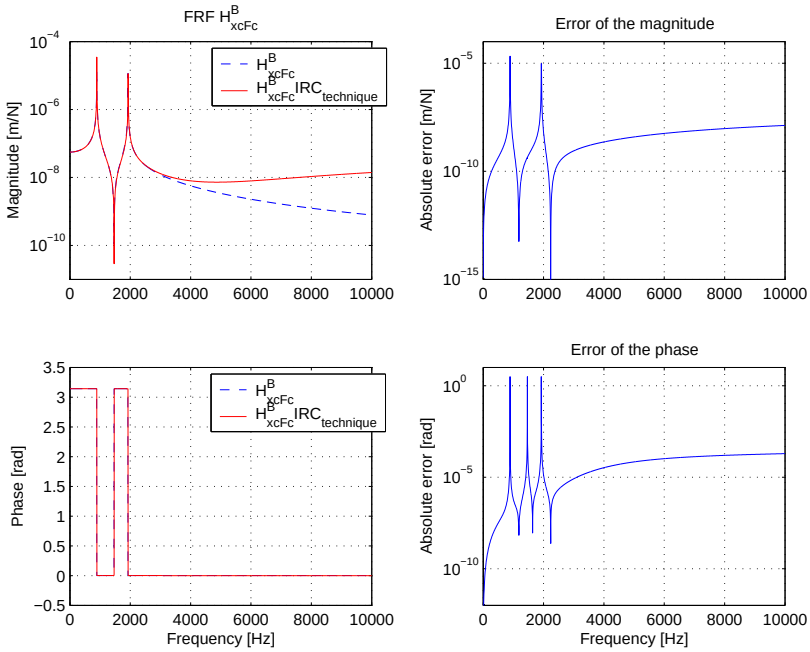

Figure B.1: $H^B_{x_cF_c}$ calculated with the IRC technique.

Appendix C

Model with rotational FRFs

The introduction of the rotational FRFs into the RC equation is tested on the mass-spring-damper model presented in Figure 3.2. The model is expanded with an extra translational DOF for each substructure. This extra translational DOF, which is called θ, represents the rotational DOF introduced in the RC equation (4.3). The replacement of the rotational DOF with the translational DOF is done to keep the testing of the RC equation with RDOFs and TDOFs as simple as possible. The expanded mass-spring-damper model is depicted in Figure C.1.

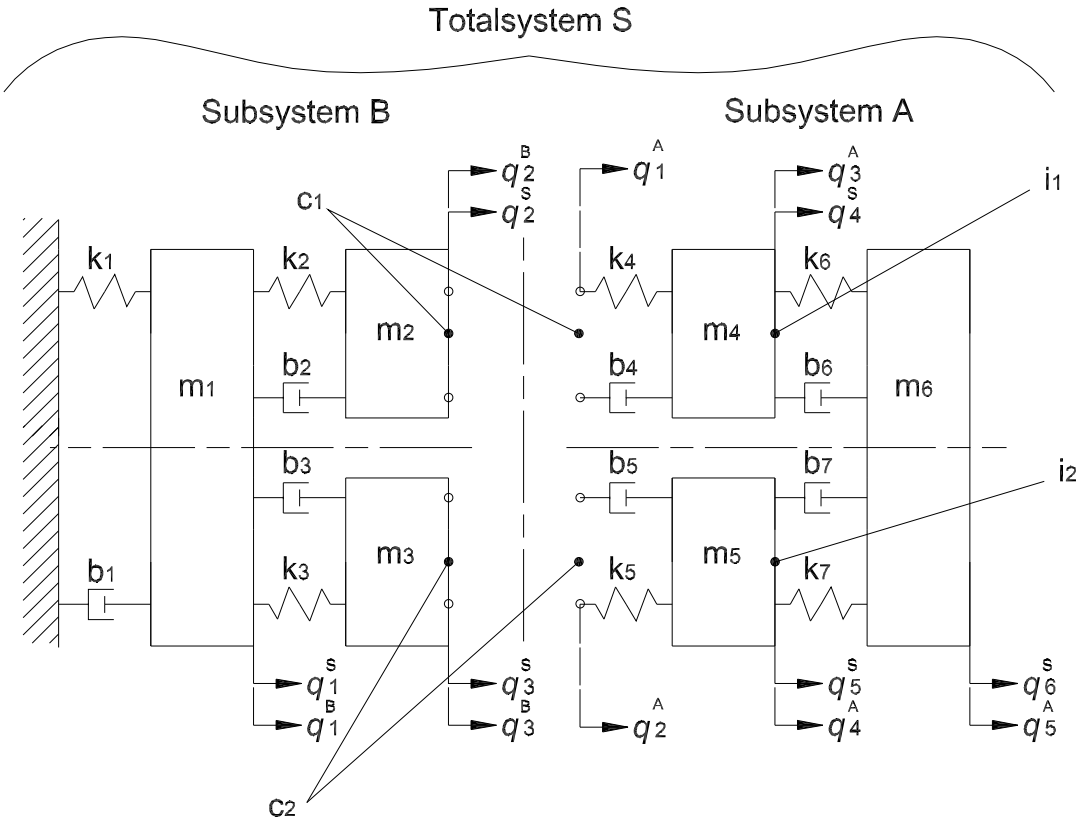

Figure C.1: Model of the 6DOF structure and its substructures.

Substructure A is a free-free system described by five generalized coordinates $q^A = [q_1^A\ q_2^A\ q_3^A\ q_4^A\ q_5^A]^T$. Substructure B is supported at one end and is characterized by three generalized coordinates $q^B = [q_1^B\ q_2^B\ q_3^B]^T$. The total system S is clamped at one end and is characterized by six generalized coordinates $q^S = [q_1^S\ q_2^S\ q_3^S\ q_4^S\ q_5^S\ q_6^S]^T$. The cross-section

consists of two coupling DOFs c_1 and c_2. The internal DOF i also consist of two DOFs i_1 and i_2. Both the DOFs c_1, c_2 and i_1, i_2 are dependent of each other with which we artificially model the influence of the RDOF of the HSM machine for the testing of the RC equation. The parameters used for the masses, spring constants and damping ratios are collected from a parameter-fit performed in [26] and summarized in Table C.1. The six most important modes of the spindle and tool of a HSM machine are used in this model.

	i=1	i=2	i=3	i=4	i=5	i=6
$m_i[kg]$	0.8705	0.3301	0.3228	0.03364	0.04124	0.01724
$k_i[N/m]$	$4.271 \cdot 10^7$	$3.075 \cdot 10^7$	$4.481 \cdot 10^7$	$2.229 \cdot 10^7$	$2.456 \cdot 10^7$	$3.010 \cdot 10^7$, $1.947 \cdot 10^7$
$b_i[-]$	0.04348	0.03551	0.04754	0.03364	0.03284	0.02754, 0.04924

Table C.1: Parameters used in the 6DOF mass-spring-damper model.

The three mass-spring-damper systems (A, B and S) are each described by a mass matrix ($\mathbf{M}$), stiffness matrix ($\mathbf{K}$) and damping matrix ($\mathbf{D}$). For substructure A,

$$\mathbf{M}^A = \begin{bmatrix} 0 & 0 & 0 & 0 & 0 \\ 0 & 0 & 0 & 0 & 0 \\ 0 & 0 & m_4 & 0 & 0 \\ 0 & 0 & 0 & m_5 & 0 \\ 0 & 0 & 0 & 0 & m_6 \end{bmatrix} \mathbf{K}^A = \begin{bmatrix} k_4 & 0 & -k_4 & 0 & 0 \\ 0 & k_5 & 0 & -k_5 & 0 \\ -k_4 & 0 & k_4+k_6 & 0 & -k_6 \\ 0 & -k_5 & 0 & k_5+k_7 & -k_7 \\ 0 & 0 & -k_6 & -k_7 & k_6+k_7 \end{bmatrix}$$

$$\mathbf{D}^A = \begin{bmatrix} b_4 & 0 & -b_4 & 0 & 0 \\ 0 & b_5 & 0 & -b_5 & 0 \\ -b_4 & 0 & b_4+b_6 & 0 & -b_6 \\ 0 & -b_5 & 0 & b_5+b_7 & -b_7 \\ 0 & 0 & -b_6 & -b_7 & b_6+b_7 \end{bmatrix},$$

for substructure B

$$\mathbf{M}^B = \begin{bmatrix} m_1 & 0 & 0 \\ 0 & m_2 & 0 \\ 0 & 0 & m_3 \end{bmatrix} \mathbf{K}^B = \begin{bmatrix} k_1+k_2+k_3 & -k_2 & -k_3 \\ -k_2 & k_2 & 0 \\ -k_3 & 0 & k_3 \end{bmatrix} \mathbf{D}^B = \begin{bmatrix} b_1+b_2+b_3 & -b_2 & -b_3 \\ -b_2 & b_2 & 0 \\ -b_3 & 0 & b_3 \end{bmatrix},$$

and for the total system S

$$\mathbf{M}^S = \begin{bmatrix} m_1 & 0 & 0 & 0 & 0 & 0 \\ 0 & m_2 & 0 & 0 & 0 & 0 \\ 0 & 0 & m_3 & 0 & 0 & 0 \\ 0 & 0 & 0 & m_4 & 0 & 0 \\ 0 & 0 & 0 & 0 & m_5 & 0 \\ 0 & 0 & 0 & 0 & 0 & m_6 \end{bmatrix}$$

$$\mathbf{K}^S = \begin{bmatrix} k_1+k_2+k_3 & -k_2 & -k_3 & 0 & 0 & 0 \\ -k_2 & k_2+k_4 & 0 & -k_4 & 0 & 0 \\ -k_3 & 0 & k_3+k_5 & 0 & -k_5 & 0 \\ 0 & -k_4 & 0 & k_4+k_6 & 0 & -k_6 \\ 0 & 0 & -k_5 & 0 & k_5+k_7 & -k_7 \\ 0 & 0 & 0 & -k_6 & -k_7 & k_6+k_7 \end{bmatrix}$$

$$\mathbf{D}^S = \begin{bmatrix} b_1+b_2+b_3 & -b_2 & -b_3 & 0 & 0 & 0 \\ -b_2 & b_2+b_4 & 0 & -b_4 & 0 & 0 \\ -b_3 & 0 & b_3+b_5 & 0 & -b_5 & 0 \\ 0 & -b_4 & 0 & b_4+b_6 & 0 & -b_6 \\ 0 & 0 & -b_5 & 0 & b_5+b_7 & -b_7 \\ 0 & 0 & 0 & -b_6 & -b_7 & b_6+b_7 \end{bmatrix}.$$

The FRFs of the individual systems are calculated from the **M**, **K** and **D** matrices with a damped MIMO frequency response function for linear systems given by

$$H_{xF}(j\omega) = \frac{1}{-\omega^2\mathbf{M} + j\omega\mathbf{D} + \mathbf{K}}, \tag{C.1}$$

in which $H_{xF}(j\omega)$ represents the transfer function matrix, ω represents the angular frequency range of interest and $j = \sqrt{-1}$. The derived FRFs of substructure A are written in a partitioned form with both translational and (fictionally) rotational coordinates. Also substructure B is presented in the translational and (fictionally) rotational DOFs. The subscripts i_1, i_2 and c_1, c_2 correspond with the location indicated with i_1, i_2 and c_1, c_2 in Figure C.1. The notation of x, F, θ and M corresponds with translational displacement response, input force, rotational displacement response and input momentum, respectively.

$$\begin{bmatrix} x^A_{i1} \\ \theta^A_{i2} \\ x^A_{c1} \\ \theta^A_{c2} \end{bmatrix} = \begin{bmatrix} H^A_{x_{i1}F_{i1}} & H^A_{x_{i1}M_{i2}} & H^A_{x_{i1}F_{c1}} & H^A_{x_{i1}M_{c2}} \\ H^A_{\theta_{i2}F_{i1}} & H^A_{\theta_{i2}M_{i2}} & H^A_{\theta_{i2}F_{c1}} & H^A_{\theta_{i2}M_{c2}} \\ H^A_{x_{c1}F_{i1}} & H^A_{x_{c1}M_{i2}} & H^A_{x_{c1}F_{c1}} & H^A_{x_{c1}M_{c2}} \\ H^A_{\theta_{c2}F_{i1}} & H^A_{\theta_{c2}M_{i2}} & H^A_{\theta_{c2}F_{c1}} & H^A_{\theta_{c2}M_{c2}} \end{bmatrix} \begin{bmatrix} F^A_{i1} \\ M^A_{i2} \\ F^A_{c1} \\ M^A_{c2} \end{bmatrix}, \begin{bmatrix} x^B_{c1} \\ \theta^B_{c2} \end{bmatrix} = \begin{bmatrix} H^B_{x_{c1}F_{c1}} & H^B_{x_{c1}M_{c2}} \\ H^B_{\theta_{c2}F_{c1}} & H^B_{\theta_{c2}M_{c2}} \end{bmatrix} \begin{bmatrix} F^B_{c1} \\ M^A_{c2} \end{bmatrix}. \tag{C.2}$$

Both the FRF matrices of substructure A and B are symmetrical matrices. This means that either the upper or lower half of the matrix does not have to be calculated. The result of the RC equation with two DOFs is displayed in Figure C.2

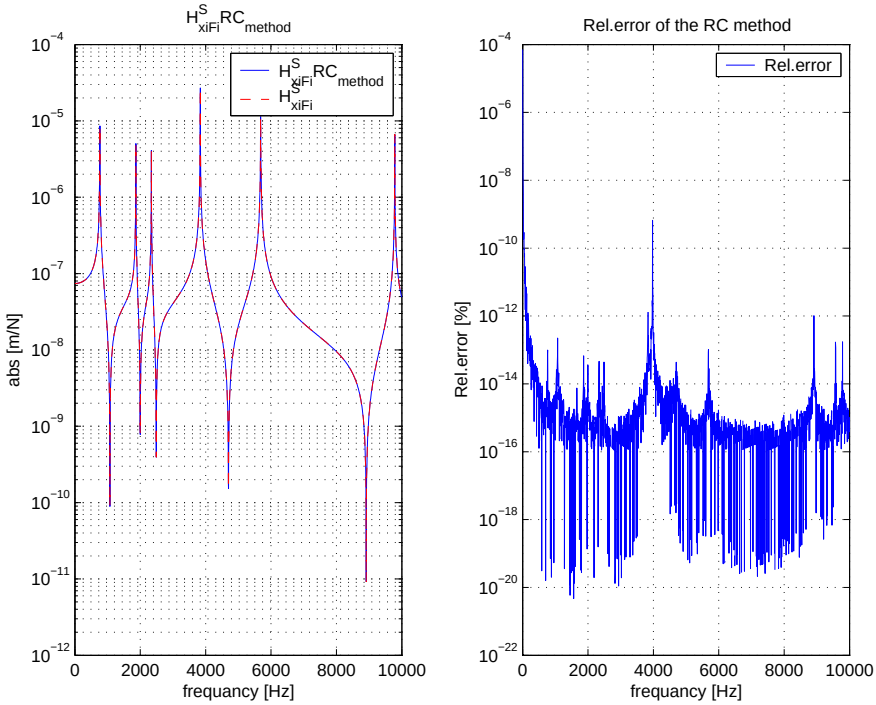

Figure C.2: RC calculation of $H^S_{x_iF_i}$.

In the left figure, two FRFs are presented; one of $H^S_{x_i F_i}$ derived from the $\mathbf{M}^S$, $\mathbf{K}^S$ and $\mathbf{D}^S$ matrices of the total system S and the second FRF is calculated with the coupling equation (3.10) of the RC technique. These two FRFs match perfectly. The right figure presents the relative error between these FRFs. The error is very small, from which we can conclude that the RC technique with TDOFs and RDOFs is exact and can be used to calculate the dynamics of the HSM machine.

Appendix D

Manual for implementation of the STEP format into UniGraphics

Jabro Tools uses Cybergrind software to design the end-mills. This program directly constructs a CNC program from the parameters of a specific milling process used by a customer. The geometrical end-mill design is converted into a STEP format [79]. STEP (STandard for the Exchange of Product model data) is an international standard for the computer-interpretable representation and exchange of product data, independent of any particular system.

The next steps must be performed to implement the STEP file into UniGraphics:

1. The STEP file is imported into UniGraphics with the import toolbox in UniGraphics. The settingsfile must be modified. The object types must be changed to solids. Now, a solid body is formed from the STEP file.

2. In UniGraphics the solid body is modified. The part above the cross-section of the end-mill is removed and the coordinate system is positioned.

3. Finally, the shortened and positioned free-free end-mill is converted to a PART file.

This PART file can be imported into Ansys through the Ansys connection for UniGraphics.

Appendix E

Dimensions of the used blanks and the end-mill replacement

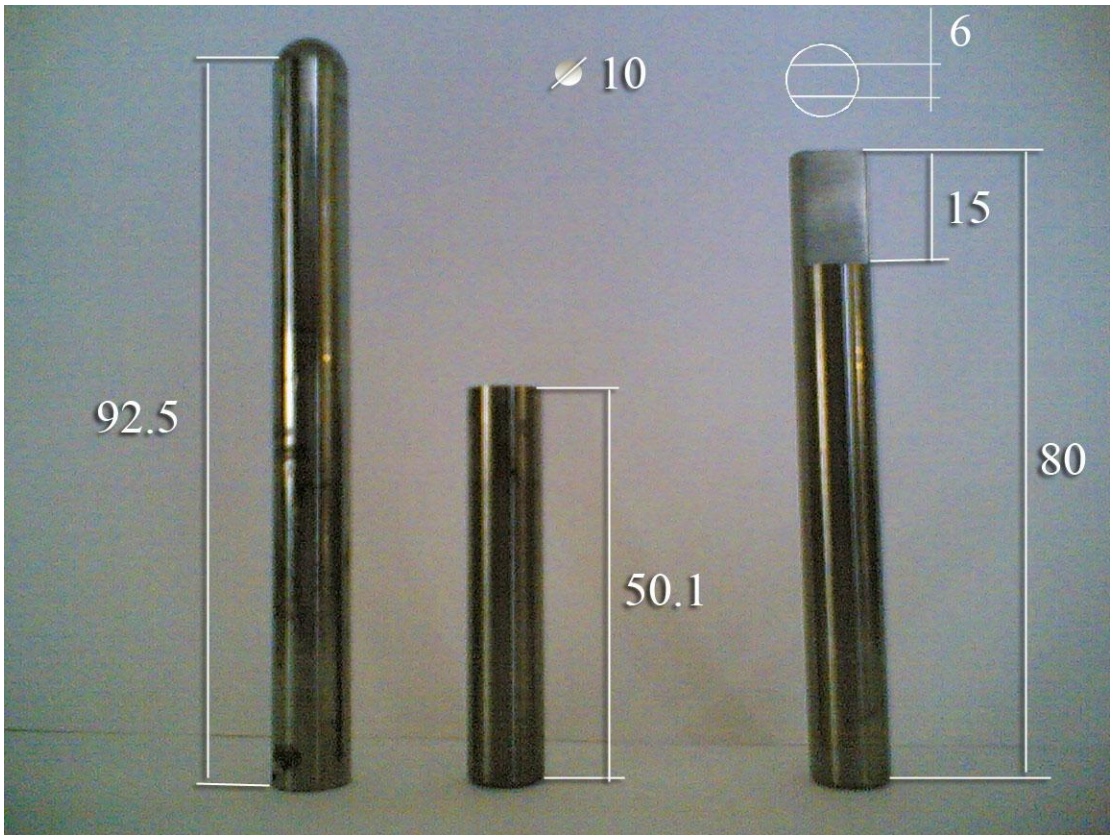

Figure E.1: Used blanks and end-mill replacement and dimentions in mm.

Appendix F

Calculation of the rotational FRFs in a model

The IRC theory with the methodology of two equations and two unknowns to construct the two FRFs $H^B_{\theta_c M_c}$ and $H^B_{x_c M_c} = H^B_{\theta_c F_c}$ is tested on the mass-spring-damper model presented in Figure C.1.

The FRFs $H^B_{x_c M_c} = H^B_{\theta_c F_c}$ and $H^B_{\theta_c M_c}$ are calculated with the inverse receptance coupling equations (4.18) and (4.19), respectively.

The results of this IRC calculation are displayed in Figures F.1 and F.2. The left two figures are from top to bottom: The magnitude and phase of $H^B_{\theta_c F_c}$ and $H^B_{\theta_c M_c}$, respectively. In these left figures, two FRFs are presented; the first FRF shown is derived from the equations of motion which is derived with Newton's second law by using the $\mathbf{M}^B$, $\mathbf{K}^B$ and $\mathbf{D}^B$ matrices of substructure B. The second FRF is calculated with the IRC technique. The right figures represent the absolute error between these FRFs in magnitude and phase, respectively.

It can be concluded that these two FRFs match perfectly. The error is very small, concluding that the IRC technique is exact.

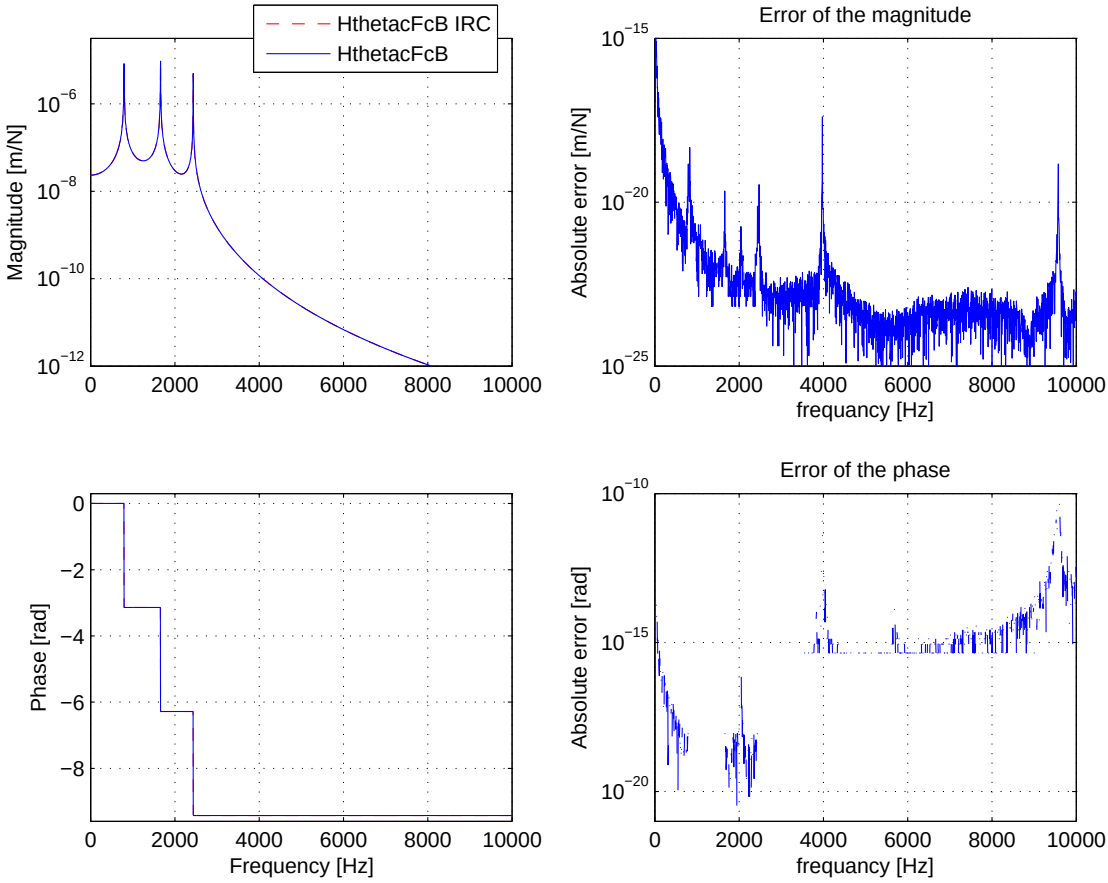

Figure F.1: IRC calculation of $H^B_{\theta_c F_c}$.

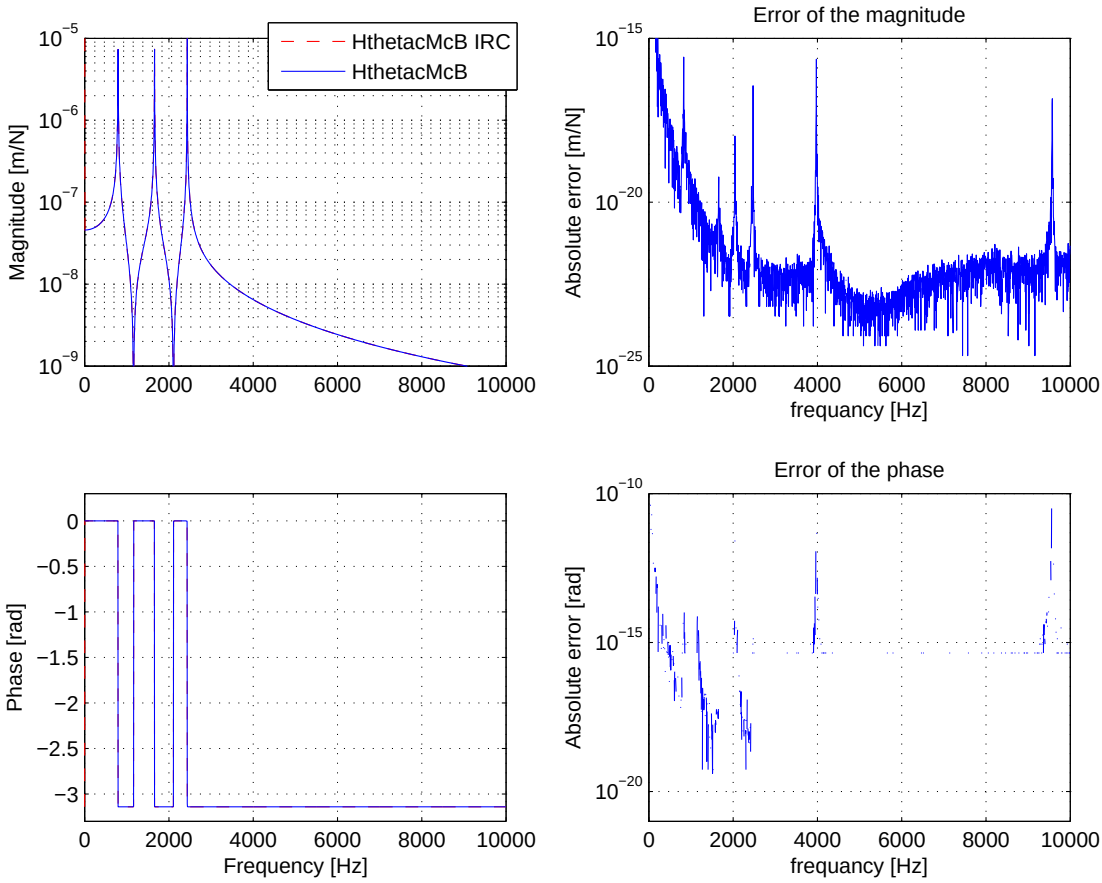

Figure F.2: IRC calculation of $H^B_{\theta_c M_c}$.